Characterization, Simulation, and Modeling of Waveguide-Type Ge Photodetectors on Si

Jeong-Min Lee

The Graduate School

Yonsei University

Department of Electrical and Electronic Engineering

Characterization, Simulation, and Modeling of Waveguide-Type Ge Photodetectors on Si

by

Jeong-Min Lee

A Dissertation

Submitted to the Department of Electrical and Electronic Engineering

and the Graduate School of Yonsei University

in partial fulfillment of the requirements for the degree of

Doctor of Philosophy

February 2017

This certifies that the dissertation of Jeong-Min Lee is approved.

_____

Thesis Supervisor: Woo-Young Choi

_____

Sang-Kook Han

_____

Hyunyong Choi

_____

Lars Zimmermann

_____

Myung-Jae Lee

The Graduate School

Yonsei University

February 2017

Table of Contents

List of Tables

List of Figures

Abstract

Characterization, Simulation and Modeling of Waveguide-Type Ge Photodetectors on Si

Jeong-Min Lee

Dept. of Electrical and Electronic Engineering

The Graduate School

Yonsei University

Si photonics is attracting a great amount of research interests as it can realize highly integrated photonic circuits based on mature silicon processing technology and provide solutions for the interconnect bottleneck of high-performance electronic systems. The photodetector (PD) is one of the key devices for realizing photonic integrated circuits, and high-performance germanium photodetectors (Ge-PDs) that can detect 1.5-μm wavelength light can be realized with silicon processing

technology. High-speed waveguide-type Ge-PDs on Si as well as high-performance integrated optical receivers containing these PDs has been reported.

This dissertation focuses on characterization, simulation and modeling of waveguide-type Ge PDs on a Si-on-Insulator substrate. Ge-PDs investigated having two different vertical and lateral p-i-n junction types are realized using IME's and IHP's Si photonics technology, respectively. The series resistance effect to Ge-VPDs, Si waveguide width effect, and n- and p-doped region areas effect to Ge-LPDs are investigated and they are characterized from DC, AC, and noise measurements. Furthermore, to better understand their characteristics in detail, new technique for co-simulation with TCAD (Technology Computer Aided Design) Sentaurus and Lumerical FDTD (Finite-Difference Time-Domain) simulation tools is established. By using this, transportation of photogenerated carriers in absorption regions for various waveguide-type Ge-PDs can be investigated. An modified equivalent circuit model 1.5-μm Ge-PDs is also developed for accurate analysis in this dissertation. This model consists of *RC* passive circuit components for representing p-i-n junction and parasitic components, two current sources for diffused and drifted photogenerated carrier transports, and one noise current source. Model

parameters are extracted from electrical *S*-parameter measurements, TCAD simulations of photodetection frequency responses, and noise measurements. The resulting equivalent circuit model accurately provides photodetection frequency responses at different bias voltages and can be applied to other types of PDs. This should be of great use for analyzing PD performance and optimal integrated with electronic circuits for Si-based applications.

Keywords: co-simulation, equivalent circuit model, Ge photodetector, optical interconnect, photodetector noise, photodetection frequency response, Si photonics, TCAD

1. Introduction

1.1. Optical Interconnect

Interconnect is a connection for the purpose of communication. Fig. 1-1 shows interconnect as different distance between thousands of kilometers to less than a millimeter. The long distance interconnection corresponds to cross-continent or trans-ocean telecommunication and short distance corresponds to board-to-board, inter-chip, and intra-chip interconnects [1]. Optical interconnect based on optical fibers has dominated long distance interconnections due to its broad bandwidth, immunity to electro-magnetic interferences, and low attenuation over long distance [2] and electrical interconnect based on copper wires has dominated short distance interconnections.

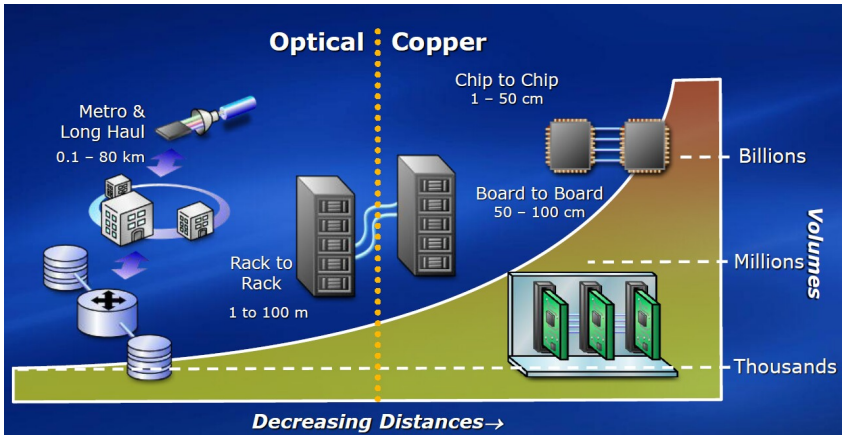

Fig. 1-1. Interconnect in different distances [1].

Nowadays, since explosive growth of data is held in variety of fields and usage of smartphones and cloud services are increasing as can be seen in Fig. 1-2, large data transmission and processing are required. As a result, the capacity of data center is getting more important. One of the consequences is that the data center traffic is estimated as doubling every 12 months [3]. Therefore, not only many distributed hardware has faster multi-core CPUs for more efficient computation, but also more connectivity to cover increasing link speeds and lengths is required in data centers.

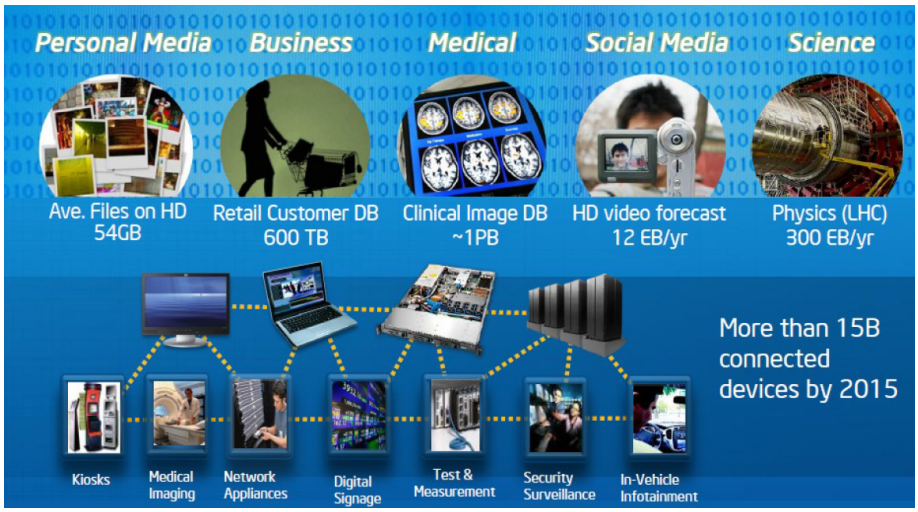

Fig. 1-2. The explosive growth of data [4].

However, electrical interconnect based on copper wires has some difficulties in being capable of increasing the data capacity, power, and volume. Optical interconnect can be an attractive candidate to fulfill the requirements due to the reason that fiber-optics provide broad bandwidth, low loss and power consumption, small volume. This can be achieved by using several transmission methods as shown in Fig. 1-3 such as WDM (wavelength division multiplexing) which multiplexes a number of optical carrier signals onto a single optical fiber by using different wavelengths [5], and PSM (parallel single mode) which uses a parallel optical interface where data is simultaneously transmitted and received.

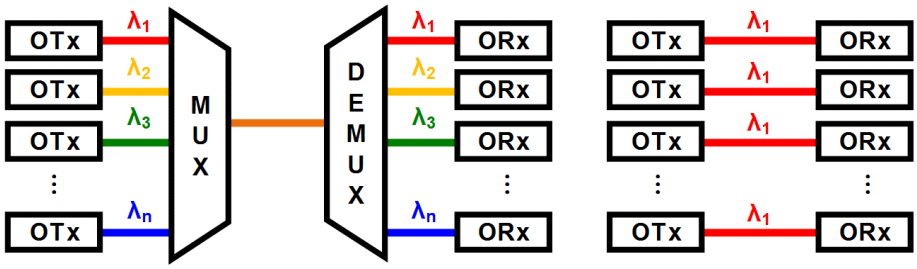

Fig. 1-3. Fiber-optic transmission types: (a) WDM and (b) PSM.

Optical interconnect used in data center connectivity is shown in Fig. 1-4. In here, electrically modulated signals are converted to optical signals by lasers and external optical modulators. Transmitted optical signals through optical fiber are detected and converted to electrical signals by photodetectors and corresponding electrical signals are treated by various functions of electronic circuits. Additionally, WDM or PSM technology can be used for transmitting large data through optical fibers.

The mature Si IC technology can realize high-performance and low-cost electrical circuits. However, optical devices based on III-V materials used in long-distance communications are not compatible with Si IC technology because it costs a lot to fabricate and integrate with electrical circuits on different platform. Therefore, Si-based optical devices receive a lot of attention for realizing low-cost optical interconnect.

Nowadays, Intel announces noteworthy optical transceiver products which are composed of Si-based optical devices by using Si photonics technology and Si CMOS circuits on single Si chip [3]. They also adopt various transmission methods such as PSM4 and coarse WDM technology to support 100-Gb/s data transmission for interconnection between row to row. This provides small form factor, high speed, and

low power consumptions. This implies infinite possibilities and a lot of potentials of optical interconnect, which can be a great solution for the interconnect bottleneck of high-performance electronic systems.

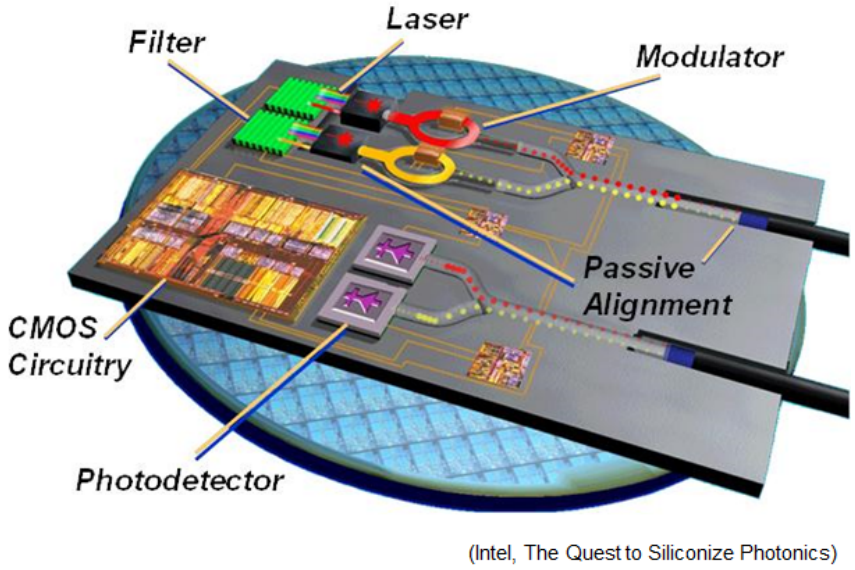

Fig. 1-4. The composition of optical transceiver on Si [1].

1.2. Si Photonics Technology and its Application

Si material is transparent at the wavelengths of 1300 and 1550 nm which are widely used in fiber-optic communication. Si waveguide can be realized with high refractive index contrast by using Si and its own oxide (SiO_2). The dimension of waveguide can be determined by Si semiconductor fabrication process and various kinds of waveguide-based optical devices can be realized by fabrication technology.

Many foundries such as IHP, IME, IMEC, and CEA-LETI support this optical device fabrication on SOI (Si-on-Insulator) substrate as MPW (Multi-Project Wafer) services. MPW service represents dividing the wafer space to different users and hence fabless companies and users can realize optical devices and electronic circuits at relatively low cost. Using this, cost-effective photonic integrated circuits can be realized as shown in Fig. 1-5 including waveguide-based passive and active optical devices such as grating and directional coupler, Ge-on-Si photodetector (Ge-PD), and Si Mach-Zehnder (MZM) or micro-ring modulators (MRM). Unfortunately, since Si laser is not available for commercialization now, additional fabrication and packaging cost for integration with the other are required yet.

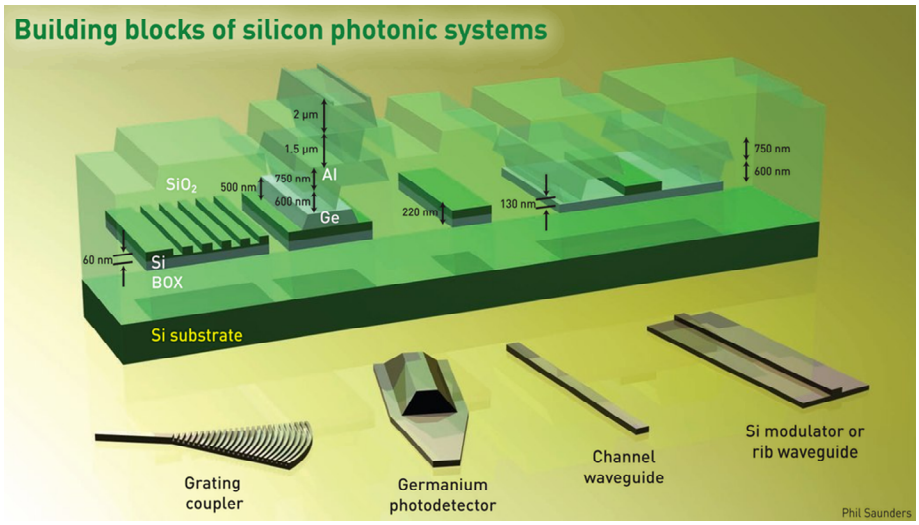

(Matthew Streshinky *et al*., The Road to Affordable, Large-Scale Silicon Photonics)

Fig. 1-5. Building blocks of silicon photonic systems [6].

These Si-based waveguide-type optical devices with various functions can be applied to various applications such as optical transceiver [7], bio-sensor [8], and radio-over-fiber system [9].

Fig. 1-4 shows the composition of optical transceiver used in data center connection. In here, electro-optical (E/O) and opto-electronic (O/E) conversion and blocks for multiplexing and demultiplexing optical signals, and interconnection between optical devices are needed. By using Si photonics technology, various optical couplers, filters, modulators, and detectors can be fabricated on Si platform to realize cost-effective as well as high-performance optical transceivers.

Si photonics technology can be also applied to bio-sensor chip [8]

and fiber-wireless system [9]. Fig 1-6 shows MZI based bio-sensor chip [8] and this uses refractive index difference between standard and sensing arm interacting with sample. The recombined optical signal is converted to electrical signals for signal processing by low-noise photodetector and electronic circuits. Optical devices and electronic circuits used in bio-sensor can be fabricated on Si substrate by Si photonics technology which provides cost-effective bio sensor application. Fig. 1-7 shows schematic diagram of fiber-wireless systems (uplink part) for being capable of data capacity increasing and a decrease of wireless coverage [9]. For this application, optically modulated signals are transmitted between central office and RAU (remote antenna unit) through optical fiber and for downlink and uplink, O/E and E/O devices as well as electronic circuits for signal processing are required in RAU. This can be also realized on Si by using Si photonics technology at low cost and a good example of applying to optical interconnect.

Although there exist technological constraints and challenges to optical interconnect by Si photonics technology, it has many potentials and possibilities for providing high-performance and cost-effective optical devices as well as compatibility with Si IC technology.

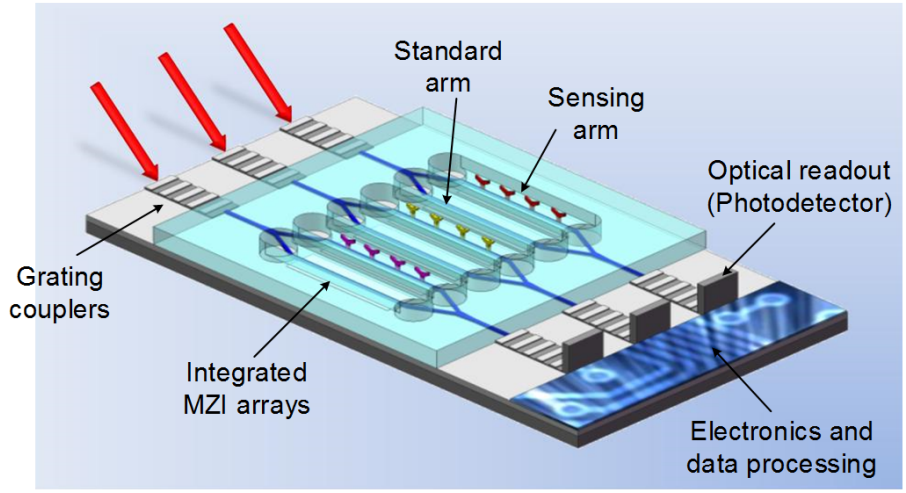

Fig. 1-6. MZI-based bio-sensor system [8].

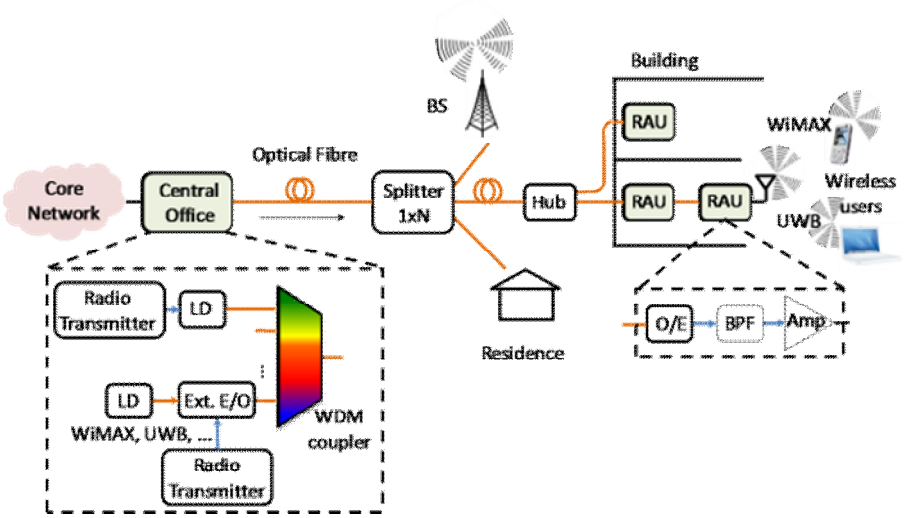

Fig. 1-7. Schematic diagram of fiber-wireless system [9].

1.3. Ge Photodetectors on Si

As introduced before, various optical devices on Si are required for cost-effective optical interconnect applications. For these applications, high-performance photodetector which can detect light is needed for converting optical to electrical signals. Light detection at around 1300 and 1550 nm which is used for optical communication is not available in Si which is transparent in 1300–1600 nm regions. To detect light in these ranges, materials that can absorb light are required such as Ge or Ge containing or III-V compound materials such as InGaAs and InP.

Many Si photonics foundry services select Ge material because it provides high-quality Ge on Si now despite of 4% lattice mismatch between Si and Ge which causes misfit and threading dislocations [10], high carrier mobility of Ge which is proper for high-speed photodetector, and low fabrication and packaging cost expended in heterogeneous integrated III-V photodetectors on Si.

To provide high-performance photodetector on Si platform, various types of Ge-on-Si photodetectors are currently researching and reporting [11]–[13]. Light coupling of photodetectors are categorized by two types as shown in Fig. 1-8: one is normal incidence which is the light coupling scheme with introducing light on the top or bottom

surface of photodetector [14] and the other is waveguide-type photodetectors which light is delivered to the photodetector by grating or edge coupler based on optical waveguide [15]. For high-responsivity photodetectors with normal light incidence, large thickness of Ge region is required for increasing absorption rates, however, this causes large junction capacitance resulting in large *RC* time constants and this limits the photodetection bandwidth. Since this is not proper for high-speed optical interconnect applications, waveguide-type photodetectors are preferred for high-speed operation.

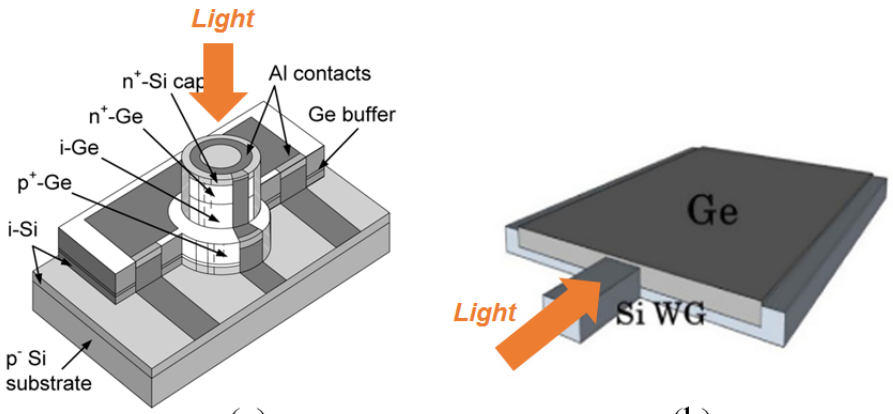

Fig. 1-8. Light coupling schemes: (a) normal incidence [14] and (b) waveguide coupling [15].

Waveguide-type Ge photodetectors on Si are realized by lateral p-i-n [11], vertical p-i-n [12], and Metal-Semiconductor-Metal [13] structures and avalanche photodetectors [16]. Table 1-1 shows summarized waveguide-type Ge-PDs on Si and they have shown high responsivities, low dark current densities, and large photodetection bandwidth with the same or better than photodetectors based on III-V materials on Si. Ge-PD on Si fabricated by using Si photonics technology can be applied to many various applications due to its outstanding performance as well as low-cost fabrication. Therefore, this dissertation is focused on the waveguide-type Ge-PDs and their characteristics are investigated intensively.

TABLE 1-1
PERFORMANCE COMPARISON OF WAVEGUIDE-TYPE GE AND III-V ON SI PHOTODETECTOR.

	IBM [17]	**IMEC [18]**	**IHP [19]**	**[20]**	**[21]**
Absorption Material	Ge			InP /InGaAs	InP
Fabrication	Growth			Bonded	Growth
Junction type	Metal-Semiconductor-Metal	Lateral P-I-N	Lateral P-I-N	Vertical P-I-N	Uni-travelling carrier
Responsivity	0.14 A/W (at –1 V)	0.74 A/W (at –1 V)	> 1 A/W (at –2 V)	0.45 A/W	0.85 A/W
Photodetection BW	40 GHz (at –2 V)	67 GHz (at –1 V)	> 70 GHz (at –1 V)	33 GHz	30 GHz (at –5 V)
Dark current	90 μA (at –1 V)	< 2.4 nA (at –1 V)	100 nA (at –1 V)	1.6 nA (at –4 V)	10 nA (at –5 V)
Absorption region thickness	100 nm	160 nm	500 nm	700 nm	300 nm

1.4. Equivalent Circuit Model of Photodetectors

For high-performance optical interconnect, high-performance Ge-PD on Si as well as integration with electrical circuits are important. Accordingly, interconnect between photodetector and corresponding electronic circuits should be considered for optimal performance. As a result, co-design with photodetector and electronic circuits are a great importance. For this, accurate equivalent circuit models of a variety of photodetectors are established containing various characteristics of bias dependency, optical-power dependency [22], and nonlinearity at large input optical power [23]. In addition, by virtue of this, a lot of approaches of integrating photodetectors and electronic circuits can be implemented by co-simulation and optimal design as well as performance analysis of low-power consumption and signal-to-noise ratio can be possible [24]. Therefore, accurate equivalent circuit models of photodetectors are required for improved integration without performance degradations and several approaches for establishing equivalent circuit model of photodetectors are researched [25]–[27].

Fig. 1-9 shows an equivalent circuit model of photodetector composed of circuit components used in several publications [25]–[27]. The model is consisted of two parts: First part is one frequency

dependent current source model for representing photogenerated carrier transports in absorption region and second is electrical components of photodetector which can be represented as passive *RC* circuit parameters. For reverse biased photodetector, most photogenerated carriers in absorption region are assumed that carriers experience sufficiently large electric field for carrier drift and one frequency-dependent current source model having single-pole frequency determined by carrier drift velocity is widely used [27]. In addition, reverse-biased photodetector can be considered as parallel connected junction resistance (R_j) and capacitance (C_j) for depletion region, series resistance (R_s) for charge neutral region, and parasitic impedance (Z_{para}) for interconnect line and pads.

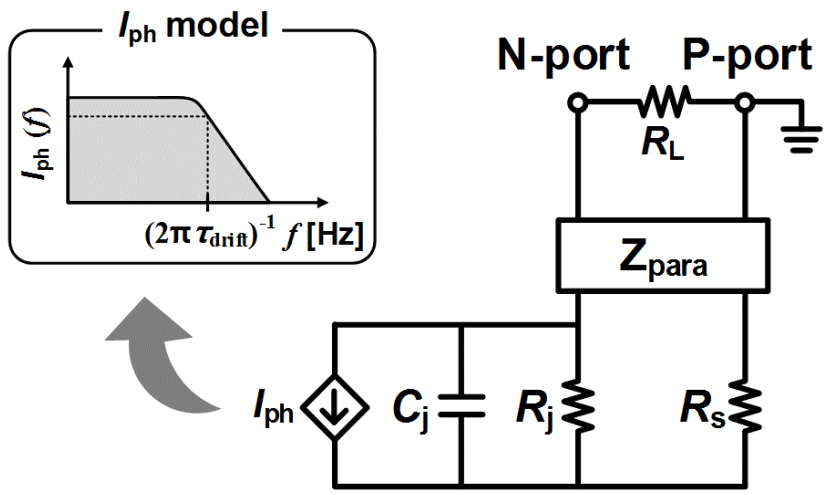

Fig. 1-9. Equivalent circuit model of photodetector with Z_{para}.

The model parameters used in equivalent circuit model in Fig. 1-9 are generally extracted and determined by process of fitting the simulated results based on model to measured electrical reflection coefficient and photodetection frequency response results [26].

However, as can be seen in Fig. 1-10, for several waveguide-type Ge-PD, this model cannot accurately model photodetection frequency responses [18], [28]–[29], especially at low-frequency range where the measured responses show a clear roll-off. This means that equivalent circuit model of waveguide-type photodetectors need to be modified according to the given device structures and configurations.

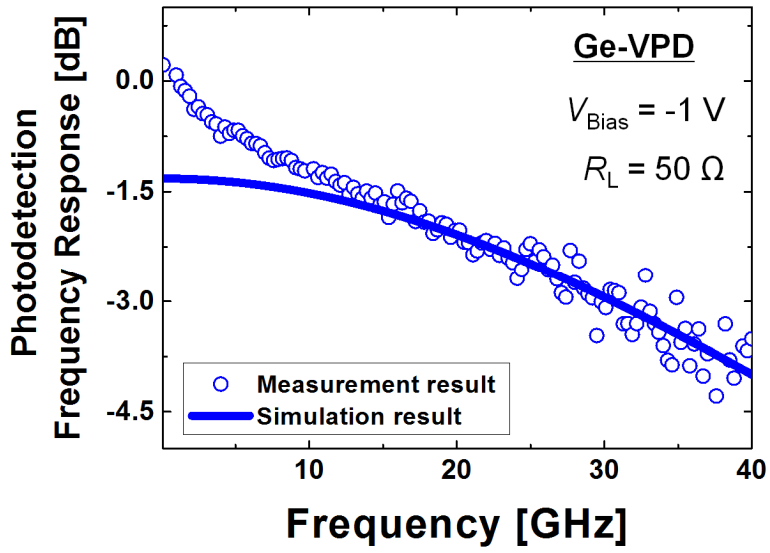

Fig. 1-10. Photodetection frequency response differential between measured and simulated results based on equivalent circuit model in Fig. 1-9 of Ge-VPD at –1 V.

This dissertation mainly focuses on waveguide-type Ge-PD on Si and how equivalent circuit model should be modified and how accurate model parameters can be determined. In chapter 5, the modified equivalent circuit model is introduced and the difference with model in Fig. 1-9 is also investigated. Furthermore, autonomously developed TCAD with FDTD simulation for extracting model parameters are introduced which provides enhanced accuracies than extraction by fitting the simulated results based on model to measured frequency response results.

By using this model and model parameter extraction, the characteristics of several waveguide-type Ge-PDs are investigated in chapter 6. These will be very useful for investigating photodetector performance analysis and co-designing the optimum integrated photodetector and electronic circuits on circuit simulator circumstance such as SPICE (Simulation Program with Integrated Circuit Emphasis), Cadence, ADS (Advanced Design System) and so on.

1.5. TCAD Simulation

For accurate equivalent circuit model of photodetector, accurate model parameters need to be provided and especially, the transportation of photogenerated carriers in absorption region should be interpreted for establishing current source model in Fig. 1-9. For simple structure of photodetector, this can be estimated by using simple physical equations or fitting the measured frequency response results to be simulated. However, this may not be easy for waveguide-type photodetector due to its complicated structures.

TCAD is the computer simulation tools that can investigate and develop semiconductor technology process and device characteristics. This can interpret the carrier transportation in semiconductor devices, numerically. This also provides graphical user interface (GUI) -based simulation environment for simulation and analyses for simulated results.

The TCAD process and device simulation tool supports a wide range of electrical and optoelectronic devices such as CMOS, BiCMOS, power, memory, and analog/RF devices and CMOS image sensor, solar cell, and photodetector, respectively. TCAD reduces technology development time and cost which is useful for development, and

optimization of semiconductor technologies with comprehensive physical based modeling where, in turn, TCAD simulation provides engineers with insights on the behavior of semiconductor devices. Synopsys TCAD Sentaurus, Taurus MEDICI, SILVACO and ATLAS provide this as commercial software.

In this dissertation, photogenerated carrier transports in waveguide which is complicated to estimate are interpreted by using TCAD Sentaurus simulation. This helps to provide model parameters of current sources in equivalent circuit model with improved accuracies.

Synopsys TCAD Sentaurus

TCAD Sentaurus supports various types of tools according to different objectives. Sentaurus Process and Sentaurus Topology is used for process simulation, Sentaurus Structure Editor for structure editing, Sentaurus Device, Raphael, Sentaurus Interconnect for device and interconnect simulation, Sentaurus Visual and Inspect for visualizing simulation results.

Sentaurus Structure Editor is a 2-D and 3-D device editor for editing device structures using geometric information. Doping profiles and meshing strategies can be defined in Structure Editor. Sentaurus Device simulates the electrical, thermal, and optical characteristics of

silicon-based or compound semiconductor devices in 2-D and 3-D.

Sentaurus Device has an extensive set of physical models and parameters of materials, and can simulate DC, AC, and transient and harmonic balance analysis. Small-signal scattering parameters (*S*-parameters) also can be simulated as different frequencies.

Sentaurus Visual and Inspect provides 1-D, 2-D, and 3-D and 1-D visualization, respectively and data exploration environment. These supports enabling post processing of output data to generate new curves and extracted parameters.

1.6. Outline of dissertation

This dissertation focuses on characterization, simulation, and modeling of waveguide-type Ge-PDs on Si. The main contribution of this work is establishing an accurate equivalent circuit model of waveguide-type Ge-PD on Si and providing the way of model parameter extraction using TCAD Sentaurus simulation with improved accuracies. With this model, quantitative investigations and characterizations of several different types of waveguide-type Ge-PDs are performed in this dissertation.

Chapter 2 shows device descriptions of waveguide-type Ge-PD

investigated in this dissertation. Two different photodetectors having vertical and lateral p-i-n junctions (Ge-VPD and Ge-LPD) are realized by using IME and IHP Si photonics fabrication process, respectively. The detailed device structures and configurations are explained in this chapter.

In chapter 3, the waveguide-type Ge-PDs are characterized by DC, AC, and noise measurements and their setups and sampled data are shown. For DC characterizing, measurement setup for current-voltage and photocurrent linearity are introduced and they are characterized according to a variety of conditions such as bias voltages and input optical power with measurement results. For AC characterization, electrical *S*-parameter and photodetection frequency response measurements and their setups are introduced in this chapter. Furthermore, PD noises are measured by using noise measurement setup and the derivation for accurate emitted PD noise is also shown in this chapter.

Chapter 4 introduces developed waveguide-type Ge-PD simulation using TCAD Sentaurus and Lumerical FDTD tools. The light guiding and absorption in waveguide are simulated using FDTD tool and the transportation of absorbed photogenerated carriers are interpreted in TCAD. For this, the information of photogenerated carriers calculated

by FDTD is imported to TCAD and the procedure for that is mainly introduced in this chapter. By using simulation technique, the several important model parameters are extracted and identified.

Chapter 5 shows modified equivalent circuit model of waveguide-type Ge-PD. For waveguide-type PD, typically used equivalent circuit model needed to be modified. In this chapter, why the model should be modified and how to model that in the model are intensively investigated. The model parameters are extracted by using previously introduced AC measurements in chapter 3 and developed TCAD simulation in chapter 4, respectively.

In chapter 6, the characteristics of several types of Ge-VPDs and Ge-LPDs fabricated by IME and IHP fabrication process are investigated, respectively. Two types of Ge-VPDs having different series resistance, four types of Ge-LPDs having different Si waveguide width, and four types having different n- and p-doped region areas are realized and their influence on PD performance are discussed with a variety of measurements and investigated based on their equivalent circuit models.

2. Device Description of Waveguide-Type Ge PDs

2.1. Vertical P-I-N Junction Photodetector (Ge-VPD)

Fig. 2-1(a) and (b) show the top-view and cross-section of the Ge-PD having vertical p-i-n junction type (Ge-VPD). In this dissertation, as can be seen in Fig. 2-1(b), it was fabricated on 220-nm thick Si-on-Insulator (SOI) layer having 2-μm thick buried-oxide layer (BOX) through the IME Si photonics MPW service as shown in Fig. 2-1(c) [30]. The Ge-VPDs are composed of highly n-doped Ge (N^{++}-Ge) layer, 0.5-μm thick intrinsic Ge (i-Ge) layer, and 0.22-μm thick p-doped Si (P^{+}-Si and P^{++}-Si) layer, vertically. The devices are nominally 7-μm wide on the top, 8-μm wide at the bottom, and 11-μm long. The peak doping concentrations are 1.27×10^{21} cm^{-3} for N^{++}-Ge, 3.5×10^{19} cm^{-3} for P^{+}-Si, and 5×10^{20} cm^{-3} for P^{++}-Si which are provided from IME foundry. Series resistance of PD is mainly determined by n- and p-doped charge neutral regions. In this dissertation, the influence of bias voltage dependency and series resistance on Ge-VPD performances as current-voltage and linearity characteristics are investigated and their equivalent circuits are also established.

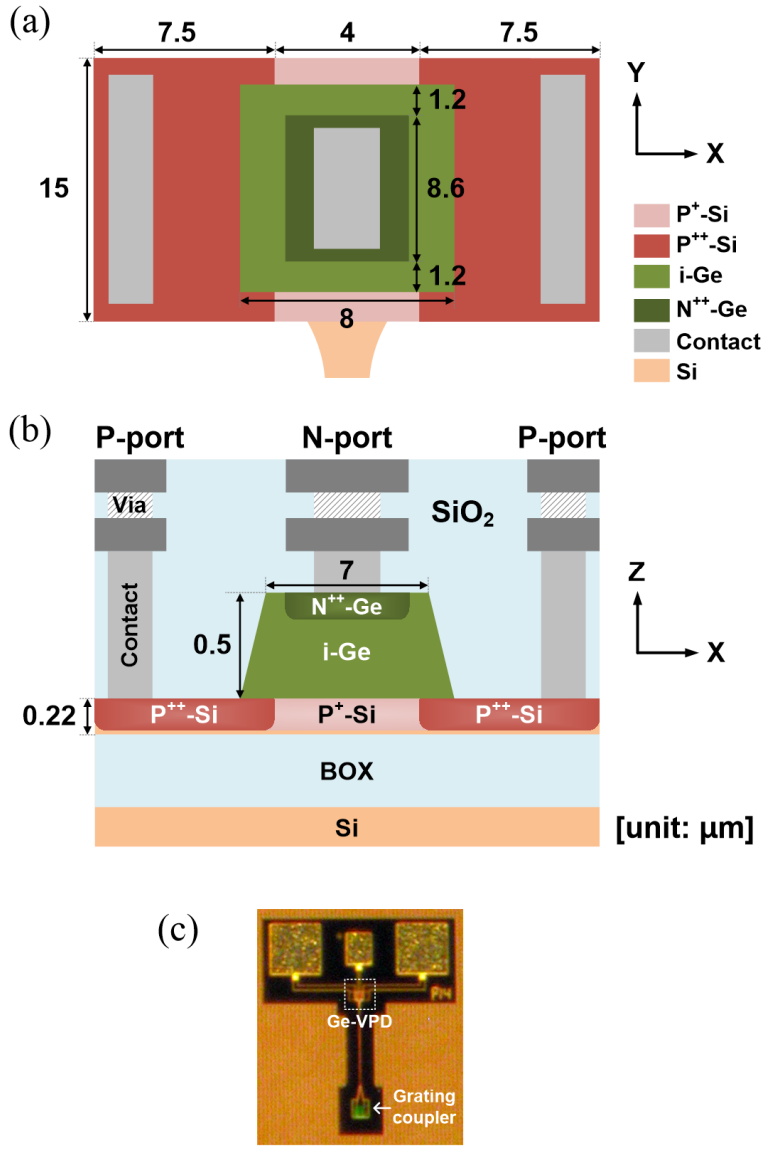

Fig. 2-1. (a) Top-view, (b) cross-sectional view, and (c) fabricated chip photo of Ge-VPD.

2.2. Lateral P-I-N Junction Photodetector (Ge-LPD)

Fig. 2-2(a) and (b) show top–view and cross-section of the Ge-PD having lateral p-i-n junction type (Ge-LPD). In this dissertation, Ge-LPDs having lateral p-i-n junction are fabricated by using IHP photonic BiCMOS process as shown in Fig. 2-2(c) which technology can fabricate integrated photonic devices and electronic circuits on single chip [19]. However, at this time, most BiCMOS frontend-of-line fabrication process are excluded for focusing on photodetector module only, except the $CoSi_2$ module for silicide process. Epitaxial grown Ge layer is on SOI substrate having 220-nm thick, 750-nm wide Si waveguide, and 2-μm thick BOX as shown in Fig. 2-2(b). Si cap is deposited on Ge region for silicidation process used in BiCMOS process which provides small contact resistance. 600-nm wide SiN pedestal is followed by self-aligned ion implantation for B and P. The average doping concentrations of p- and n-doped regions are about 1×10^{18} cm^{-3} and the length of Ge-LPDs are 20 μm. Details of fabrication process can be found in [19]. In this dissertation, the effects of underlying Si waveguide width and n- and p-doped region areas to Ge-LPDs are investigated and their characteristics are analyzed and explained by using their equivalent circuit model.

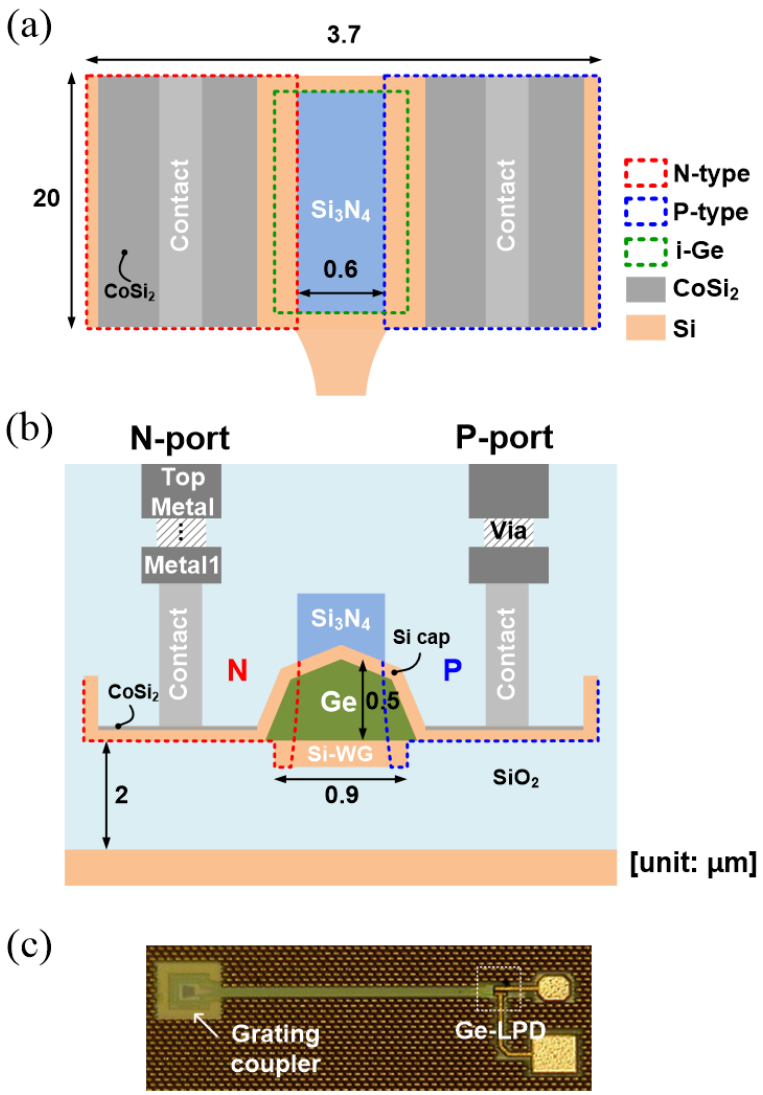

Fig. 2-2. (a) Top-view, (b) cross-sectional view, and (c) fabricated chip photo of Ge-LPD.

3. Measurements for Waveguide-Type Ge-PD

To characterize waveguide-type Ge-VPDs and Ge-LPDs, several measurements are performed in this chapter and their DC, AC, and noise measurement setups and sampled measurement results for one type of Ge-VPD are given for example.

In chapter 3.1, the measurement setup for current-voltage characteristics and linear photocurrent characteristics are shown. By measuring dark current and photocurrent as different bias voltages, responsivity, and series resistance can be extracted and by varying input optical power which introduces to waveguide-type Ge-PDs, the linearity of photocurrent can be investigated. These investigations are useful to analog communication systems for antenna remoting, phased array antennas, and photonic analog-to-digital converter and digital communication systems [31]. To build optical links for these systems and directly drive digital logic circuits, photodetector need to be able to operate at large linear photocurrents for satisfying required dynamic range.

For AC characterization, electrical *S*-parameter and photodetection frequency response are measured. From measured electrical S-parameter results, impedances characteristics of waveguide-type Ge-PD

can be investigated. From measured photodetection frequency responses, how the frequency-dependent characteristics of waveguide-type Ge-PD are varied according to different frequencies and these are essential elements for establishing equivalent circuit model which will be discussed in chapter 5. All measurement setups and sampled measurement results for Ge-VPD are described in chapter 3.2.

Ge-PD noise measurement is investigated for noise characterization in this chapter 3.3. In bio-sensor applications, since very low-level optical signals like noise are dealt with, low-noise photodetectors are needed. For that, noise contribution to Ge-PD should be clarified. From noise measurement, noise characteristics of Ge-PD and which elements affect Ge-PD noise can be investigated. In addition, noise deembedding procedure is introduced and derived to extract accurate noise current density of Ge-PD only. In chapter 5, Ge-PD noise model is provided based on noise measurement which helps to design integrated photodetector and electronic circuits in bio-sensor chip.

3.1. DC Measurements

3.1.1. Current-Voltage Characteristic

Fig. 3-1 shows measurement setup for device current-voltage characterization. 1.55-μm light through lensed fiber or fiber array is injected into the device through an on-chip grating coupler having about 5-dB insertion loss connected to Ge-VPD. A polarization controller is used so that only TE-polarized light is coupled into grating coupler. Positive bias voltages are applied to N-port of Ge-VPD with P-port grounded for bias using semiconductor parameter analyzer (Agilent 4156A). Output electrical signals are measured through RF probes and all measurements are done on-wafer. Fig. 3-2 and Fig. 3-3 show measured current-voltage and wavelength-responsivity characteristics at –1 and –4 V for incident optical power of –5 dBm coupled into the Ge-VPD, respectively. As can be seen in Fig. 3-3, this Ge-VPD has about 0.45-A/W responsivity at 1.55-μm wavelength as different reverse bias voltages.

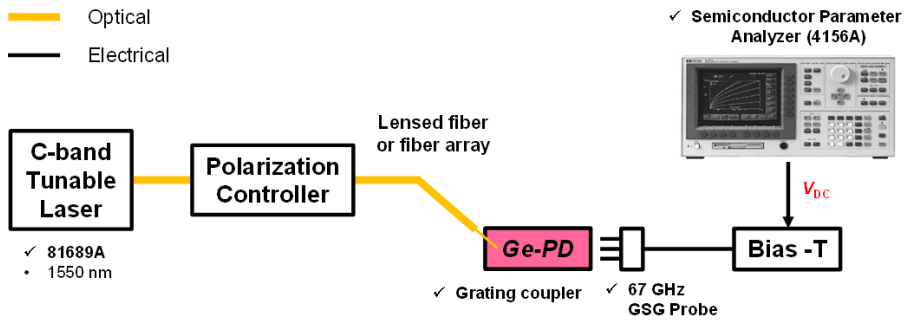

Fig. 3-1. Current-voltage measurement setup for waveguide-type Ge-PD.

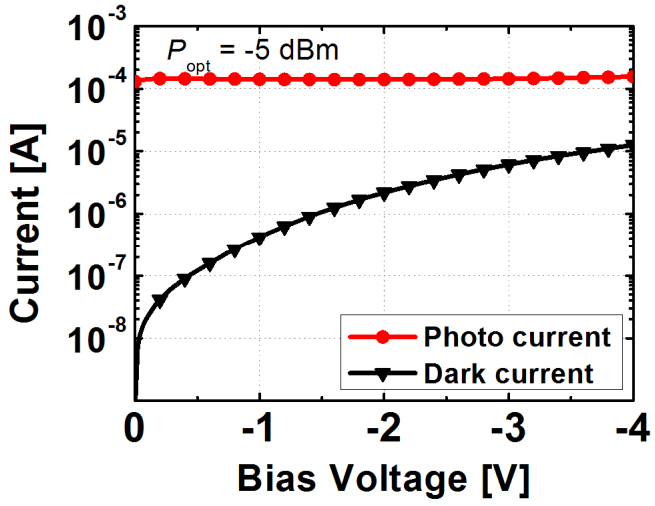

Fig. 3-2. Dark and photo current-voltage characteristics of Ge-VPD.

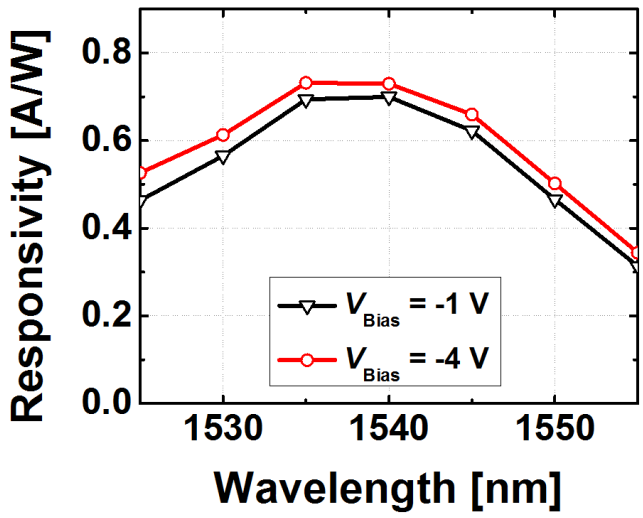

Fig. 3-3. Responsivity-wavelength characteristics of Ge-VPD at –1 and –4 V.

3.1.2. Nonlinear Photocurrent Characteristic

Fig. 3-4 shows measurement setup for linearity characterization. For varying input optical power, input light is amplified by an Erbium-doped fiber amplifier (Keopsys KPS-BT2-C) and then controlled to desired power level with a variable optical attenuator. At high input optical power to Ge-PD, since large photocurrent is flowed through PD, the PD often encounters device fail. Therefore, careful optical power level controls are needed during measurement.

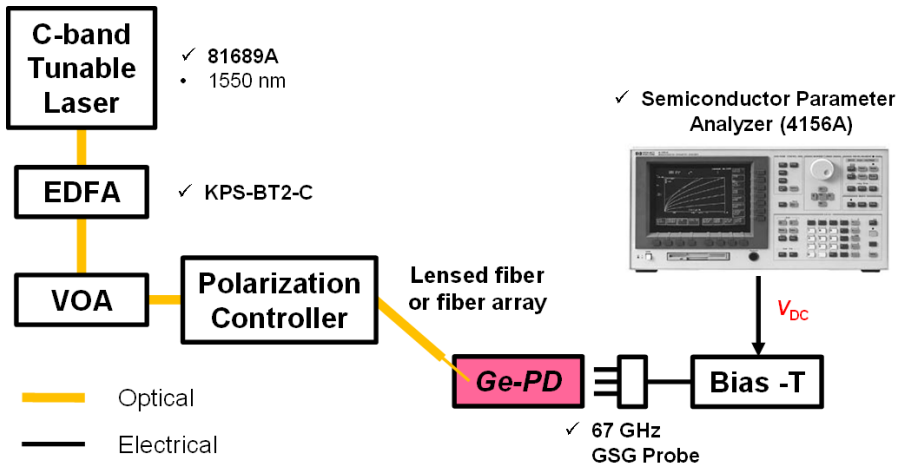

Fig. 3-4. Linearity measurement setup for waveguide-type Ge-PD.

Fig. 3-5 shows measured photocurrent-optical power characteristics at different bias voltages to Ge-VPD. The slope in this figure means responsivity and from this, the linearity characteristics according to different optical power are also investigated. As can be seen in Fig. 3-5, photocurrents saturate and at higher reverse bias voltages, linear characteristics are not maintained at higher input optical power due to the space charge screening effect [32]. From this linearity measurement, optical power dependency of Ge-PD can be investigated for high power application such as Radio-over-Fiber technology.

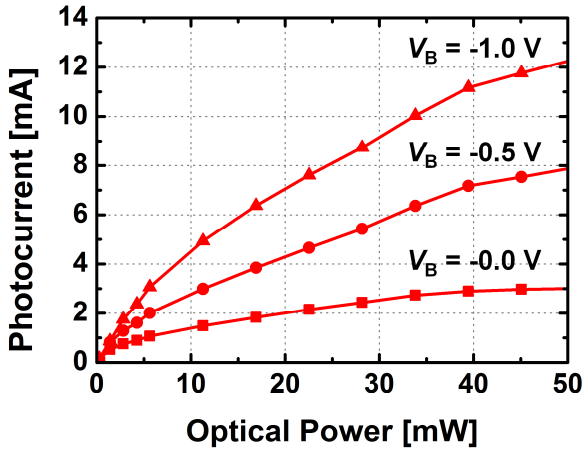

Fig. 3-5. Measured photocurrent-optical power characteristics of Ge-VPD at different reverse bias voltages.

3.2. AC Measurements

3.2.1. Electrical Reflection Coefficient Characteristic

Fig. 3-6 show measurement setup for electrical reflection coefficient (s_{22}) and it is measured with a network analyzer (PNA; Agilent E8361C). For accurate electrical *S*-parameter measurements, 1-port calibration including rf probe is performed using calibration kit substrate carefully.

This reflection coefficient implies impedance characteristics and this is composed of real and imaginary parts which represent resistive and capacitive or inductive components, respectively. The normalized reflection coefficient as 50-Ω terminator from 100 MHZ to 40 GHz at –1 and –4 V can be depicted on smith chart as shown in Fig. 3-7 and this helps to investigate and understand impedance characteristics of Ge-PD as various conditions of different frequencies or bias voltages. Fig. 3-7 shows resulting measured results at –1 and –4 V. As can be seen in this figure, for different reverse bias voltages, Ge-VPD has almost same real part but larger imaginary part for impedance, which represents it has almost same resistive component but smaller capacitive component and which can be easily understood that Ge-VPD

has smaller *RC* time constant at higher reverse bias voltages. This is because, for p-i-n junction diode, the depletion region is increased as reverse bias voltage is increased resulting in decreased depletion capacitance.

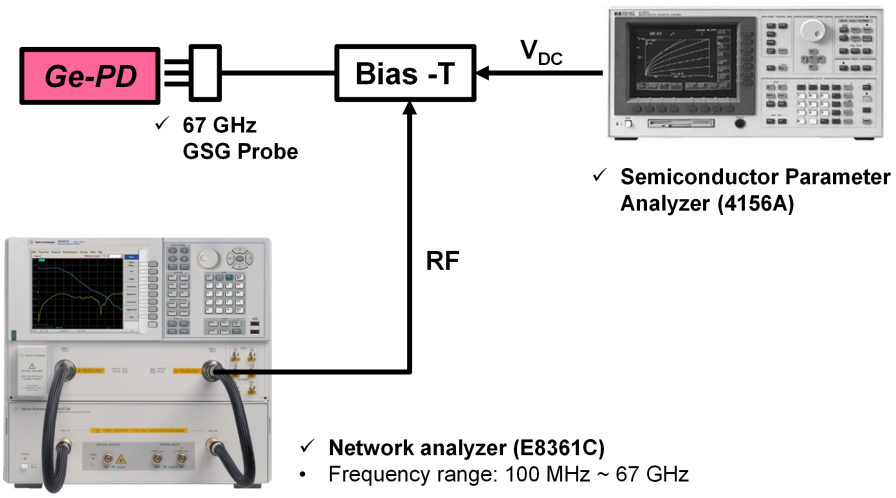

Fig. 3-6. Electrical reflection coefficient measurement setup for waveguide-type Ge-PD.

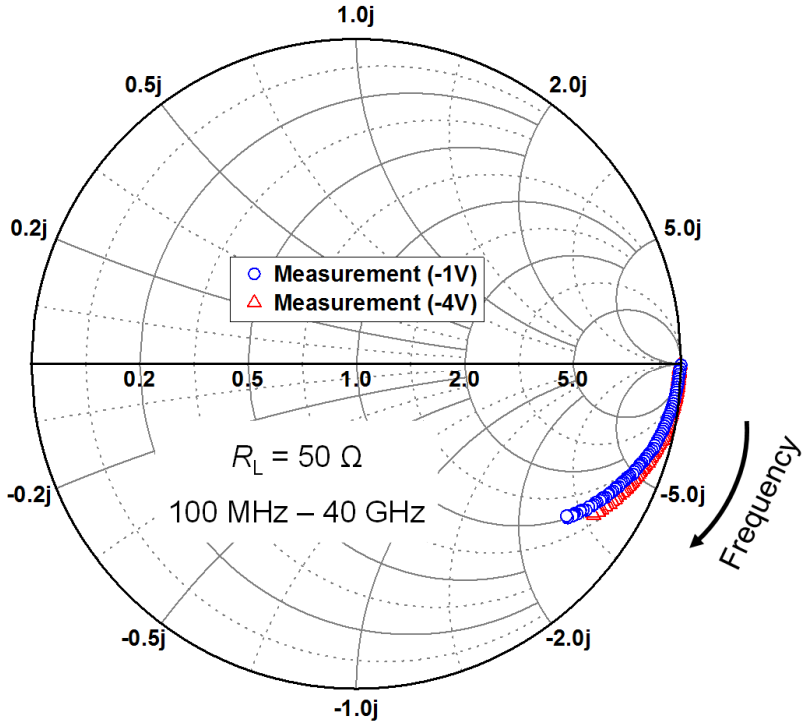

Fig. 3-7. Measured electrical reflection coefficients using electrical *S*-parameter measurement results (s_{22}) for Ge-VPD at –1 and –4 V from 100 MHZ to 40 GHz.

3.2.2. Photodetection Frequency Response Characteristic

Fig. 3-8 shows measurement setup for photodetection frequency response (S_{21}) and they are measured using a lightwave component analyzer (LCA; Agilent N4373D). Modulated input optical signal generated by LCA is injected to grating coupler through lensed fiber or fiber array and output electrical signal get into LCA. For accurate measurements, all electrical lines and probe are calibrated using calibration kit substrate carefully. DC bias voltages are applied using semiconductor parameter analyzer (HP 4156A).

Fig. 3-9 shows normalized measured photodetection frequency responses from 100 MHZ to 40 GHz with –8-dBm optical power into Ge-VPD biased at –1 and –4 V. Photodetection bandwidths at –1 and –4 V are 27 and 35 GHz, respectively.

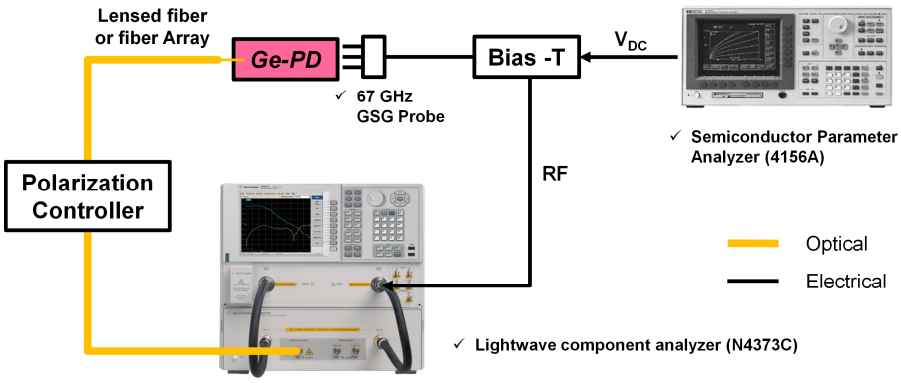

Fig. 3-8. Photodetection frequency response measurement (s_{21}) setup for waveguide-type Ge-PD.

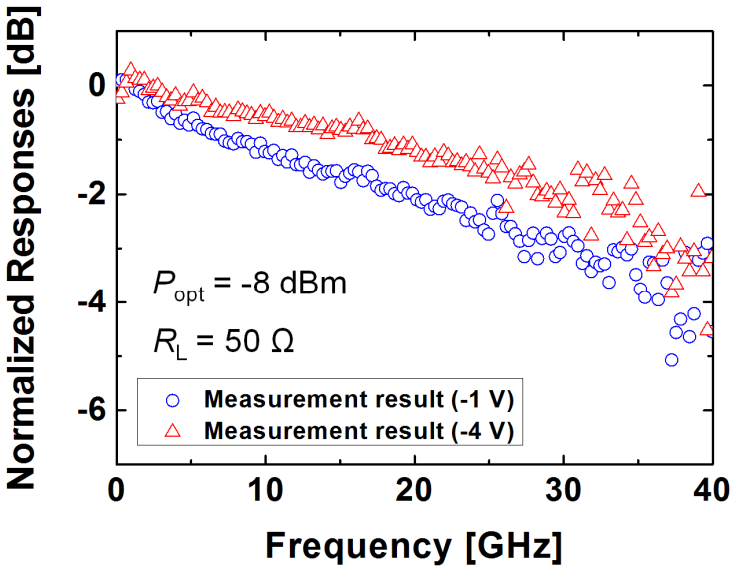

Fig. 3-9. Measured photodetection frequency response results (s_{21}) for Ge-VPD at –1 and –4 V.

3.3. Noise Measurement

Fig. 3-10 shows measurement setup for noise of Ge-PD using a spectrum analyzer (Agilent N9020A). Since the measured noise level of Ge-VPD is less than the measurement sensitivity of spectrum analyzer, two commercially available low-noise amplifiers (LNAs) having 62-dB gain and 3-dB noise figure are used in cascade. Bias voltages are applied to Ge-VPD through bias-T.

Noise can be represented by noise power spectral density (dBm/Hz or W/Hz) and this can be measured by the spectrum analyzer. As can be seen from noise measurement setup in Fig. 3-10, noise is sum of emitted noise by PD as well as noise generated by the LNA, bias-T, and spectrum analyzer and sum of those noises, $P_o(f)$ are derived with the following equation [33]:

$$P_{\mathrm{o}}(f) = 10\log[\mathrm{g}\times(10^{\frac{P_{\mathrm{PD}}(f)-L_{\mathrm{probe}}(f)-L_{\mathrm{B\text{-}T}}(f)}{10}} + (nf-1)k_{\mathrm{b}}T] - L_{\mathrm{cable}}(f). \quad (3.1)$$

Here, $P_o(f)$ is output noise spectral density at the output of LNA in dBm/Hz measured by spectrum analyzer, g is the gain of LNA in a linear scale, $P_{\mathrm{PD}}(f)$ is the noise power spectral density of Ge-PD, $L_{\mathrm{probe}}(f)$, $L_{\mathrm{B\text{-}T}}(f)$, and $L_{\mathrm{cable}}(f)$ are insertion loss of rf probe, bias-T and rf cable, nf is noise figure of LNA in a linear scale, and k_b is

Boltz-mann's constant, and T is temperature in Kelvin, respectively.

To exclude noise from the spectrum analyzer itself, noise spectral density is also measured by changing rf probe to 50-Ω terminator. The difference between noise emitted by Ge-PD and 50-Ω terminator represents emitted noise spectral density by Ge-PD excluding noise from the spectrum analyzer [33].

From this calibration process, measured noise power spectral densities of Ge-VPD from 50 to 850 MHZ at –1 V under –8-dBm optical power are shown in Fig. 3-11. As can be seen in this figure, the Ge-VPD noise spectral density consists of the spectrally-dependent flicker noise dominant at low frequencies and the constant shot and thermal noises dominant at high frequencies [33]. Since, noise is sensitively affected by various elements such as temperature, input optical power, and resistive components, stable measurement conditions should be arranged.

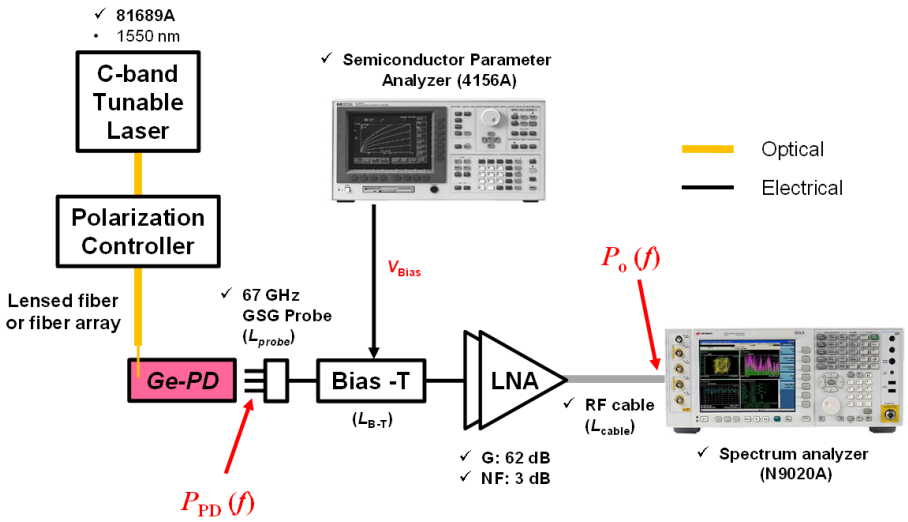

Fig. 3-10. Noise measurement setup for waveguide-type Ge-PD.

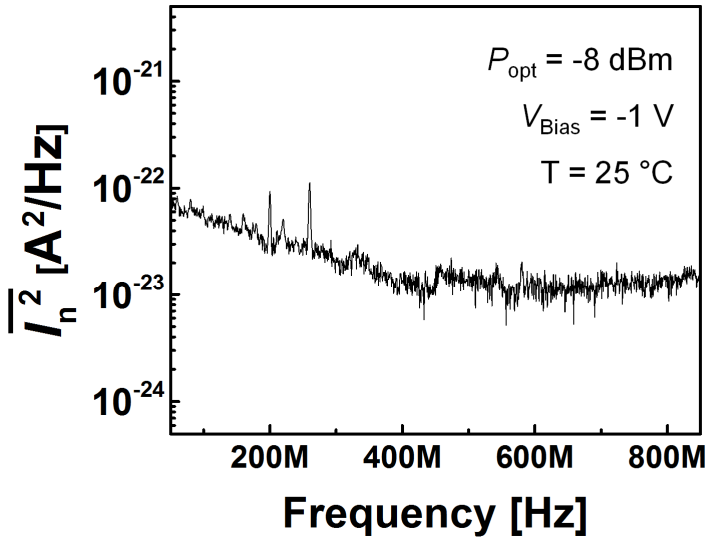

Fig. 3-11. Measured noise power spectral density for Ge-VPD at –1 V.

3.4. Summary

This chapter introduces DC, AC, and noise measurement setup for characterizing waveguide-type Ge-PD on-wafer probing. From DC measurement setup, the characteristics of current-voltage and nonlinear photocurrent can be investigated as different wavelength, optical power, and different bias voltages. From AC measurement setup, electrical *S*-parameter, photodetection frequency response are measured and from this, frequency-dependent characteristics of waveguide-type Ge-PD can be investigated and these are used for model parameter extraction used in equivalent circuit model. In addition, from noise measurement, noise can be characterized as different frequencies, input optical power, and bias voltages and this noise measurement is useful for low-noise photodetector investigations for such as bio-sensor application dealing with very low optical signal like noise.

4. Simulation for Waveguide-Type Ge-PDs

4.1. Introduction

The operation principle of PD is converting input optical signals to output electrical signals. To investigate and analyze PD characteristics and performance optimization, both optical and electrical PD simulations are needed. The optical and electrical properties of PD can be interpreted using the FDTD and TCAD simulations, respectively.

FDTD method represents direct discretization of Maxwell's differential equations by finite differences which were first established by Yee as a 3-D solution of Maxwell's curl equations [34]. This can perform a full-vector simulation of wide range of optical devices such as ring resonator, grating coupler, directional coupler, and photodetector. In this dissertation, optical simulation for calculating optical generation rates in absorption region of waveguide-type Ge-PD is done by Lumerical FDTD tool and this is introduced in chapter 4.2.

TCAD is physical-based simulation tool and this model the behavior of the semiconductor device using various fundamental physical models such as drift-diffusion and Poisson equations. If the

information of optical generation rates can be imported to TCAD, photogenerated-carrier transport occurred in waveguide-type Ge-PD is interpreted by TCAD simulation and this will be helpful to investigate dynamics of photogenerated carrier as well as determination of photogenerated current source model parameters used in equivalent circuit model. In chapter 4.3, the procedure for TCAD Sentaurus with Lumerical FDTD tool is shown. From that, electric-field, current-voltage characteristic, electrical S-parameter, and photodetection frequency response can be simulated and this will be a great help to investigate photodetectors.

4.2. Lumerical FDTD Simulation

3-D FDTD simulation for calculating optical generation rates in waveguide-type Ge-PD can be done in the following steps. Here, Ge-VPD is used for an example [35].

First, the 3-D device structure of Ge-VPD is realized in Lumerical FDTD as shown in Fig. 4-1 [35]. The properties of materials, mode source, and boundary conditions are configured for 3-D FDTD simulation and after simulation, spatially distributed electric field, $\vec{E}(\lambda)$ and magnetic field, $\vec{H}(\lambda)$ can be obtained as shown in Fig. 4-2 (a) and (b).

To determine the amounts of photogenerated carriers in Ge absorption region, absorption power per unit volume (P_{abs}) is calculated from divergence of the Poynting vector, $\vec{P}(\lambda) = \vec{E}(\lambda) \times \vec{H}(\lambda)$ as shown in followed equation:

$$P_{\text{abs}} = -0.5 \times \text{real}(\vec{\nabla} \cdot \vec{P}(\lambda)) . \tag{4.1}$$

Here, $\vec{P}(\lambda)$ is Poynting vector which represents the directional energy flux density of an electromagnetic field. However, since the divergence calculations tend to be very sensitive to numerical problems, Eq. (4.1) is modified to numerically stable form of Eq. (4.2) [34]:

$$P_{\text{abs}} = -0.5 \times \omega \left|\vec{E}(\lambda)\right|^2 \text{imag}[\varepsilon(\lambda)]. \quad (4.2)$$

Here, ω is angular frequency of input optical signal and $\varepsilon(\lambda)$ is permittivity of material at given wavelength optical signal. From Eq. (4.2), P_{abs} can be calculated from $\vec{E}(\lambda)$ and the imaginary part of $\varepsilon(\lambda)$. Assuming that each absorbed photon generates one electron-hole pair, the number of photo-generated carriers per unit volume (g) same as optical generation rate can be calculated by dividing by the energy per photon as shown in Eq. (4.3) [34]:

$$g = \frac{P_{\text{abs}}}{\hbar\omega} = \frac{-0.5 \times \left|\vec{E}(\lambda)\right|^2 \text{imag}[\varepsilon(\lambda)]}{\hbar}. \quad (4.3)$$

Here $\hbar$ is reduced Plank constant. The g can be calculated using scripting language supported by Lumerical FDTD. For your information, the syntax of scripting language is very similar to that in MATLAB and this is very useful for data calculation and analysis.

Fig. 4-2 (c) shows corresponding calculated optical generation rate (g) at the wavelength of 1.55-μm light. The direction of these figure is same as light propagation (Y-Z axis at X=0). As can be seen in this figure, absorption rate is decreased as increased length of waveguide-type Ge-PD.

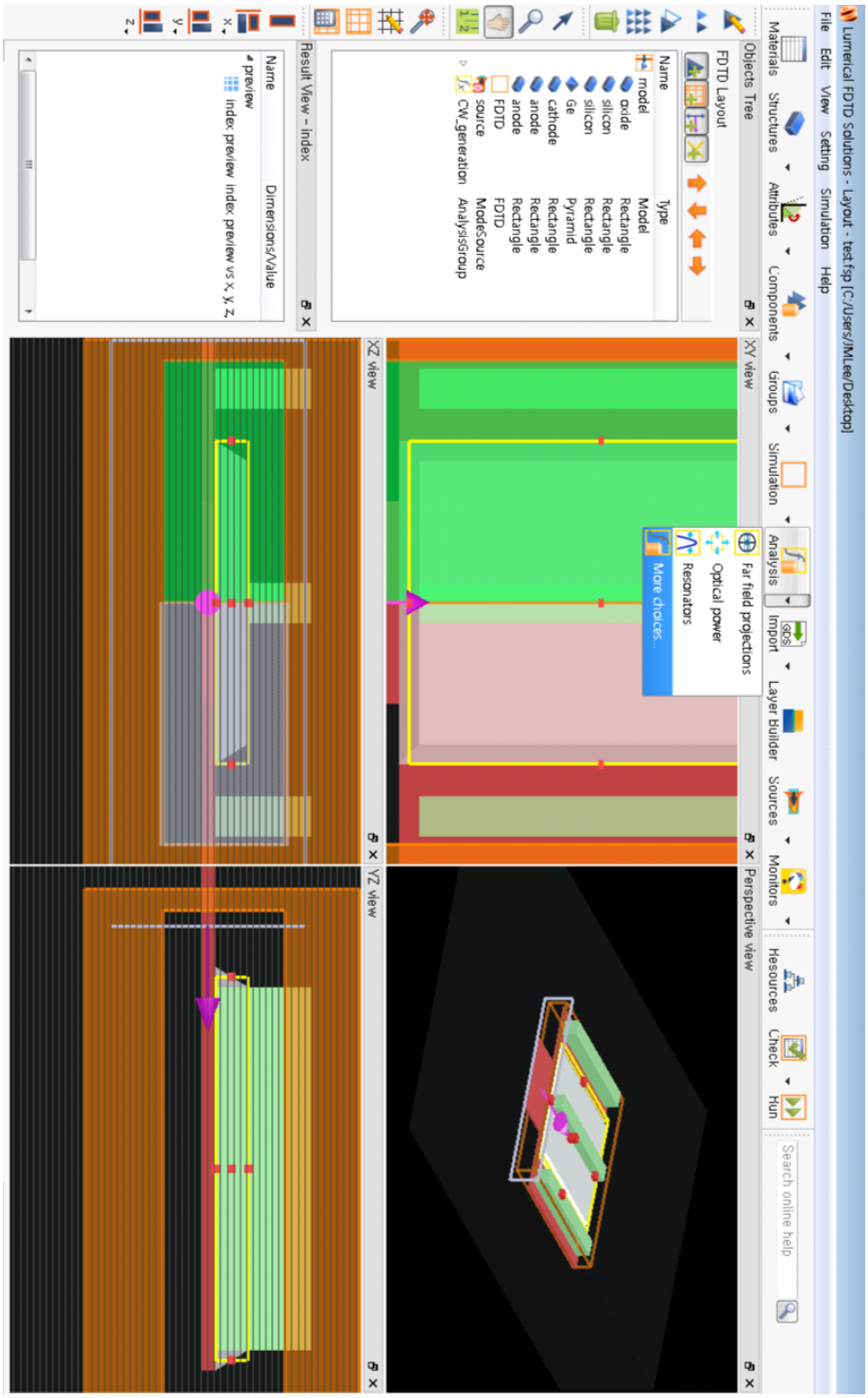

Fig. 4-1. Lumerical FDTD simulation environment.

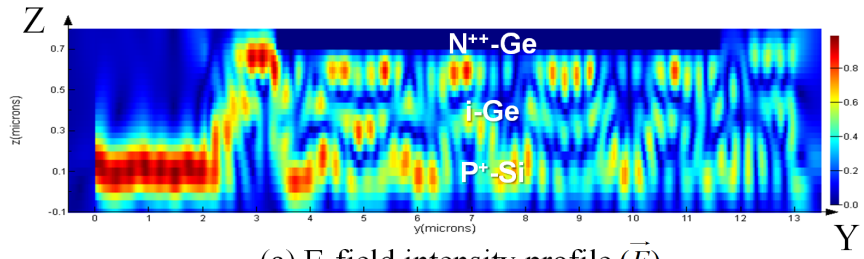

(a) E-field intensity profile ($\vec{E}$)

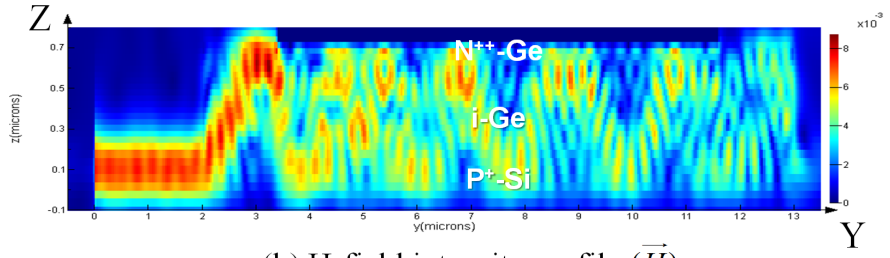

(b) H-field intensity profile ($\vec{H}$)

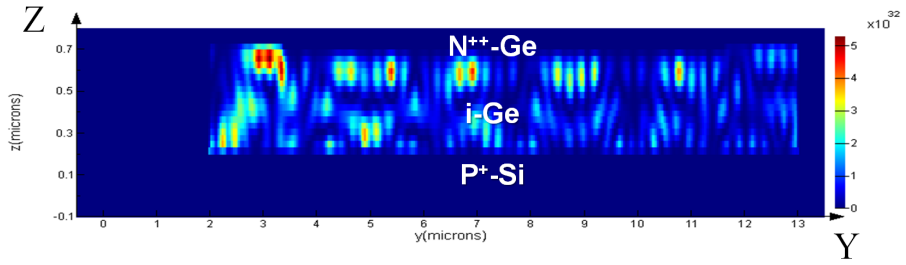

(c) Optical generation profile (g)

Fig. 4-2. FDTD simulated (a) electric-field intensity, (b) magnetic-field intensity, and (c) optical generation rate profiles along the light propagation direction at X=0.

4.3. TCAD Sentaurus Simulation

4.3.1. Carrier Transport

To investigate the electron and hole carrier transports in PD, Poisson's equation coupled with charge current continuity equation should be solved. Total charge is modeled by followed Poisson's equation:

$$\frac{\partial E}{\partial x} = (\frac{1}{\varepsilon}) \cdot [q(p - n + N_D^+ - N_A^-) - Q_T] . \quad (4.4)$$

The n and p in above equation are calculated by solving the continuity equations as shown in Eq. (4.5) and (4.6) and coupled with carrier drift-diffusion equations in Eq. (4.7) and (4.8).

$$\frac{\partial n}{\partial t} = \frac{1}{q}\frac{\partial J_n}{\partial x} + G_n - R_n , \quad (4.5)$$

$$\frac{\partial p}{\partial t} = \frac{1}{q}\frac{\partial J_p}{\partial x} + G_p - R_p , \quad (4.6)$$

$$J_n = qn\upsilon_n(E) + qD_n\frac{\partial n}{\partial x} , \quad (4.7)$$

$$J_p = qn\upsilon_p(E) + qD_p\frac{\partial p}{\partial x} . \quad (4.8)$$

Here, parameters used in these equations are listed in Table 4-1.

TABLE 4-1
PARAMETERS USED TO PHYSICAL MODEL.

PARAMETERS	DESCRIPTION
E	Electric field
ε	Permittivity
n, p	Electron and hole concentrations
N_D^+, N_A^-	Ionized donor and acceptor impurity concentrations
Q_T	Total charge caused by trap
J_n, J_p	Electron and hole current densities
G_n, G_p	Electron and hole generation rates
R_n, R_p	Electron and hole recombination rates
υ_n, υ_p	Electron and hole velocity
D_n, D_p	Electron and hole diffusion constants

4.3.2. Procedures for Waveguide-type Ge-PD Simulation

Sentaurus Device under TCAD Sentaurus tool is a semiconductor numerical device simulator, capable of simulating electrical, optical, and thermal characteristics [37]. It supports two different types of simulations: one is a carrier transport simulation and another is a mixed-mode simulation. For carrier transport simulation in Sentaurus Device, the transportation of carriers is solved by using drift-diffusion, thermodynamic, hydrodynamic, and Monte Carlo transport, as well as quantum transport, based on density gradient model [37]. Mixed-mode simulation supports simulation on small circuits in which several circuit elements, including physical devices simulated by carrier transport simulation and lumped elements. The procedures of carrier transport and mixed-mode simulation for waveguide-type Ge-PD are shown in Fig. 4-3 and 4-4 and these are introduced in this chapter. Sentaurus Structure Editor, Sentaurus Device, Sentaurus Visual, and Inspect, and Lumerical FDTD tools are used for waveguide-type Ge-PD simulation and their functions are simply introduced in this chapter.

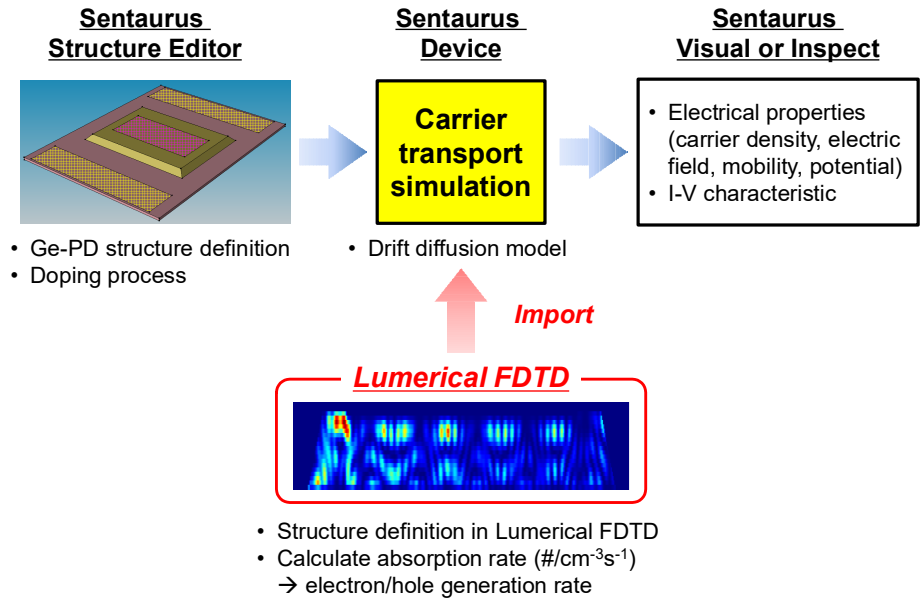

Fig. 4-3. Carrier transport simulation procedure.

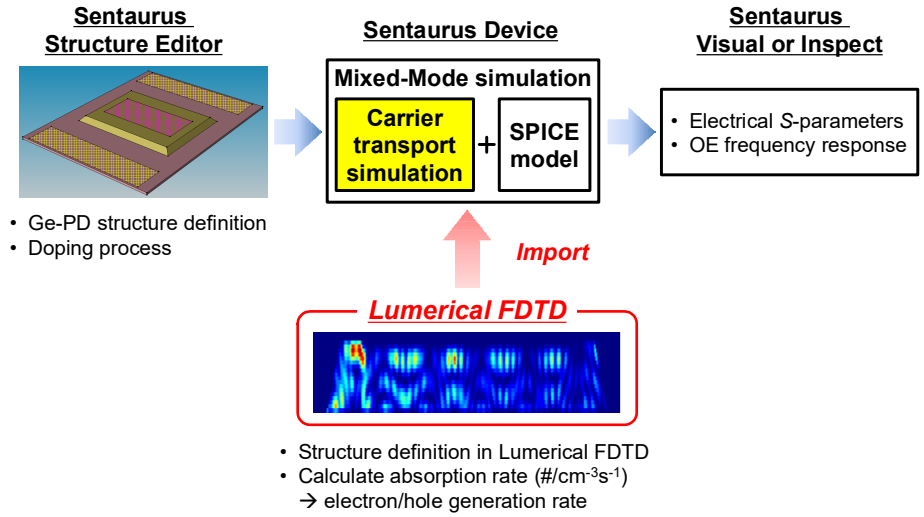

Fig. 4-4. Mixed-mode simulation procedure.

A. Structure Definition in Sentaurus Structure Editor

For carrier transport and mixed-mode simluation, first, the Ge-VPD structure under consideration is given and this can be drawn with materials defined in Sentaurus Structure Editor as shown in Fig. 4-5. Doping profiles are also defined to form p- and n-doped regions with the doping process information provided by the IME foundry service. In IME doping process, Boron and Phosphorus were implanted with same condition of 4×10^{15}-cm^{-2} dose and 10-keV energy and thermally activated at 500°C for 5 mins and 1030°C for 5 secs to form highly p-doped Si (P^{++}-Si) and highly n-doped Ge (N^{++}-Ge) regions, respectively [30]. Fig. 4-6 (a) and (b) shows 3-D and 2-D view of Ge-VPD after Boron and Phosphorus ion implantations.

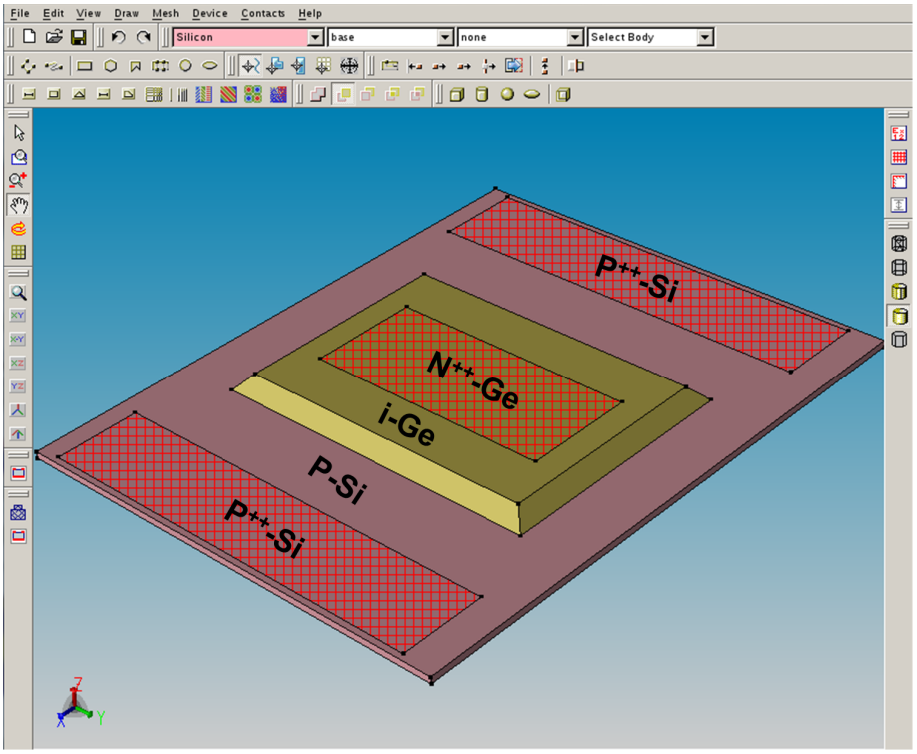

Fig. 4-5. Device structure definition of Ge-VPD in TCAD Sentaurus Structure Editor.

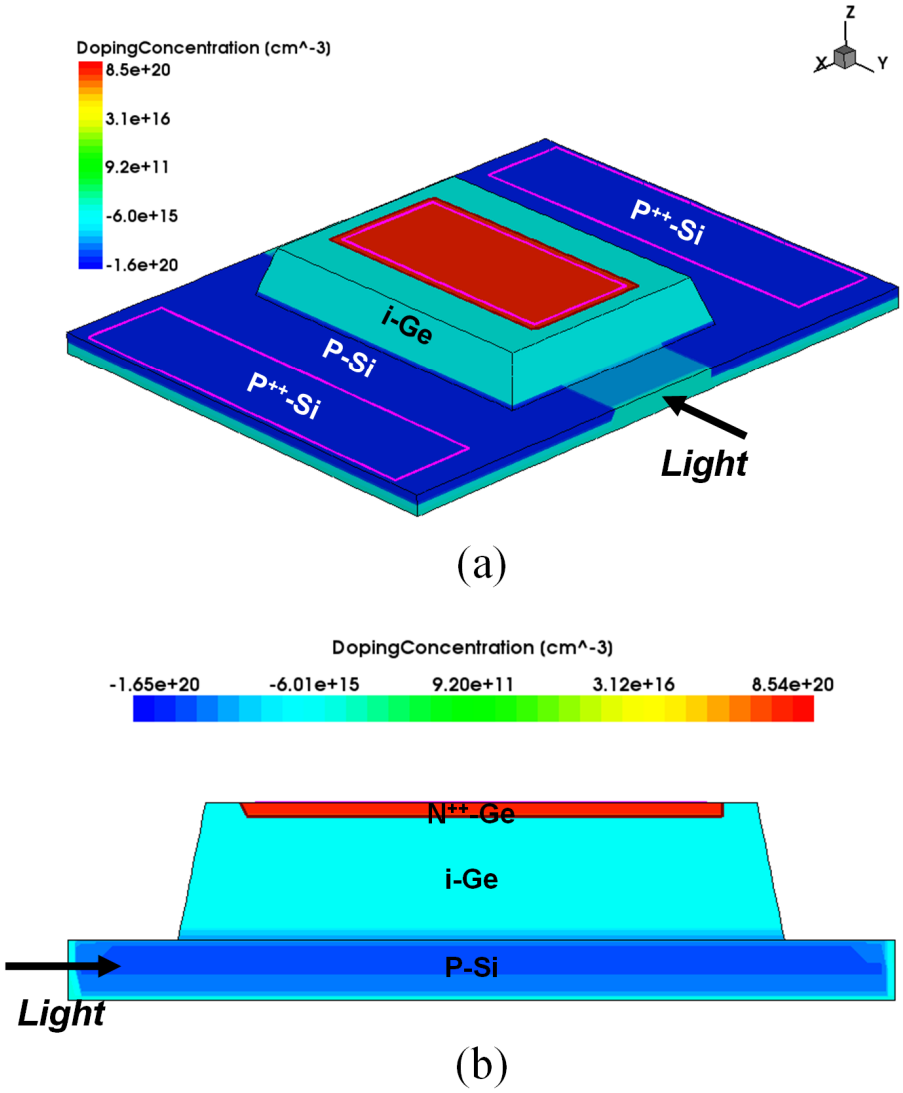

Fig. 4-6. Ge-VPD with doping process: (a) scaled 3-D view and (b) scaled 2-D view along the light propagation direction at X=0.

B. Importing Optical Generation Rate from Lumerical FDTD to TCAD Sentaurus

As described in Eq. (4.5) and (4.6), optical generation rate for electron and hole, G_n and G_p are required for optoelectronic simulation. In this dissertation, optical generation rates are calculated by Lumerical FDTD as explained in chapter 4.2. Since different meshing strategy at Lumerical FDTD and TCAD Sentaurus are used and supported file format and file name extension are different, careful jobs for matching mesh and rearranging are performed using MATLAB to be available in TCAD Sentaurus. Fig. 4-7 shows successfully imported optical generation rates from Lumerical FDTD to TCAD Sentaurus.

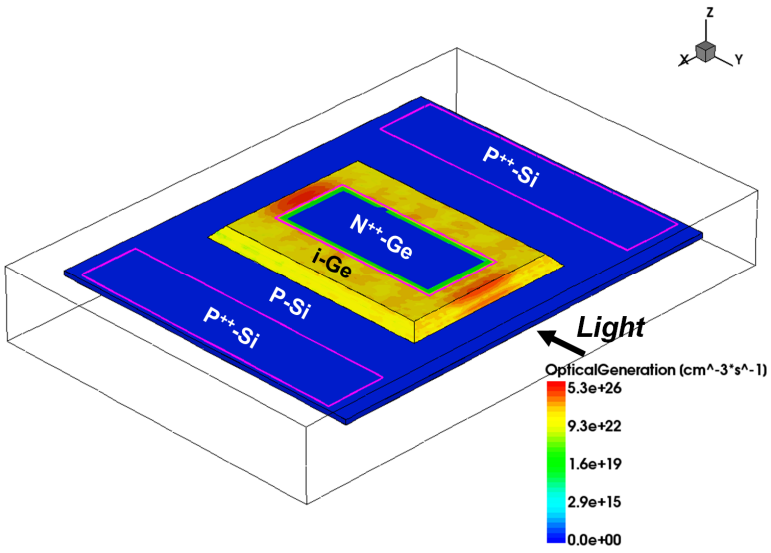

Fig. 4-7. Imported optical generation rates in TCAD Sentaurus.

C. Carrier Transport & Mixed-Mode Simulation

After importing optical generation rate to TCAD, now, optoelectronic simulation can be performed by Sentaurus Device as carrier transport and mixed-mode simulations.

Carrier transport simulation with drift diffusion model solves physical equations from Eq. (4.4) to Eq. (4.8) numerically, and as a result, electrical properties such as carrier density, electric field, mobility, and potential in photodetector can be simulated.

As shown in Fig. 4-8, the summarized script for carrier transport simulation is consists of several command lines for File, Electrode, Physics, Math, Solve, and Plot sections. In File section, input defined structure from Sentaurus Structure Editor and output plots and extracted data are designated. Electrode section is used to define the name and materials of electrodes for biasing. To apply physical model in Sentaurus Device simulation, models for mobility, recombination, and trap level are needed to define. Doping and electric-field dependent mobility models and Shockley-Read Hall and band-to-band recombination models can be used in simulation. The Math section is used to control the simulator numeric. Here, calculation solver configuration and the number of iteration are defined for effective solving. The Solve section is usually used to how bias voltage is

applied to device and electrical AC or optical AC simulation can be also activated in this section. The Plot section is used to specify the variables to be visualized in Sentaurus Visual.

Mixed-mode simulation is simulation on small circuits including several circuit elements, physical devices simulated by carrier transport simulation and lumped elements. And as a result, electrical *S*-parameter and photodetection frequency response can be simulated. The summarized script for mixed-mode simulation is shown in Fig. 4-9 and this script includes not only the definitions of each individual element in the circuit, but also a netlist showing the connectivity between the elements. All these things are defined in System section.

```
File {
        Grid = "*_msh.tdr"          * input file definition
        Parameter = "*.par"         * parameter information
        Plot = "*_des.tdr"          * output plot file definition
        Current = "*_des.plt"       * output data file definition
}

Electrode {
        Anode
        Cathode
}

Physics {* physical model definition
        Mobility ( … )              * mobility model
        Recombination( … )          * recombination model
        Traps ( … )                 * trap model
}

Plot {  * variable list for visualization
        Doping DonorConcentration AcceptorConcentration Density
        Current ElectricField Potential Velocity DriftVelocity
        Mobility DiffusivityMobility
        Potential SpaceCharge ElectricField
}

Math {  }

Solve { * solver setting for carrier transport simulation
        Coupled (Iterations=50) {Poisson}
        Coupled (Iterations=15) {Hole Poisson}
        Coupled (Iterations=15) {Electron Hole Poisson}

        QuasiStationary ( … )               * bias voltage setting
        { coupled {Hole Electron Poisson} }
}
```

Fig. 4-8. Summarized script for carrier transport simulation using Sentaurus Device simulation.

```
File   {
          ACExtract =”File name”      * output AC simulation file definition
}

Device {  * device simulation setting under consideration

          File { … }

          Electrode { … }

          Physics { … }

}

System { … }        * netlist definition for electrical S-parameter and photodetection
                      frequency response simulation

Math { … }

Solve {
          Coupled (Iterations=50) {Poisson}
          Coupled (Iterations=15) {Hole Poisson}
          Coupled (Iterations=15) {Electron Hole Poisson}

          QuasiStationary ( … )          * bias voltage setting

          { coupled {Hole Electron Poisson} }

          * electrical S-parameter simulation setting
          ACCoupled( StartFrequency = 100e6 EndFrequency = 40e9
                     NumberOfPoints = 10 linear Node Exclude)
          {Poisson Electron Hole}

          * optical AC simulation setting
          ACCoupled (StartFrequency=100e6 EndFrequency=40e9
                     NumberOfPoints = 10 decade Node Optical)
          { Poisson Electron Hole }
}
```

Fig. 4-9. Summarized script for mixed-mode simulation using Sentaurus Device simulation.

D. Analysis Based on Simulation Results

From TCAD Sentaurus simulation with Lumerical FDTD, not only electrical properties such as doping concentration, electron and hole densities, electric field, potential voltage, and mobility but also electrical *S*-parameter, photodetection frequency response can be simulated. From these, photogenerated carrier transportation in waveguide-type Ge-PD can be interpreted and investigated numerically.

Fig. 4-10 (a) and (b) show carrier transport simulated electric-field and imported optical generation-rate profiles of Ge-VPD at –1 V along the light propagation direction. As can be seen in these figures, there are regions having small electric field at the edge of Ge absorption region and especially, considerable light absorptions are existed at the front of Ge absorption region having not sufficiently large electric-field intensity. This is because N^{++}-Ge region cannot extend to the very beginning of the PD due to the design rule, which requires 1.2-μm spacing between N^{++}- and i-Ge layers. Photogenerated carriers occurred in this region do not experience strong drift and, as a result, have to transport by the slow diffusion process. At higher reverse bias voltage, these regions are decreased due to increased depletion region.

Fig. 4-11 and 4-12 shows mixed-mode simulation results of electrical reflection coefficient and photodetection frequency response

results for waveguide-type Ge-PD at –1 V from 100 MHZ to 40 GHz, respectively. From these, the information of photodetector input impedance can be extracted and photogenerated carrier transport can be interpreted on frequency domain and it helps to understand dynamics of photogenerated carriers.

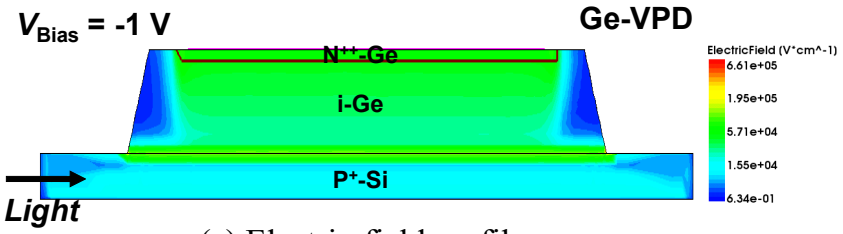

(a) Electric-field profile

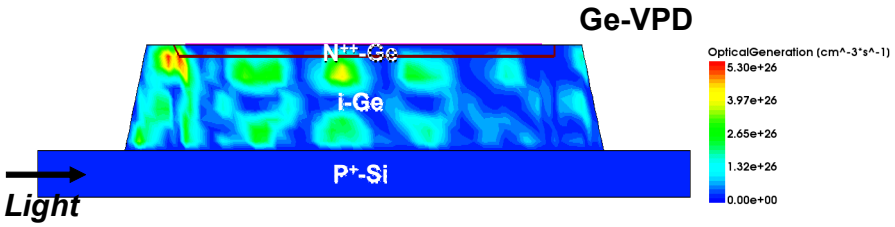

(b) Optical generation-rate profile

Fig. 4-10. TCAD simulated result of Ge-VPD: (a) electric-field profile at –1 V and (b) optical generation-rate profile along the light propagation direction at X=0.

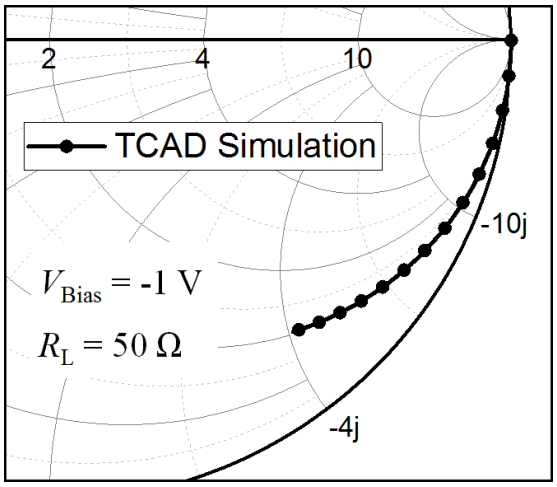

Fig. 4-11. TCAD simulated electrical reflection coefficient result of Ge-VPD at –1 V from 100 MHZ to 40 GHz.

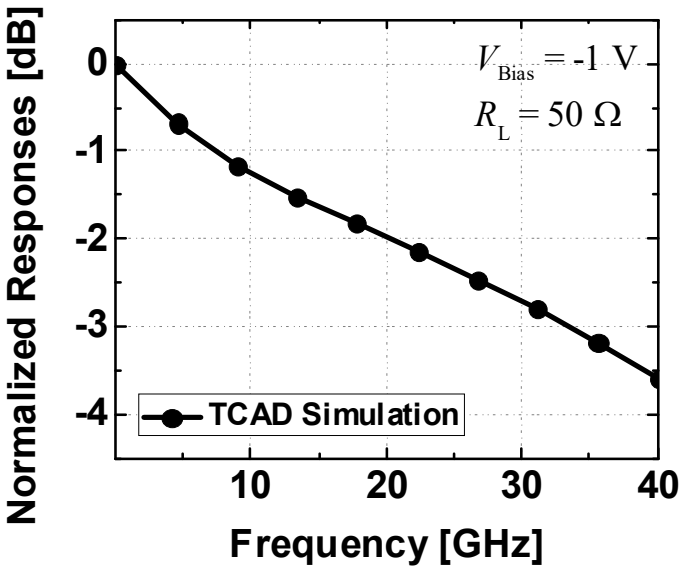

Fig. 4-12. TCAD simulated photodetection frequency response of Ge-VPD at –1 V from 100 MHZ to 40 GHz.

4.4. Summary

In this chapter, co-simulation technique for simulating waveguide-type Ge-PDs is developed using TCAD Sentaurus and Lumerical FDTD tools. By importing calculated optical generation rates by Lumerical FDTD to TCAD Sentaurus, the transportation of photogenerated carriers can be interpreted by solving carrier transport equations in TCAD Sentaurus. From this simulation, it can be concluded that photogenerated carriers experience sufficiently small as well as large electric fields in Ge absorption region which is believed that the reason of low-frequency roll-off characteristics in photodetection frequency responses observed in some waveguide-type Ge-PDs which is discussed in chapter 1.4. In addition, this simulation is very useful to identify how fast and how much photogenerated carriers are transported in Ge absorption region, and as a result, this contributes to model photogenerated current sources in equivalent circuit model which is dealt with in next chapter.

5. Equivalent Circuit Model of Waveguide-Type Ge-PD

In previous chapter 4, it is concluded that which regions are photogenerated carriers in absorption region of Ge-VPD experience sufficiently large and small electric fields. However, discussed in chapter 1.4, typical equivalent circuit model has not considered that and most photogenerated carriers are assumed as having sufficiently large electric field for carrier drift and this is represented as one current source having single-pole frequency determined by drift velocity.

In this chapter 5.1, the modified equivalent circuit model of waveguide-type Ge-PD is introduced and the difference with typical model is discussed. In chapter 5.2 and 5.3, parameter extraction procedures for *RC* passive components and current source models used in model are introduced, respectively. Chapter 5.4 shows applications of equivalent circuit model and from this, each time constant effect to photodetection frequency response of waveguide-type Ge-PD are clarified to find out the bandwidth limitation.

5.1. Modified Equivalent Circuit Model

To represent transportation of photogenerated carriers in equivalent circuit model, one current source model having single-pole frequency response is usually used as show in Fig. 1-9. However, for Ge-VPD and Ge-LPD in this dissertation, there are regions having small electric field for photogenerated carriers in Ge absorption region, which results in low-frequency roll-off characteristics. For Ge-VPD, these regions are located at the edge of Ge absorption region in Fig. 5-1 and for Ge-LPD, at charge neutral region in n- and p-doped regions in Fig. 5-2.

To consider this for accurate waveguide-type Ge-PD modeling, as shown in Fig. 5-3(a), modified equivalent circuit model is proposed having three current sources: two for photogenerated carriers experiencing large and small electric fields as diffusion (I_1) and drift (I_2), respectively, and one for a noise current source, respectively. The frequency response of I_1 and I_2 can be modeled by a single time constant, τ_1 ($=1/2\pi f_1$) for I_1 and τ_2 ($=1/2\pi f_2$) for I_2, along with corresponding DC gain, A_1 and A_2, sum of which represents Ge-PD DC responsivity as graphically shown in Fig. 5-3(b) but is normalized to one for simplicity in this dissertation.

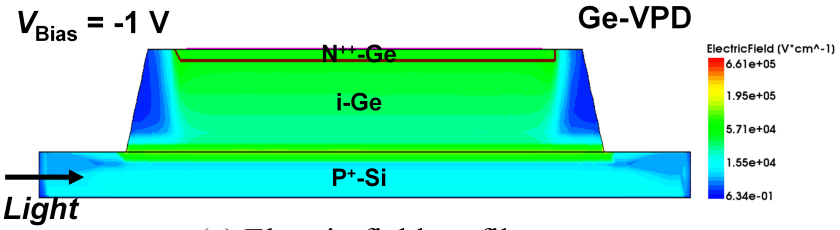

(a) Electric-field profile

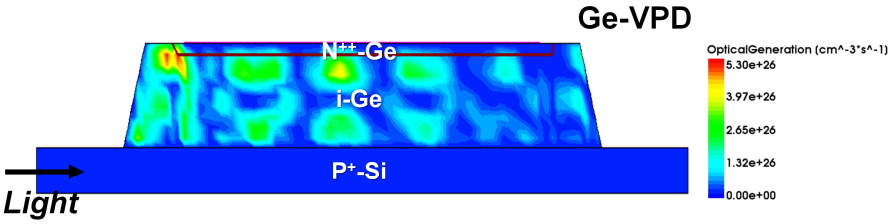

(b) Optical generation-rate profile

Fig. 5-1. (a) TCAD simulated electric-field distribution of Ge-VPD at –1 V and (b) simulated optical generation-rate profile along the light propagation direction at X=0.

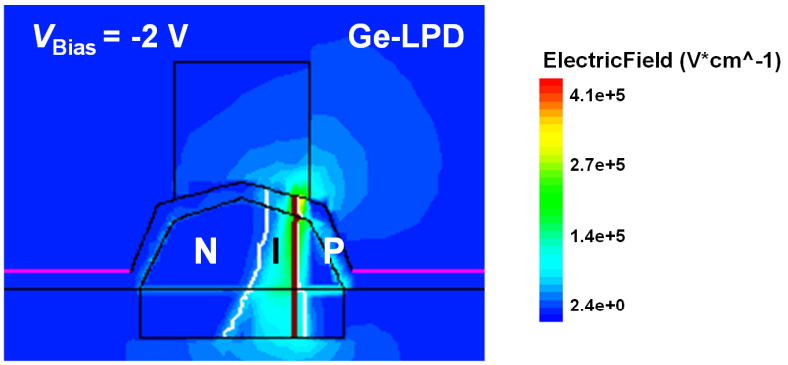

(a) Electric-field profile

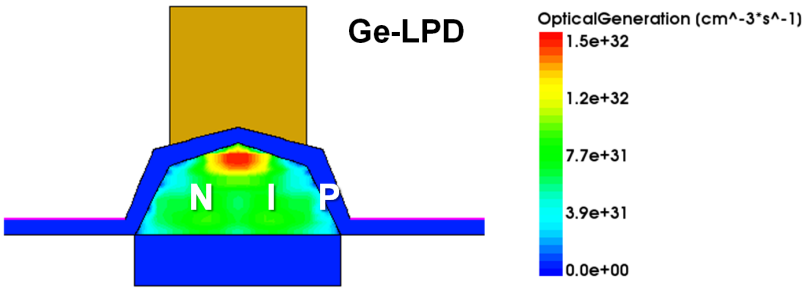

(b) Optical generation-rate profile

Fig. 5-2. (a) TCAD simulated electric-field distribution of Ge-LPD at –2 V and (b) simulated optical generation-rate profile.

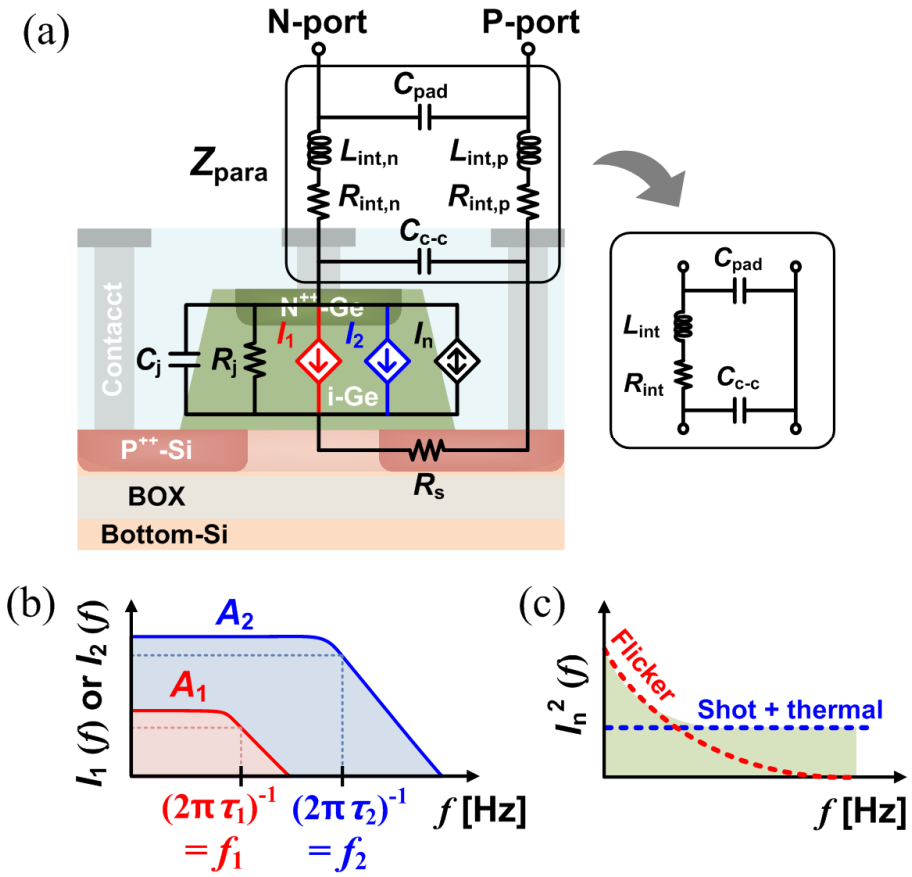

Fig. 5-3. (a) A modified equivalent circuit model of Ge-VPD, (b) frequency responses of photogenerated currents, and (c) noise characteristics.

This model also contains the noise current source I_n for the noises generated in the waveguide-type Ge-PD due to three different mechanisms shown in Fig. 5-3(c) and detailed model parameters are discussed in chapter 5.3.

In model, Z_{para} represents parasitic components due to the pads and interconnects, which must be considered for accurate modeling of waveguide-type Ge-PD dynamics. For *RC* passive component for p-i-n junction, R_s, C_j, and R_j are used and they are same as typical equivalent circuit model in chapter 1.4.

5.2. Parameter Extractions for RC Passive Components

5.2.1. Parasitic RLC Passive Components

As shown in Fig. 2-1(c) and Fig. 2-2(c), output current signals generated by Ge-VPD and Ge-LPD flow through signal and ground pads and this is modeled by Z_{para} in Fig. 5-3(a). This must be considered for accurate equivalent circuit model of Ge-VPD. As shown in Fig. 5-3(a), $R_{int,p}$, $R_{int,n}$ and $L_{int,p}$, $L_{int,n}$ represent parasitic resistances and inductances in the interconnects from P-port and N-port to the bottom metal layer, respectively. C_{pad} represents the parasitic capacitance between P- and N-port pads and $C_{c\text{-}c}$ is the capacitance between Ge-VPD metal contacts. For simplicity, we model these parasitic elements together with Z_{para} shown in inset of Fig. 5-3(a), in which $R_{int} = R_{int,p} + R_{int,n}$ and $L_{int} = L_{int,p} + L_{int,n}$.

In order to extract R_{int}, L_{int}, and C_{pad}, open and short test patterns are implemented on the same die as shown in Fig. 5-4(a) and (b), and their electrical *S*-parameters are measured from 100 MHZ to 40 GHz under –20-dBm rf test power using a vector network analyzer. Fig. 5-5(a) and (b) shows the measured reflection coefficients for open and short test

patterns. From measured real and imaginary parts of converted *S*- to *Y*- and *Z*-parameters, the values of C_{pad}, R_{int}, and L_{int} can be extracted and they are shown in Table 5-1. As can be seen in Fig. 5-5(a) and (b), measured and simulated results based on equivalent circuit model in Fig. 5-4(c) match very well.

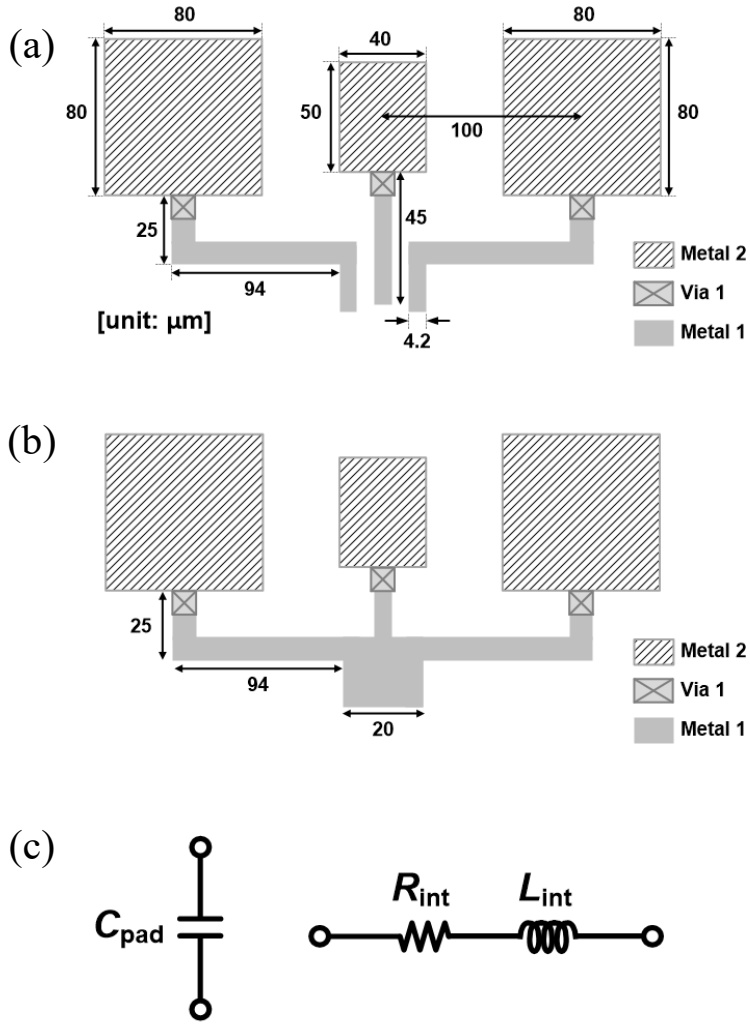

Fig. 5-4. (a) Open and (b) short test patterns, and (c) equivalent circuit of open and short test patterns.

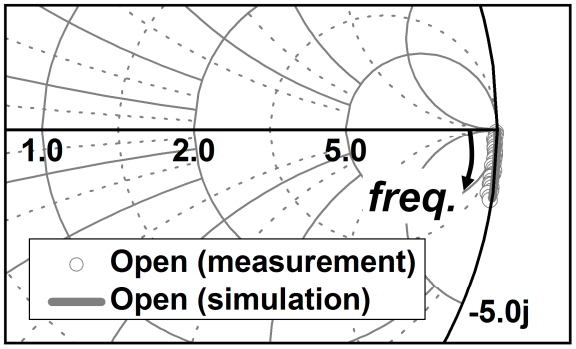

(a) Open test pattern

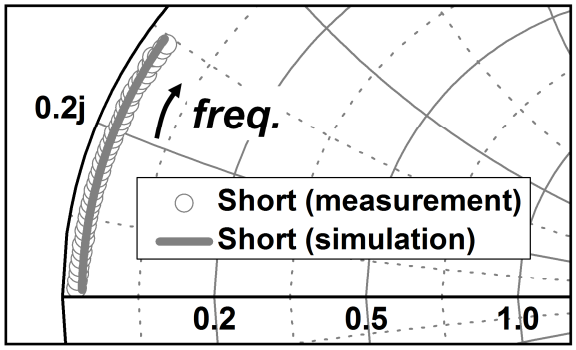

(b) Short test pattern

Fig. 5-5. Measured and simulated reflection coefficients of (a) open and (b) short patterns from 100 MHZ to 40 GHz under –20-dBm test power.

TABLE 5-1

EXTRACTED PARAMETERS FOR PAD AND INTERCONNECT

C_{pad} [fF]	R_{int} [Ω]	L_{int} [pH]
6.1	1.1	65

5.2.2. RC Passive Components for P-I-N Junction

After deembedding C_{pad}, R_{int}, and L_{int} to modified equivalent circuit model of Ge-VPD as shown in Fig. 5-3(a), parameters for p-i-n junction, R_s, C_j, and R_j can be obtained by parameter tuning and optimization based on the comparison of measured and simulated reflection coefficients using Agilent Advanced Design System tool.

Electrical *S*-parameters of Ge-VPDs are measured using lightwave component analyzer from 100 MHZ to 40 GHz at –1 and –4 V under –20-dBm test power. Fig. 5-6 shows well-matched measured and simulated reflection coefficients for Ge-VPD and extracted parameters for R_s, C_j, and R_j at –1 and –4 V are listed in Table 5-2. At higher reverse bias voltage, C_j is decreased due to wider depletion width, which results in smaller *RC* time constant. By using mixed-mode simulation, electrical *S*-parameters of Ge-VPDs at –1 V can be simulated as shown in Fig. 4-11 and these are well-matched to measured results.

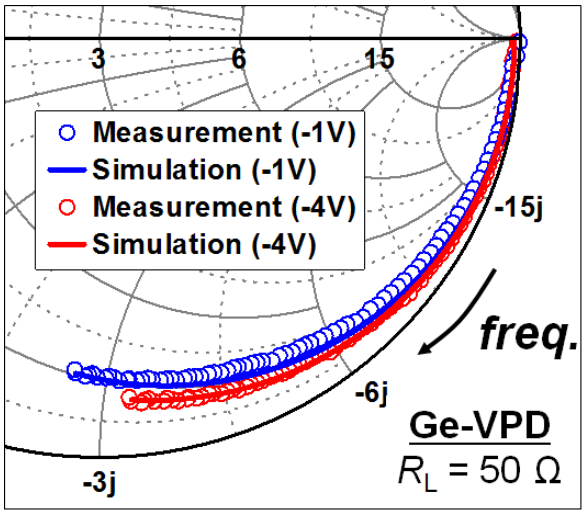

Fig. 5-6. Measured and simulated reflection coefficients for Ge-VPD with Z_{para} from 100 MHZ to 40 GHz at –1 and –4 V.

TABLE 5-2
EXTRACTED RC PARAMETERS AND RC TIME CONSTANT FOR GE-VPD WITH Z_{PARA}

	–1 V	**–4 V**
R_s [Ω]	88	
C_j [fF]	15.9	11.6
R_j [kΩ]	20	
$C_{c\text{-}c}$ [fF]	6	
τ_{RC} [ps]	2.15	1.59

5.3. Parameter Extractions for 3-Current Source Models

5.3.1. 2-Current Sources: Photogenerated Carrier Model

For extracting model parameters for diffusing and drifting photogenerated carrier values for I_1 (f) and I_2 (f), TCAD simulation based on imported optical generation rates from FDTD is performed.

For that, two virtual generation profiles are created, one containing the generation rates only in the region where the electric field is small (less than 4500 V/cm) as shown in Fig. 5-7(a) where carriers experience diffusion, and the other only in the region where the electric field is strong (larger than 4500 V/cm) where carriers experience drift as shown in Fig. 5-7(b). It was empirically found that simulated results do not change much as long as the diffusion/drift boundary field value is between 4000-V/cm and 5000-V/cm as shown in Fig. 5-8. Then, the photodetection frequency responses are simulated for each case and obtain separate photodetection frequency responses for diffusing and drifting photogenerated carriers as shown in Fig. 5-9(a) and (b) at –1 and –4 V, respectively.

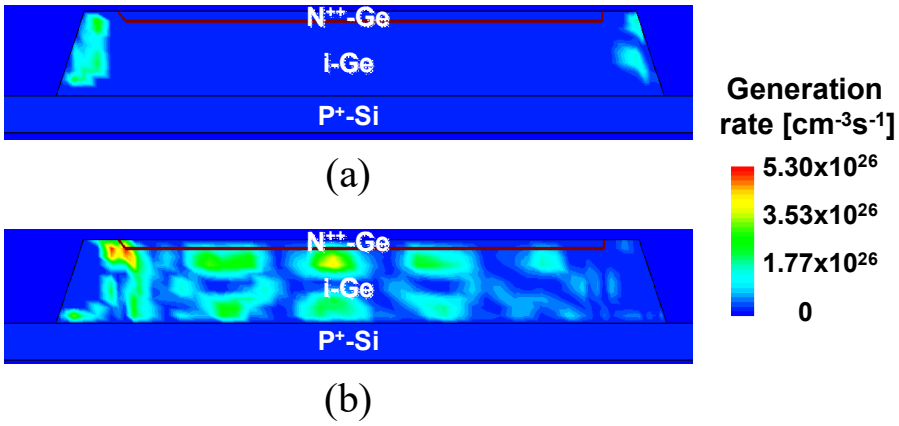

Fig. 5-7. Generation-rate profiles of (a) diffusion and (b) drift photogenerated carriers of Ge-VPD at –1 V.

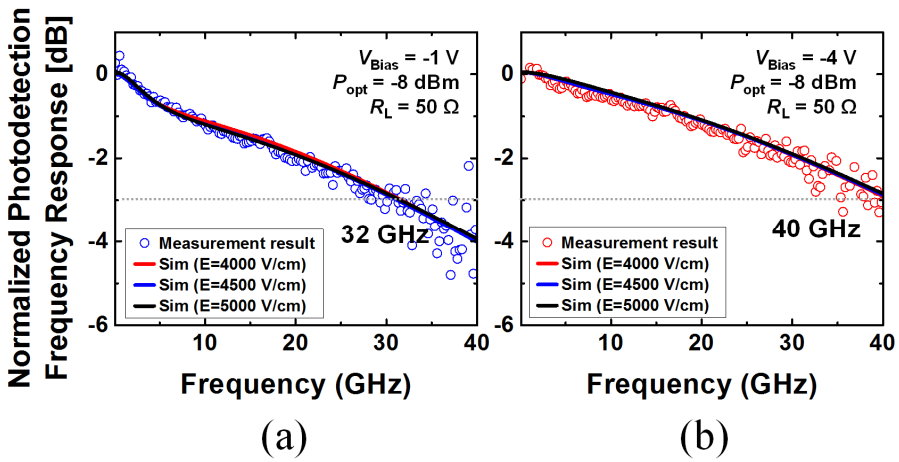

Fig. 5-8. Measured and simulated photodetection frequency response according to different boundary electric field intensity from 4000 to 5000 V/cm for Ge-APD at (a) –1 and (b) –4 V.

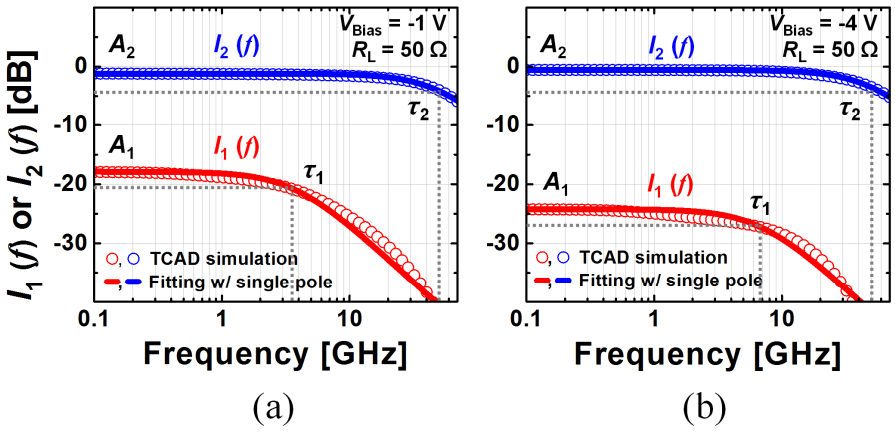

Fig. 5-9. Simulated frequency responses for two current source models at (c) –1 and (d) –4 V.

TABLE 5-3

EXTRACTED PARAMETERS FOR TWO CURRENT SOURCES FOR GE-VPD

	-1 V	**-4 V**
τ_1 [ps]	43.0	23.4
A_1 [%]	12.7	6.2
τ_2 [ps]	3.12	
A_2 [%]	87.3	93.8

From these, values for A_1, τ_1 for I_1 and A_2, τ_2 for I_2 are easily determined that produce the best matching between TCAD simulation and single-pole response as listed in Table 5-3. Both A_1 and τ_1 are smaller for larger reverse bias voltage as can be seen in Table 5-3 because with the larger reverse bias voltage, photogenerated carriers experience diffusion within a smaller portion of the device and, consequently, need to diffuse a smaller distance. τ_2 does not change with bias voltages because carriers drift with the saturation velocity, which does not change much with the bias voltages.

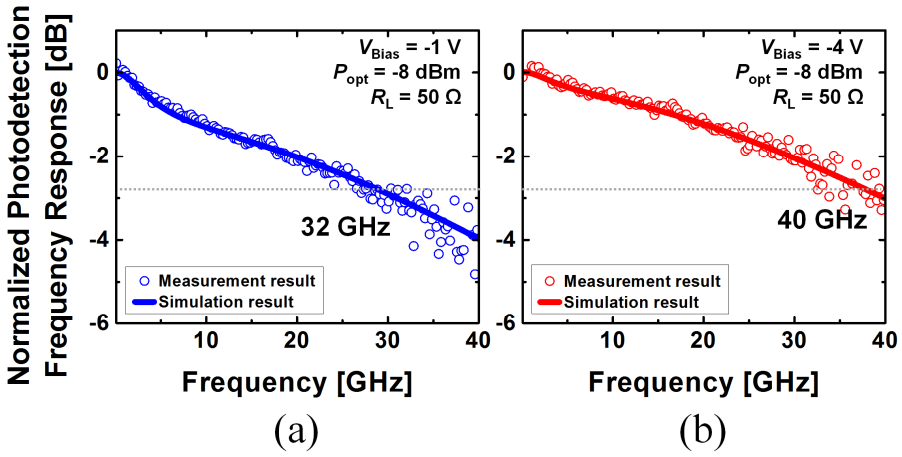

Fig. 5-10. Measured and simulated photodetection frequency responses from 100 MHZ to 40 GHz for Ge-VPD at (a) –1 and (b) –4 V.

Fig. 5-10(a) and (b) show the simulation results at –1 and –4 V for the complete Ge-PD equivalent circuit along with the measured results. Simulated results based on equivalent circuit model with extracted model parameters are well-matched to measured. From this, dedicated photogenerated carriers transport in absorption region can be extracted as bias voltages and they can be confirmed that considering as two parallel connected current sources having each single pole frequency limited by carrier diffusion and drift, respectively.

5.3.2. 1 Current Source: Noise Model

PD emitted noises are consisting of flicker, shot, and thermal noise. Although flicker noise has no general theoretical origin yet [33], valence band discontinuity in interface of Ge and Si materials, large defect densities, and contact processing are believed contributing flicker noise [38]. Flicker noise is dependent on frequencies so which is usually called as $1/f$ noise often. Flicker noise can be modeled by following equation:

$$\overline{I_{\text{n, flicker}}^2} = s_0 \frac{{I_{\text{DC}}}^a}{f^\gamma} \tag{5.1}$$

where $\overline{I_{\text{n, flicker}}^2}$ is the flicker noise spectral density, I_{DC} is the DC photocurrent, and s_0, a, γ are fitting parameters [33].

Shot noise is generated by the quantum nature of the photons in the optical input and that of the photogenerated carriers and this noise is modeled by following equation:

$$\overline{I_{\text{n, shot}}^2} = 2qI_{\text{DC}} \tag{5.2}$$

where $\overline{I_{\text{n, shot}}^2}$ is the shot noise spectral density and q is the electron charge [33]. For photomultiplier, photoconductor, and avalanche photodetector, since shot noise is also amplified due to their internal

gain, excess shot noise is used to represent that.

Thermal noise is generated by random thermal motion of the carriers and associated with the blackbody radiation. Only materials can absorb and dissipate energy can emit blackbody radiation, thermal noise is generated by resistive components [39]. Thermal noise is modeled by following equation:

$$\overline{I_{\text{n, thermer}}^2} = \frac{4kT}{R} \sim \frac{4kT}{R_{\text{j}}} \tag{5.3}$$

where $\overline{I_{\text{n, thermal}}^2}$ is the thermal noise spectral density, T is temperature in K, R is resistive component, and R_{j} is junction resistance of PD. In reverse biased p-i-n PD, resistive component is determined by series connected junction and series resistances. However, junction resistance in depletion region is much larger than series resistance and dominant thermal noise is determined by R_{j}.

Consequently, the total noise of PD is represented by following equation:

$$\overline{I_{\text{n}}^2} = s_0 \frac{{I_{\text{DC}}}^a}{f^{\gamma}} + 2qI_{\text{DC}} + \frac{4kT}{R_{\text{j}}}, \tag{5.4}$$

As can be seen in Eq. (5.4), noise spectral power density consists of the spectrally-dependent flicker noise dominant at low frequencies and the constant shot and thermal noises dominant at high frequencies [33].

Noise characteristics can be measured by using measurement setup in chapter 3.3 and Fig. 5-11(a) and (b) are measured and fitted noise spectral power densities by Eq. (5.4) from 50 to 850 MHZ at –1 and –4 V under –8-dBm optical power. The fitting parameters used in Eq. (5.4) are given in Table 5-4. Consequently, shot noise is mainly contributing total noise spectral power density of Ge-VPD. Small photocurrent, large junction resistance, and low temperature are preferred for low-noise photodetector applications.

TABLE 5-4
EXTRACTED PARAMETERS FOR NOISE CURRENT SOURCE MODEL OF GE-VPD UNDER −8-DBM OPTICAL POWER

	-1 V	**-4 V**
I_{DC} [μA]	71.6	105
s_0	0.55	
a	3.17	3.15
γ	1.1	1.1

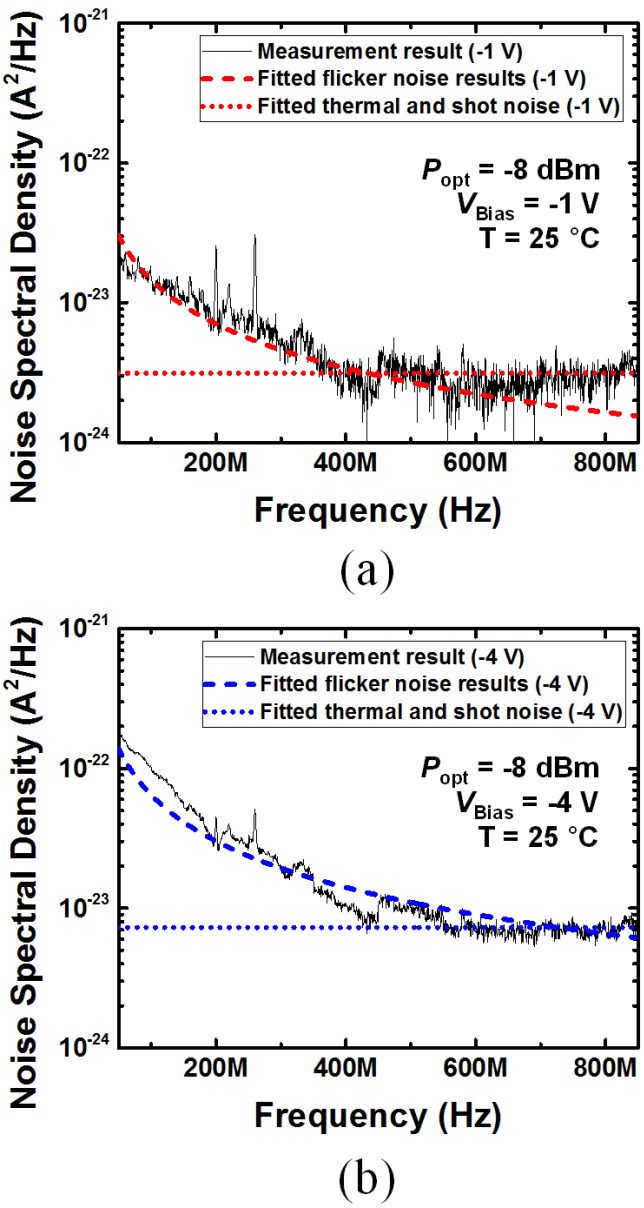

Fig. 5-11. Measured and fitted noise spectral densities of Ge-VPD at (a) –1 and (b) –4 V.

5.4. Frequency Response Analysis with Time Constants

As can be seen in modified equivalent circuit model of waveguide-type Ge-PD, three time constants contribute photodetection frequency responses. With the equivalent circuit model, it can be clarified how each of three time constants, τ_1, τ_2, and τ_{RC} (diffusion, drift, and *RC* time constants), influences the photodetection frequency response. These are available based on different circuit models in Fig. 5-12: (a) that includes all the factors (with τ_1, τ_2, and τ_{RC}), (b) which considers only the *RC* time constant (with τ_{RC}), and (c) that includes the photogenerated carrier transit time including diffusion and drift components (with τ_1 and τ_2).

Fig. 5-13 shows the simulated photodetection frequency responses based on circuit model in Fig. 5-12 at −1 V considering all three time constants (blue solid), τ_{RC} (black triangle), τ_1 and τ_2 (green dot), and only τ_2 and τ_{RC} (A_1 = 0, red circle). Z_{para} are not included for considering only the Ge-VPD core dynamics. It is interesting to note that the photodetection bandwidth is slightly higher with Z_{para} (32 GHz) than without (30 GHz). This is because the inductor in Z_{para} provides a small amount of frequency peaking. For A_1 = 0, the photodetection 3-dB bandwidth goes up to 38 GHz, indicating that the diffusion of

photogenerated carriers reduces the photodetection bandwidth by about 20 %. Furthermore, it can be clearly seen that carrier transport rather than τ_{RC} is the bandwidth limiting factor for Ge-VPD. This gives a clear design guideline for further bandwidth enhancement of waveguide-type Ge-PD on Si.

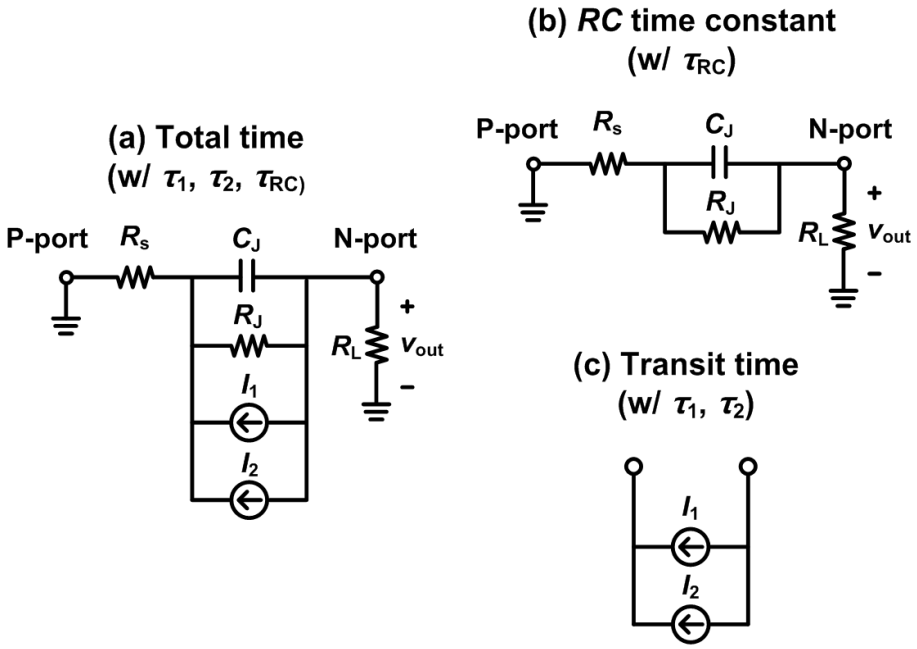

Fig. 5-12. Frequency response circuit models with three different combination of diffusion (τ_1), drift (τ_2), and *RC* time constant (τ_{RC}): (a) total time (τ_1, τ_2, and τ_{RC}), (b) *RC* time constant (τ_{RC}), and (c) photogenerated transit time (τ_1 and τ_2).

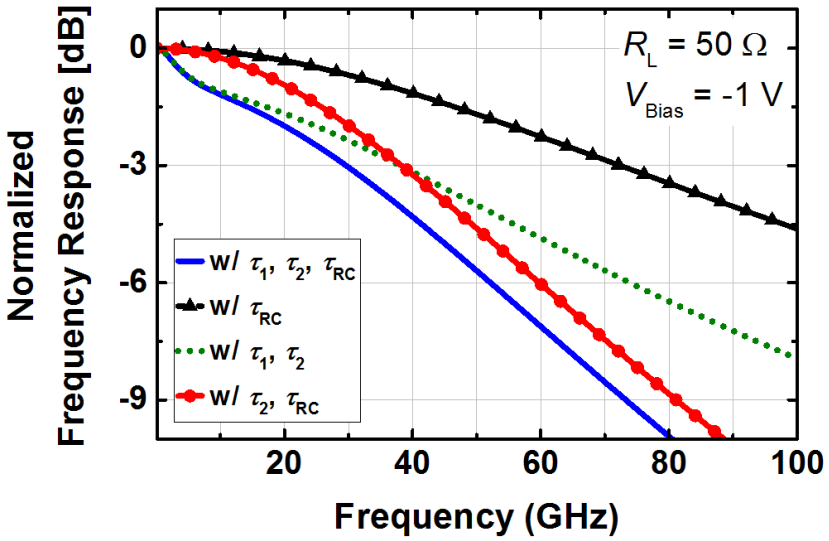

Fig. 5-13. Simulated photodetection frequency responses for Ge-VPD core at –1 V with different combination of diffusion (τ_1), drift (τ_2), and *RC* time constant (τ_{RC}).

5.5. Summary

In this chapter, modified equivalent circuit model of waveguide-type Ge-PD is introduced. The model is consisting of *RC* passive parameters for representing each p-i-n junction and parasitic components, and three current source models: two for modeling diffused and drifted photogenerated carriers in Ge absorption region, and one for emitted PD noise. It is also shown that how to model photogenerated carriers in waveguide-type Ge-PD to equivalent circuit model using TCAD simulation. For low-noise PD, noise characteristics are modeled based on noise related theories. From this equivalent circuit modeling, the performance of waveguide type Ge-PD can be easily analyzed and this is helpful to co-design with electronic circuits on circuit simulator environment for performance optimization.

6. Characteristics of Waveguide-Type Ge-PDs

In this chapter, the characteristics of several types of Ge-VPDs and Ge-LPDs are investigated. In chapter 6.1, two different structures of Ge-VPDs having different series resistance are designed using IME Si photonics foundry services to characterize series resistance effects to performance of Ge-VPDs. For that, current-voltage, optical power dependency in terms of dc photocurrent, and frequency responses are measured in this chapter. In addition, each equivalent circuit model based on measurement and TCAD simulation is provided for investigation in this chapter.

In chapter 6.2 and 6.3, the influences of Si waveguide width and n- and p-doped region areas on Ge-LPD performances are investigated. Ge-LPDs in this chapters are fabricated using IHP BiCMOS photonic fabrication process and measurement results are provided from IHP as collaboration. The equivalent circuit models of Ge-LPDs are also established and their characteristics are investigated based on model in this chapter.

6.1. The Effects of Series Resistance of Ge-VPDs

6.1.1. Device Description

Fig. 6-1(a) and (b) show the top-view and cross-section of the Ge-VPD investigated. Ge-VPDs are composed of highly n-doped Ge (N^{++}-Ge) layer, 0.5-μm thick intrinsic Ge (i-Ge) layer, and 0.22-μm thick p-doped Si (P^{+}-Si and P^{++}-Si) layer. The device is nominally 7-μm wide on the top, 8-μm wide at the bottom, and 11-μm long. Series resistance (R_s) of Ge-VPD is composed of the contact resistance and the resistance through p-doped Si layers below the photodetector intrinsic region. The fabrication process used for Ge-VPD has no silicide step, resulting in relatively large contact resistance of 5500 Ω-μm^2 between metal 1 to P^{++}-Si region [30]. In order to reduce contact resistance as much as possible, Ge-VPD has two parallel and relatively large (13.2 × 2.8 μm^2) contacts, which provides about 75 Ω contact resistance. To investigate the influence of R_s on Ge-VPD performance, two different types of devices are fabricated having different values for P^{+}-Si and P^{++}-Si region length as shown in Fig. 6-1(c). Type 1 Ge-VPD has smaller P^{++}-Si region length resulting in larger R_s. Type 2 has larger P^{++}-Si region length with P^{+}-Si region narrower than i-Ge region.

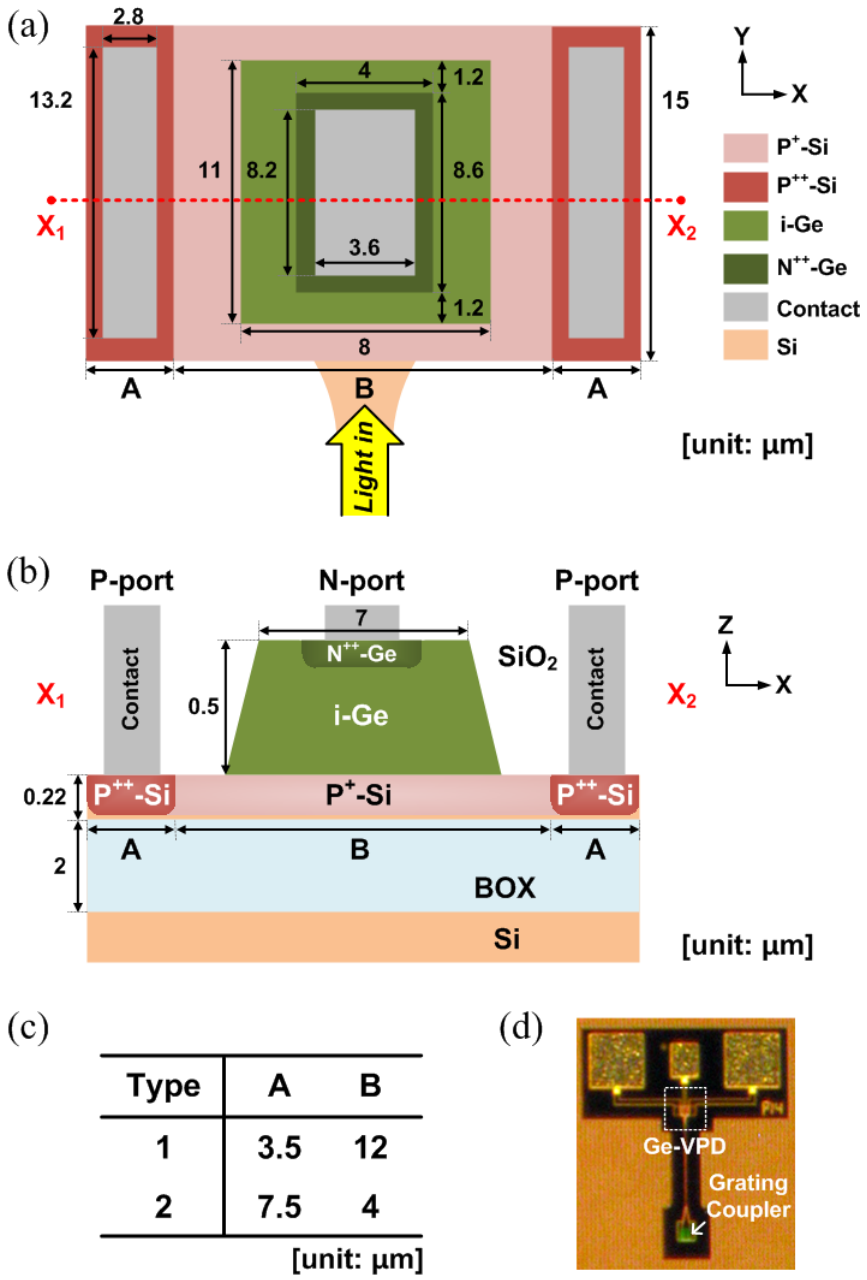

Fig. 6-1. (a) Top-view, (b) cross-section, (c) design parameters, and (d) microphotograph of fabricated Ge-VPD.

6.1.2. DC Characterizations

Current-voltage characteristics

Fig. 6-2(a) and (b) show measured dark current- and photocurrent-voltage characteristics for Type 1 and Type 2 Ge-VPDs for incident optical power of –5 dBm coupled into the Ge-VPD, respectively. Dark current increases exponentially with the applied electric field due to band bending in Ge-VPDs. In addition, two types of Ge-VPDs have almost the same current-voltage characteristics resulting in responsivities of about 0.45 A/W. This is because design modification to have different series resistance is performed on bottom p-doped Si region and the absorption is not much influenced by Si region transparent at 1550-nm wavelength light.

By using TCAD simulation with imported optical generation rates from FDTD, responsivities of Ge-VPDs can be also simulated. The responsivity is simulated as about 0.65 A/W under 100-μW optical power at –1 V. This result is larger than the measured one, which can be believed that calculated optical generation rates are not considered metal absorption from contact on N^{++}-Ge region and defects. If accurate metal information is provided, the simulated responsivity can be matched to the measured responsivity.

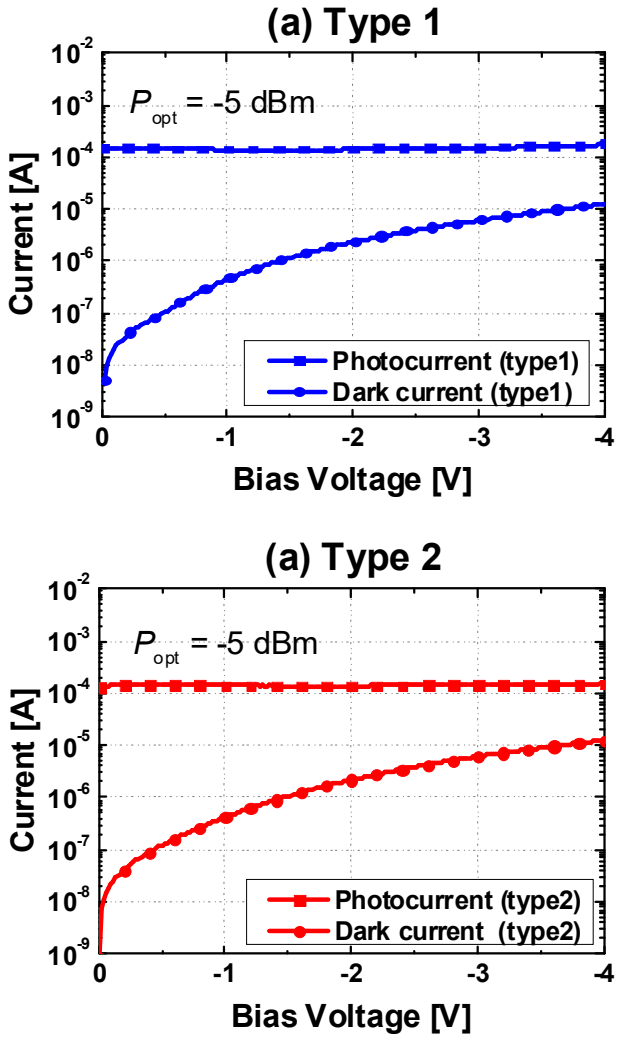

Fig. 6-2. Measured current-voltage characteristics of (a) Type 1 and (b) Type 2 Ge-VPDs as a function of bias voltage at −5-dBm incident optical power introduced to Ge-VPDs.

Photocurrent linearity characteristics

To characterize linearity of Ge-VPD, photocurrents for different incident optical powers at several different reverse bias voltages are measured as shown in Fig. 6-3.

In Fig. 6-3, the photocurrent of Ge-VPDs saturates at large input optical power due to space charge screening effect [31]. This effect is occurred when spatial distribution of photogenerated carriers transit the depletion region, which creates additional electric field that redistributes and collapse the electric field in the depletion region [31]. This also induces photogenerated carrier transit time increasing. Higher reverse bias voltages can mitigate space chare screening effect. Eventually, this can increase the ranges of linear photocurrent operations. However, large photocurrents cause Joule heating (I×V) and increase temperature in depletion region [31] due to thermal conductivity limitations of material with given geometry. This also leads to device failure due to thermally-activated runaway dark currents [31].

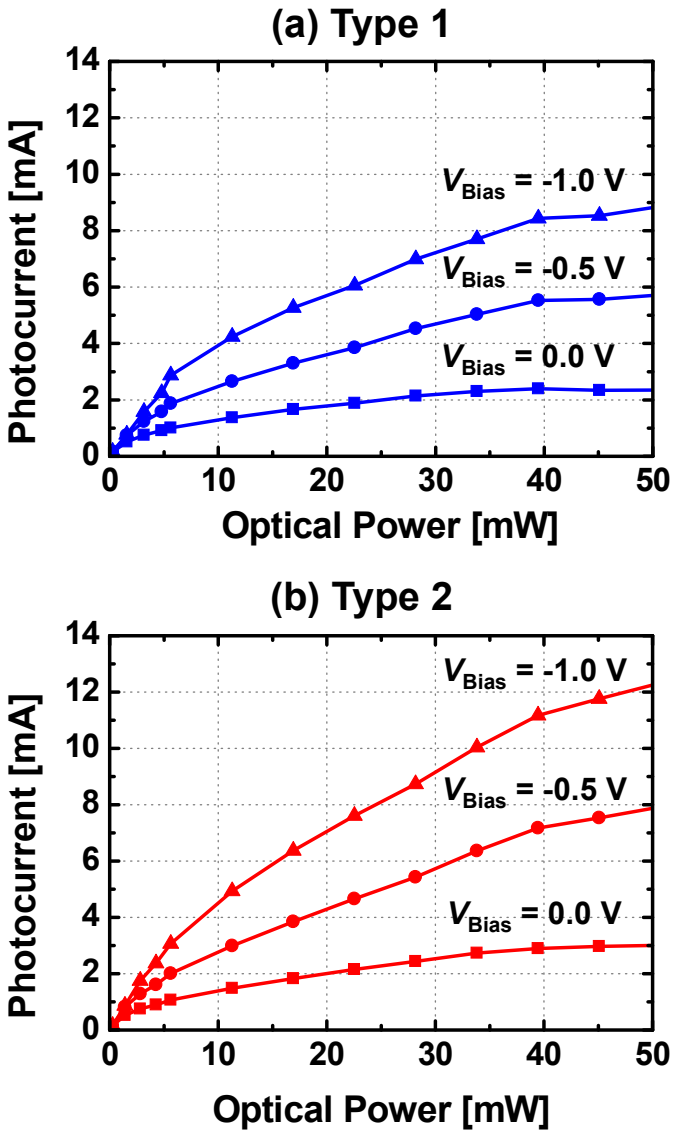

Fig. 6-3. Measured photocurrent as a function of input optical power introduced to Ge-VPDs at different bias voltages for (a) Type 1 and (b) Type 2 Ge-VPDs.

As can be seen in Fig. 6-3(b), photocurrents of Type 2 Ge-VPD saturate substantially less. This can be explained by investigation of current flows in photodetector. In Fig. 6-4, most photocurrent flow to R_s and R_L of equipment (50 Ω). Type 2 having smaller R_s should have smaller voltage drop in the p-doped Si region, which causes larger electric field in depletion region and mitigates more space charge screening effect than Type 1. Since saturation photocurrents are influenced by R_s and R_L, Ge-VPD having smaller R_s is preferred for PD application operating at large photocurrents.

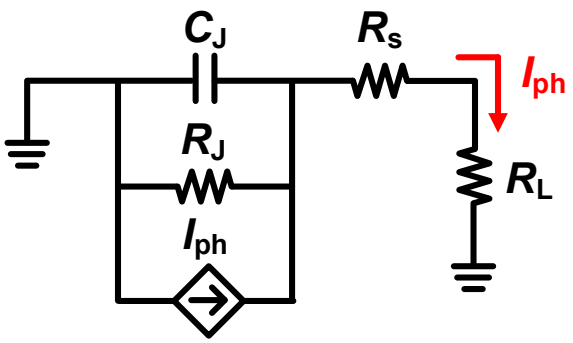

Fig. 6-4. Current flow in photodetector.

6.1.3. Frequency Response Characterizations

Frequency responses of Ge-VPDs having different series resistances are investigated based on accurate equivalent circuit models. The models are established by following the procedures introduced in Chapter 5. Electrical reflection coefficients as well as photodetection frequency responses are measured for modeling. From the measured results, frequency responses are characterized by extracted model parameters and their characteristics are explained by using model parameters.

Fig. 6-5 shows equivalent circuit model of Ge-VPDs. The model parameters are extracted by measured and simulated electrical reflection coefficients and photodetection frequency responses based on equivalent circuit model at different bias voltages of –1 and –4 V. Optical powers used in measurement are determined not to occur space charge screening effects. $C_{c\text{-}c}$ is used for representing capacitance between Ge-PD metal contacts can be obtained by comparing measured and simulated reflection coefficients of Ge-VPDs with de-embedding of C_{pad}, R_{int}, and L_{int}.

Fig. 6-6 shows resulting measured and simulated electrical reflection coefficients of Type 1 and 2 Ge-VPDs with Z_{para} on Smith

charts from 100 MHZ to 40 GHz at –1 and –4 V and extracted RC model parameters are listed in Table 6-1.

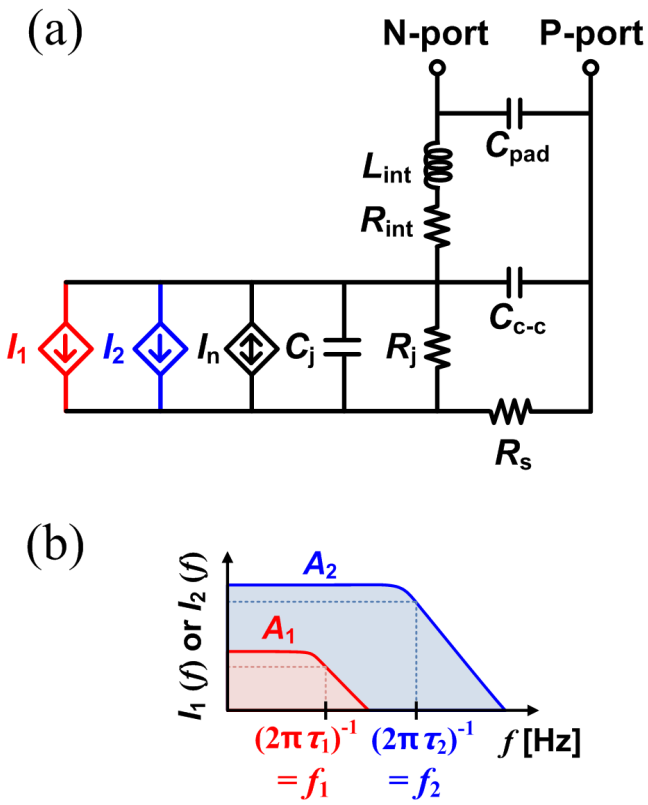

Fig. 6-5. (a) A modified equivalent circuit model of Ge-VPD with Z_{para} and (b) frequency responses of photogenerated current sources.

Electrical reflection coefficients on smith chart help to understand information of device impedance intuitively. The measurement results in Fig. 6-6 show that, at each reverse bias voltage, Type 2 has the smaller real part for the impedances than Type 1 but their imaginary parts are identical at a given frequency. This is because Type 2 has smaller R_s than Type 1 but C_j are the same for both. In addition, both Type 1 and 2 have the larger imaginary parts of their impedances for the higher reverse bias voltage, due to smaller C_j for the higher reverse bias voltage. These analyses are consistent with extracted model parameters. As can be seen in Table 6-1, Type 2 has smaller R_s than Type 1, but they have almost same C_j at each reverse bias voltages.

TABLE 6-1
EXTRACTED PARAMETERS FOR TYPE 1 AND 2 GE-VPDS

	Type 1		**Type 2**	
	−1 V	**−4 V**	**−1 V**	**−4 V**
R_s [Ω]	140		88	
C_j [fF]	15.9	11.6	15.9	11.6
R_j [kΩ]	20			
$C_{c\text{-}c}$ [fF]	6			
f_1 [GHz]	3.7	6.8	3.7	6.8
A_1 [%]	12.7	6.2	12.7	6.2
f_2 [GHz]	51	51	51	51
A_2 [%]	87.3	93.8	87.3	93.8

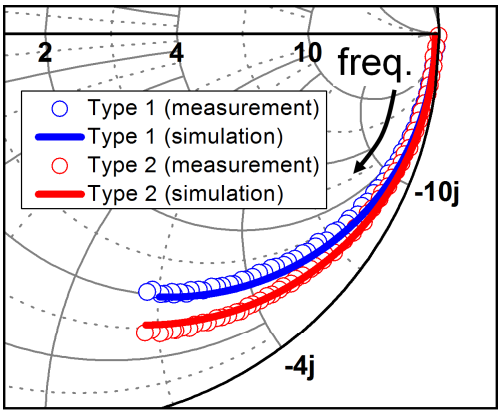

(a) -1 V

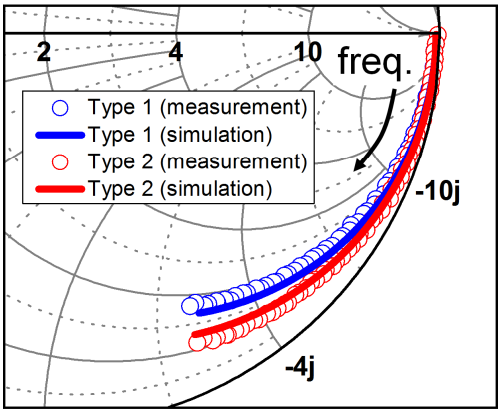

(b) -4 V

Fig. 6-6. Measured and simulated electrical reflection coefficients for Type 1 and 2 Ge-VPDs with Z_{para} from 100 MHZ to 40 GHz at (a) –1 and (b) –4 V.

To determine current source model parameters of diffused (f_1 and A_1 for I_1) and drifted (f_2 and A_2 for I_2) photogenerated carriers in Fig. 6-5(b), TCAD simulations are performed, and extracted model parameters for Type 1 and 2 at –1 and –4 V are listed in Table 6-1. Each current source model parameters are almost same, because Type 1 and 2 have almost same electric-field profiles in Ge absorption region despite of structure modification having different R_s values.

At higher reverse bias voltages for Ge-VPDs, diffused photogenerated-carrier transit time is reduced. This is because as shown in Fig. 6-7, undepleted region areas at –4 V is smaller than at –1 V due to fringing electric field extension. This is because highly N-doped Ge region cannot cover intrinsic Ge region entirely.

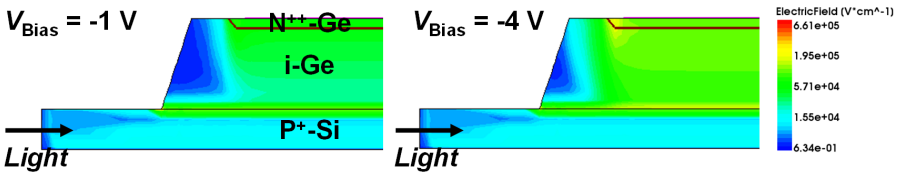

(a) (b)

Fig. 6-7. TCAD simulated electric-field profiles of Ge-VPDs at (a) –1 and (b) –4 V.

Fig. 6-8 shows normalized measured and simulated photodetection frequency responses of Ge-VPDs having different R_s. Simulation results also include 3 different kinds of results with different time constant considerations introduced in chapter 5.4: one that includes all the factors (with τ_1, τ_2, and τ_{RC}), another which considers only the *RC* time constant (with τ_{RC}), and third that includes the photogenerated carrier transit time including drift and diffusion components (with τ_1 and τ_2). From these simulations, bandwidth limiting factors and contribution of each time constant can be investigated. The extracted time constants are listed in Table 6-2. In Fig. 6-8, well-matched measured and simulated photodetection frequency responses considering all time constants represents model parameter validity. At higher reverse bias voltage, *RC* time constant is reduced due to smaller C_j and photogenerated carrier transit time is also decreased due to reduced diffused photogenerated carrier in absorption region.

These results imply that smaller R_s contributes photodetection bandwidth increases due to reduced *RC* time constant. In addition, limiting factors of photodetection frequency response are mainly determined by diffused photogenerated carrier transit time (τ_1) and its amount (A_1) than τ_{RC}.

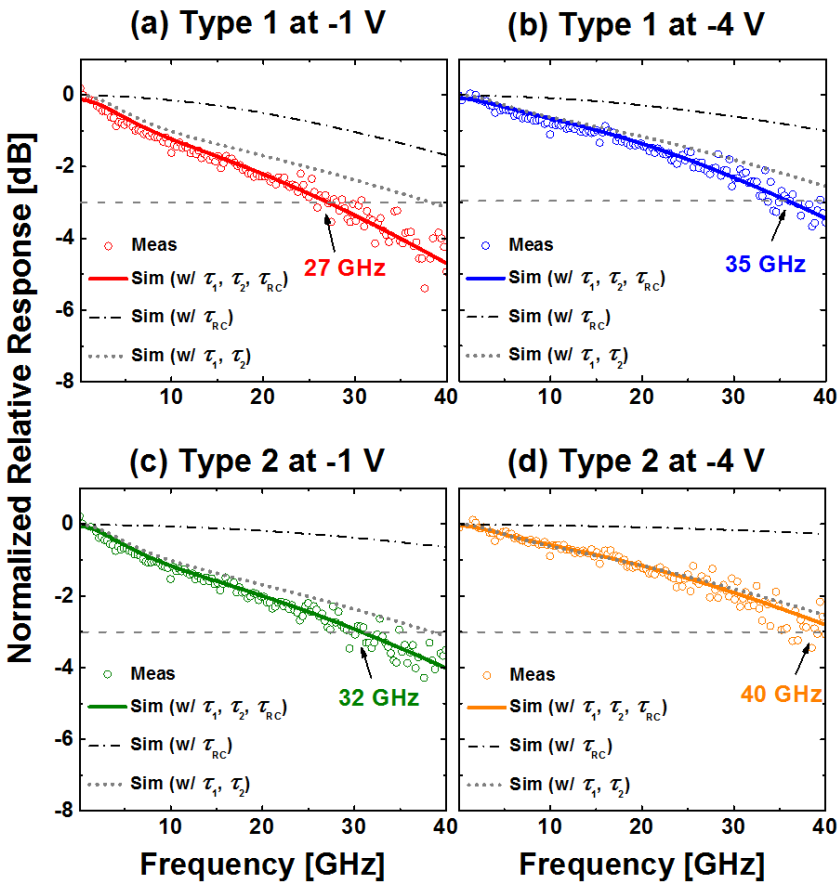

Fig. 6-8. Measured and simulated photodetection frequency responses with Z_{para} from 100 MHZ to 40 GHz for Type 1 Ge-VPD at (a) –1 and (b) –4 V and Type 2 Ge-VPD at (c) –1 and (d) –4 V under –8-dBm input optical power to Ge-VPDs.

TABLE 6-2
EXTRACTED TIME CONSTANTS FOR TYPE 1 AND 2 GE-VPD CORES

	Type 1		**Type 2**	
	−1 V	**−4 V**	**−1 V**	**−4 V**
τ_{RC} [ps]	3.3	2.5	2.3	1.7
$\tau_{transit}$ [ps]	4.2	3.5	4.2	3.5
τ_{total} [ps]	6.4	4.8	5.5	4.2

6.2. The Effects of Si Waveguide Width of Ge-LPDs

6.2.1. Device Description

The Ge-LPDs in this dissertation are fabricated by IHP BiCMOS photonic process and are composed of lateral highly n-doped, intrinsic and highly p-doped layer on 220-nm top Si layer [19]. The Ge absorption region is grown as much as the width of underlying Si waveguide width (W) and after that, self-aligned Phosphorus (P) and Boron (B) implantations are performed using self-aligned Si_3N_4 region. During doping implantation, P has long diffusion tail than B due to longer diffusion of P in Ge [38]. Then, Si cap layer is deposited on Ge region for cobalt silicidation ($CoSi_2$) process to reduce contact resistance than that from IME fabrication process [30]. Therefore, Ge-LPDs with silicidation process don't have to need large number of contacts that is done without silicidation, and as a result, Ge-LPDs can have small contact resistance.

To investigate the effects of Si waveguide width of Ge-LPDs to PD performance, four different structures of Ge-LPDs as shown in Fig. 6-9(a) are designed by increasing Si waveguide width (W) from 50 nm to 150 nm without changing any fabrication processes [40]. When Si

waveguide width is increased keeping the width of Si_3N_4, n- and p-doped region areas are also increased, whereas that of intrinsic region is constant. The detailed design parameters for each Ge-LPD are listed in Fig. 6-9(b).

(a)

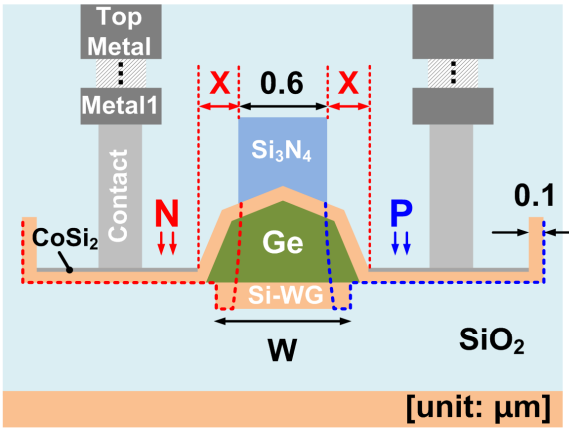

(b)

Type	1	2	3	4
W	0.9	1.0	1.1	1.2
X	0.15	0.20	0.25	0.30

[unit: μm]

Fig. 6-9. (a) Cross-section and (b) design parameters of fabricated four types of Ge-LPDs having 4 different W and X.

6.2.2. DC Characterizations

The origin of leakage current of reverse biased photodetector is generally diffusion current and generation of minority carriers in the depletion region governed by the Shockley-Read-Hall (SRH) process [41]. In addition, leakage current can be affected by defects and dislocations which can lead to dangling bond [43]. For Ge-LPD dc characterization, defects and dislocations occurred in Ge-LPD are investigated in this chapter.

Defects and Dislocations in Ge on Si

During fabrication process, several hetero-interface causes defects, dislocations, and band discontinuity. First, misfit and threading dislocations as shown Fig. 6-10 can be existed during Ge epitaxial growth on Si, which caused by lattice mismatch at Ge/Si interface. Second, dangling bonds occur at Ge/oxide and Ge/Si interfaces during passivation on Ge regions. Third, ion beam bombards the semiconductor substrate to implant dopants into the material, which leads to damage of the substrate. This is why post-implantation anneal is required to reduce defects [42]. In fact, extra non-doping ion implantation causes increased leakage current and photodetection

bandwidth at the same time by minority-carrier life time reduction, which is described in [38].

These defects and dislocations can be described in terms of electronic states in the Ge forbidden bandgap [43]. However, to figure out how much and where they are occurred in bandgap, samples need to be measured at each fabrication step such as Hall effect measurements as a function of temperature or deep-level transient spectroscopy (DLTS) measurements [44]. In other way, they can be referred by previously identified defects and dislocations occurred in similar process conditions such as temperature, time, atmosphere, duration, cooling rate, activation energy, etc. [44]. However, there are some limitations to verify with such methods using MPW services. Because MPW services mainly give users final complete fabricated

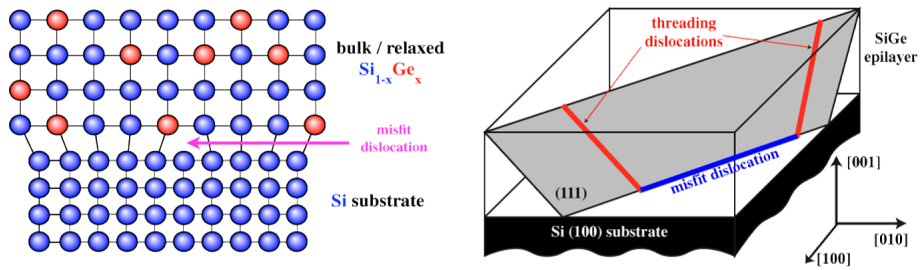

(a) (b)

Fig. 6-10. (a) Misfit dislocation in Si/Ge interface and (b) dislocations in Ge.

chips, but the detailed fabrication conditions are typically not disclosed to users.

Model for Defects and Dislocations

In this dissertation, due to these limitations and lack of unique and exhaustive model, a two-level distribution of defect model agreed by most published results is referred [43]. As shown in Fig. 6-11, the first level is acceptor-like level which is located above 0.07 eV from valence band and the other one is neutral deep level is above 0.2 eV from valence band.

Such states as discrete energy levels in the forbidden bandgap can be described using "traps" model in TCAD Sentaurus. However, since these energy level locations are influenced by various process conditions, trap level can be changed accordingly.

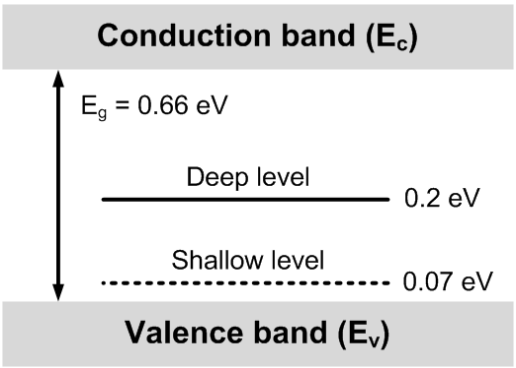

Fig. 6-11. The distribution of defect states in forbidden bandgap of Ge: deep and shallow states [42].

Also, the model in Fig. 6-11 is referred to specify trap levels, and their densities (or concentrations) are roughly determined until TCAD simulated current-voltage characteristics are matched to the measured results as shown in Fig. 6-12. This is one of the methodologies to determine trap concentration used in [43].

In fact, most defects and dislocations are located at the Si/Ge interfaces. However, their concentrations used in TCAD simulation are assumed to be distributed same for each location in Ge region due to lack of location information. If such a Hall effect measurement or a deep-level transient spectroscopy (DLTS) for identifying the electronic structure of defects are performed [42] or detailed process conditions are arranged, their location and concentration can be specified and determined with more improved accuracies.

Current-Voltage Characteristics

Fig. 6-12 shows measured and simulated dark current-voltage characteristics for Ge-LPDs having different Si-waveguide width. Since simulated results for Ge-LPDs in this chapter are very similar to each other types, only Type 1 simulated results are shown in Fig. 6-12 with traps (circle) and without traps (inverted triangle). The trap concentration of 1×10^{14} cm^{-3} and 1.5×10^{18} cm^{-3} for acceptor-like and

neutral deep levels are used for best matching, respectively.

Based on this result, responsivities of 4 types of Ge-LPDs can be also simulated. From that simulation, the influences of trap on PD responsivity can be investigated using TCAD with optical generation rates from FDTD.

From simulation without considering trap, about 0.7-A/W responsivities have shown, but with trap, they are reduced to about 0.4 A/W under 100-μW input optical power at –2 V. It is believed that this discrepancy is due to assumption of constant trap concentration at each location. However, most traps are distributed at Si/Ge interfaces in reality. Therefore, if additional information of trap distribution is arranged, it can be expected that the responsivity can be enhanced than before. In addition, responsivities at DC are not changed significantly according to the width of Si waveguide. This is because absorption coefficient is affected by length.

Consequently, dislocations and defects act as electrical traps, and generation and recombination centers in bandgap which affects increasing leakage current and decreasing photocurrent level [43]. Therefore, high quality of epitaxial growth and passivation are required to reduce leakage current and increase responsivity at the same time.

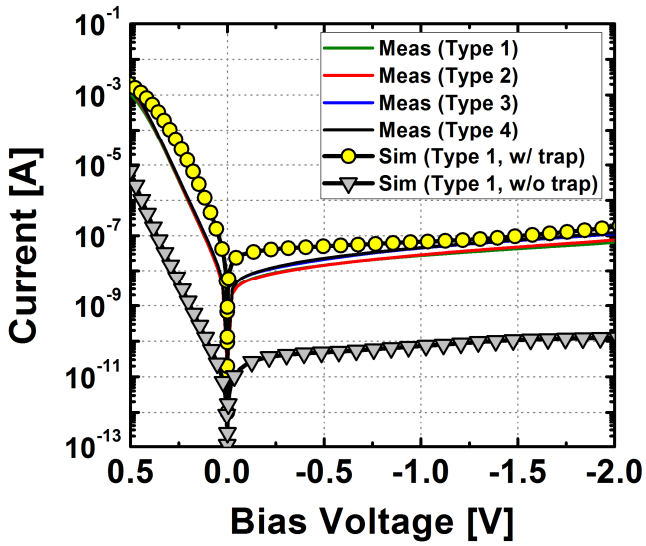

Fig. 6-12. Measured dark current-voltage characteristics for 4 types of Ge-LPDs having different Si waveguide width and simulated dark current results with and without trap.

6.2.3. Frequency Response Characterizations

Frequency response of Ge-LPDs having different Si waveguide width are investigated based on accurate equivalent circuit models.

Fig. 6-13(a) shows equivalent circuit model of Ge-LPDs without impedance for parasitic components (Z_{para}). The model parameters are extracted by measured and simulated electrical reflection coefficients and photodetection frequency responses based on equivalent circuit model at –2 V.

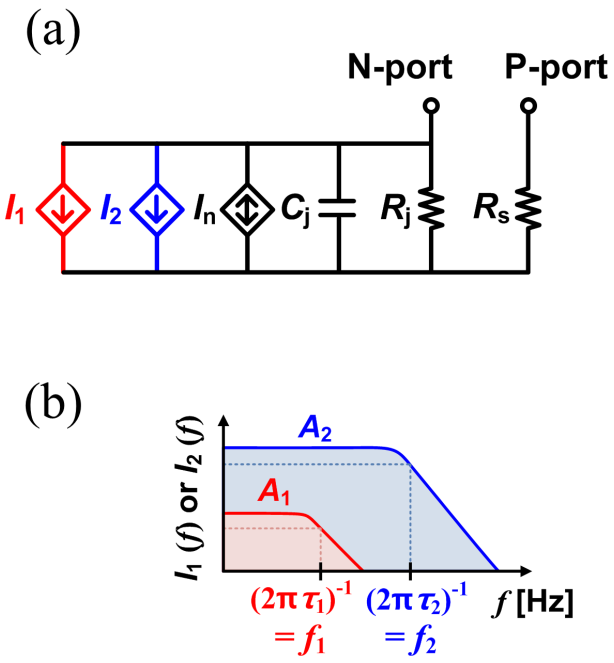

Fig. 6-13. (a) A modified equivalent circuit model of Ge-LPD core and (b) frequency responses of photogenerated current sources.

Electrical *S*-parameters of four types of Ge-LPDs having different Si waveguide width are measured as shown in Fig. 6-14 with a network analyzer from 100 MHZ to 67 GHz at –2 V. Resulting measured results are well-matched to simulated. The extracted model parameters for Ge-LPD core are listed in Table 6-3. As Si waveguide width increases, R_s decreases but C_j remains constant. This is because reduced distance between contact and the edge of intrinsic Ge region decreases R_s, and constant depletion region due to constant Si_3N_4 width contributes constant C_j.

TABLE 6-3
EXTRACTED PARAMETERS FOR 4 TYPES OF GE-LPDS HAVING DIFFERENT SI WAVEGUIDE WIDTH

	Type 1	**Type 2**	**Type 3**	**Type 4**
	−2 V			
R_s [Ω]	22	20	18	10
C_j [fF]	12			
R_j [kΩ]	100			
f_1[GHz]	19	12.5	12	10
A_1 [%]	10.0	10.8	13.8	16.3
f_2[GHz]	83	83	83	83
A_2 [%]	90.0	89.2	86.2	83.7

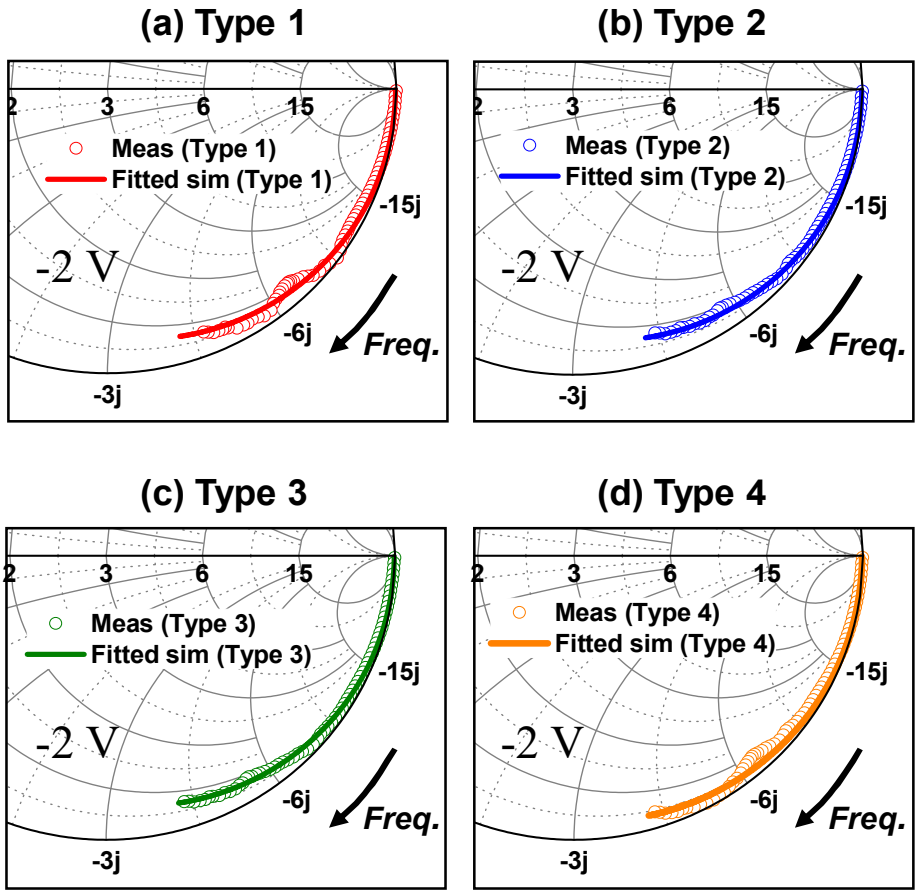

Fig. 6-14. Measured and simulated reflection coefficients for 4 types of Ge-LPD cores having different Si waveguide width from 100 MHZ to 67 GHz at –2 V.

To determine current source model parameters of diffused and drifted photogenerated carriers in Fig. 6-13(b), TCAD simulations are performed, and extracted model parameters for Ge-LPDs at –2 V are listed in Table 6-3. From this, it can be observed that as Si waveguide width is increased, diffused photogenerated carrier transit time (τ_1) and the amount (A_1) are also increased.

This analysis is reasonable when relationship between diffusion length and the width of each n- and p-doped charge neutral region are known. This can be verified by using below equations related to diffusion length:

$$L_{\mathrm{e/h}} = \sqrt{D_{\mathrm{e/h}} \cdot \tau_{\mathrm{e/h}}} \quad \text{and} \tag{6.1}$$

$$D_{\mathrm{e/h}} = \mu_{\mathrm{e/h}} (\frac{k\mathrm{T}}{q}) . \tag{6.2}$$

where $L_{\mathrm{e/h}}$ is diffusion length, $D_{\mathrm{e/h}}$ diffusion coefficient, $\tau_{\mathrm{e/h}}$ the life time, $\mu_{\mathrm{e/h}}$ mobility for electron and hole, k Boltzmann constant, T temperature in Kelvin, and q is electric charge.

Since $\mu_{\mathrm{e/h}}$ is influenced by doping concentrations and electric-field intensities, $\mu_{\mathrm{e/h}}$ is obtained by TCAD simulation for improved accuracies. $\tau_{\mathrm{e/h}}$ is chosen as the slowest case of about 100 ps which is from Type 4 in Table 6-3. From that, diffusion length of electron and hole is calculated by 250 and 230 nm, respectively. Since Type 4 has

about at least 300 nm charge neutral region, it can be verified that reduced doped regions causes reducing diffusion length, and as a result, Ge-LPD having smaller Si-waveguide width is preferred for enhanced photodetection bandwidth.

Fig. 6-15 shows normalized measured and simulated photodetection frequency responses of four types of Ge-LPDs. They also include 3 different simulation results considering time constants of τ_1, τ_2, and τ_{RC}. Type 1 having the smallest Si-waveguide width among them shows the largest photodetection bandwidth of about 70 GHz, whereas Type 4 shows the smallest of about 56 GHz. The extracted time constants are listed in Table 6-4 and from these, Ge-LPD having small Si-waveguide width contributes large photodetection bandwidth due to reducing diffused photogenerated carriers.

TABLE 6-4

EXTRACTED TIME CONSTANTS FOR 4 TYPES OF GE-LPD CORES HAVING DIFFERENT SI WAVEGUIDE WIDTH

	Type 1	**Type 2**	**Type 3**	**Type 4**
	−2 V			
τ_{RC} [ps]	0.87	0.84	0.82	0.72
$\tau_{transit}$ [ps]	2.26	2.36	2.55	2.72
τ_{total} [ps]	2.58	2.68	2.85	2.99

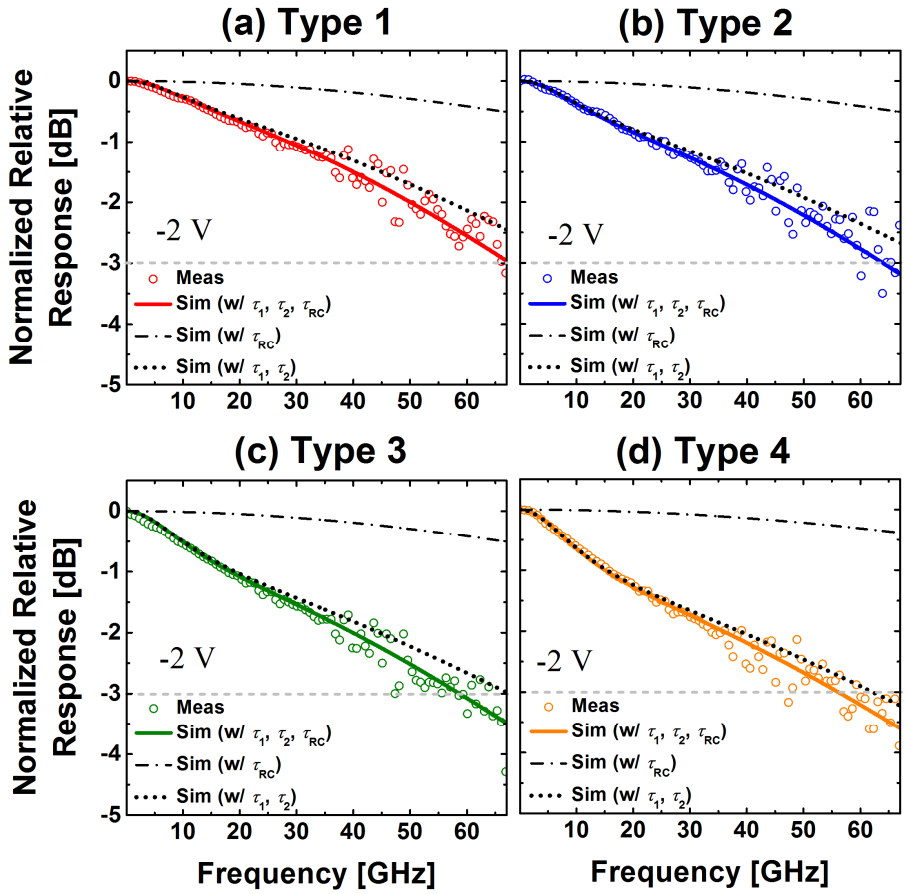

Fig. 6-15. Measured and simulated photodetection frequency responses from 100 MHZ to 67 GHz for four types of Ge-LPD cores having different Si waveguide width at –2 V.

6.3. The Effects of N- and P-Doped Region Areas of Ge-LPDs

6.3.1. Device Description

Fig. 6-16(a)–(d) show the top-view and cross-section of the 4 different structures of Ge-LPDs investigated [40]. All Ge-LPDs are composed of lateral highly n-doped, intrinsic and highly p-doped layer, on 0.22-μm top Si layer. They are fabricated using IHP BiCMOS photonic process [19] and realized by changing the width of Si waveguide layer underneath Ge epitaxy layer to have different portion of n- and p- doped region areas without changing any fabrication process [19]. As shown in Fig. 6-16, Type 1 has both narrow n- and p-doped regions, and Type 2 has both wide n- and p-doped regions, and Type 3 has narrow n- and wide p-doped regions, and on the contrary, Type 4 has wide n- and narrow p-doped regions. As compared with Type 3 and 4, Type 4 has wider doped region due to longer diffusion tail of P than B. The design parameters for each Ge-LPD are listed in Fig. 6-16(e).

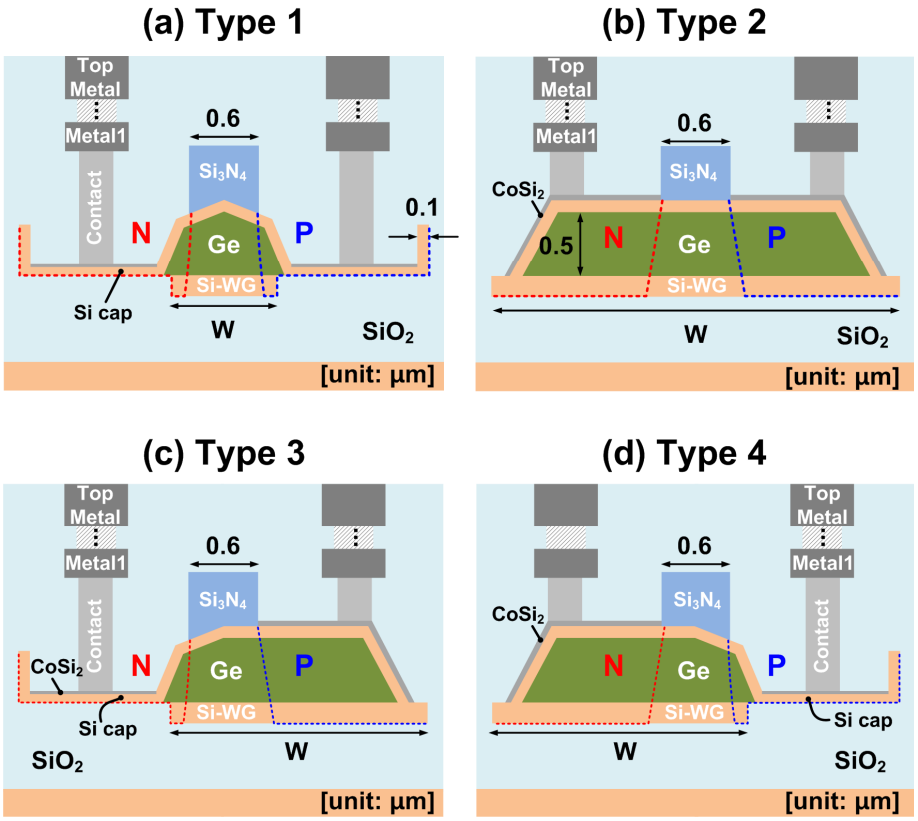

(e)

Type	1	2	3	4	
W	0.9	3.7	2.3	2.3	[unit: μm]

Fig. 6-16. (a)–(d) Cross-sections and (e) design parameters for 4 types of Ge-LPDs having different n- and p-doped region areas.

6.3.2. DC Characterizations

Fig. 6-17 shows dark current-forward bias voltage characteristics of four types of Ge-LPDs as shown in Fig. 6-16(a)–(d). The slope of this graph represents inverse of resistance for each Ge-LPD and as can be seen in Fig. 6-17, Type 1 having narrow n- and p-doped region has larger series resistance than any other type. This is because the distance between the edge of intrinsic Ge region and contact determines the value of R_s and therefore, Type 1 has the largest value of R_s.

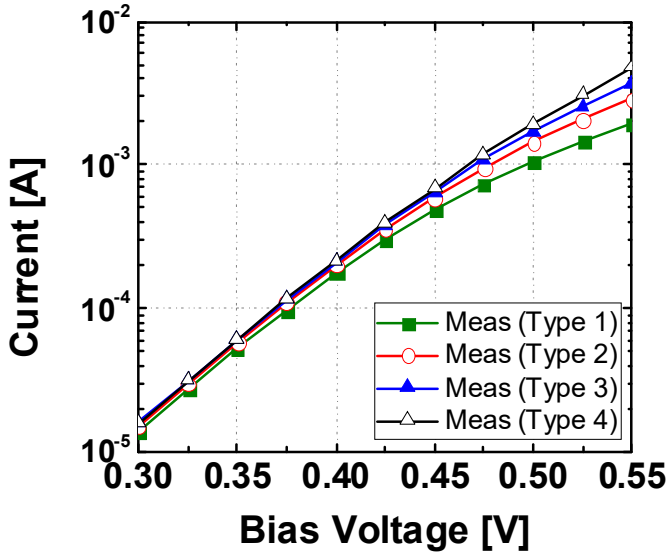

Fig. 6-17. Measured dark current-forward bias voltage characteristics for 4 types of Ge-LPDs having different n- and p-doped region areas.

Fig. 6-18 (a)–(d) shows measured and TCAD simulated dark current-bias voltage characteristics of 4 types of Ge-LPDs. As can be seen, simulation results without traps have huge gap from measured. Trap induced leakage currents at Si/Ge interfaces can be one possible reason. Trap concentrations used in simulation are listed in Table 6-5.

Based on that, responsivities of 4 types of Ge-LPDs are simulated and the influence of trap on Ge-PD responsivity can be investigated using TCAD with imported optical generation rates from FDTD. Without trap, they have about 0.7-A/W responsivities, but with trap, responsivities are reduced to 0.4 A/W under 100-μW input optical power at –2 V. It is believed that this discrepancy is due to assuming constant trap concentration at each location. These simulation results also show similar responsivity characteristics, however, simulations are performed on ignoring metal absorption effects from contact region. It can be believed that the responsivities of Type 2, 3, and 4 will be smaller than Type 1, because wide doped regions in these type are very close to contact region which causes metal absorption effects much more.

TABLE 6-5

TRAP CONCENTRATIONS USED IN SENTAURUS DEVICE SIMULATION FOR 4 TYPES OF GE-LPDS HAVING DIFFERENT N- AND P-DOPED REGION AREAS

	Type 1	**Type 2**	**Type 3**	**Type 4**
Neutral [cm^{-3}]	1×10^{14}	1×10^{14}	1×10^{14}	1×10^{14}
Acceptor-like [cm^{-3}]	1.5×10^{18}	2.9×10^{18}	2.5×10^{18}	2.5×10^{18}

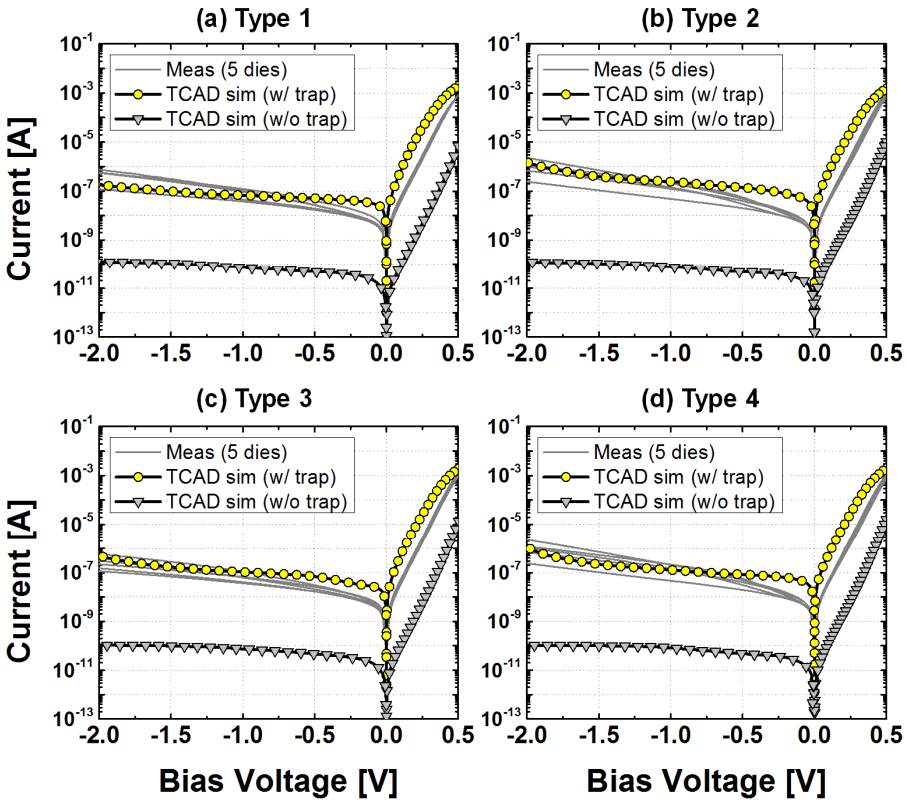

Fig. 6-18. Measured dark current-voltage characteristics for 4 types of Ge-LPDs having different n- and p-doped region areas.

6.3.3. Frequency Response Characterizations

Frequency response of Ge-LPDs having different n- and p-doped region areas are investigated based on accurate equivalent circuit models. The model is same as in Fig. 6-13 and extracted model parameters for Ge-LPD core are listed in Table 6-6 and resulting simulated results are well-matched to measured one as shown in Fig. 6-19. As can be seen in Table 6-6, R_s of Type 1 is about 22 Ω and this is larger than any other type and this coincides with R_s analysis based on dark current-forward bias voltage characteristics. Since the width of Si_3N_4 for all types of Ge-LPDs is same, they have almost same depletion width resulting in almost same C_j.

TABLE 6-6
EXTRACTED PARAMETERS FOR 4 TYPES OF GE-LPD CORES HAVING DIFFERENT N- AND P-DOPED REGION AREAS

	Type 1	**Type 2**	**Type 3**	**Type 4**
	−2 V			
R_s [Ω]	22	9	8	1
C_j [fF]	10			
R_j [kΩ]	100			
f_1[GHz]	19	12	15	10
A_1 [%]	10.0	29.0	23.5	57.0
f_2[GHz]	83	83	83	83
A_2 [%]	90.0	71.0	76.5	43.0

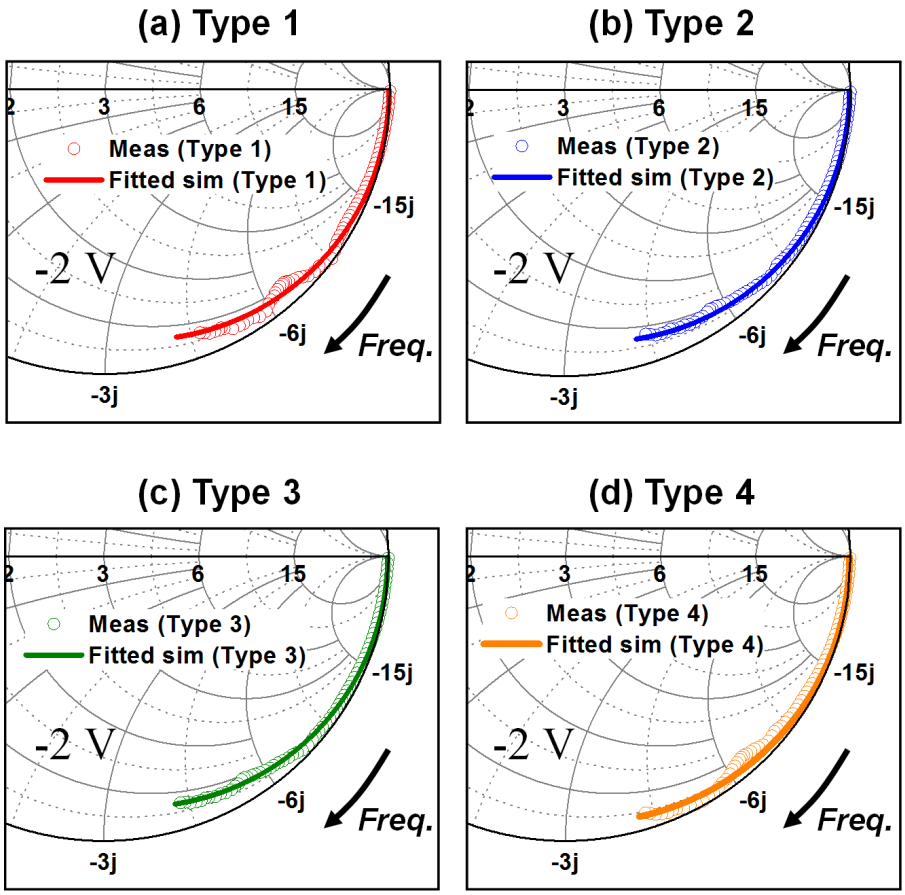

Fig. 6-19. Measured and simulated electrical reflection coefficients for four types of Ge-LPD cores having different n- and p-doped region areas from 100 MHZ to 40 GHz at –2 V.

To determine current source model parameters of diffused and drifted photogenerated carriers in Fig. 6-13(b), TCAD simulations are performed and extracted model parameters for Ge-LPDs at –2 V are listed in Table 6-6.

Fig. 6-20 shows normalized measured and simulated photodetection frequency responses of four types of Ge-LPDs. They also include 3 different simulation results considering time constants of τ_1, τ_2, and τ_{RC}. As can be seen in Fig. 6-20, Type 1 has the largest photodetection bandwidth and this is because Type 1 having smaller n- and p-doped region areas causes smaller diffusion length than any other type. From Type 3 and 4, the influence of diffused photogenerated electron and hole carriers in p- and n-doped region can be investigated, respectively. Since Type 4 has wider doped region due to longer diffusion tail of Phosphorus as shown in Fig. 6-21, more amounts of slow photogenerated hole carriers limit photodetection bandwidth. On the contrary, for Type 3, photogenerated electrons in p-doped region limit photodetection bandwidth. However, due to shorter diffusion tail of Boron, smaller amounts of photogenerated electrons contributes photodetection bandwidth which can have larger bandwidth than Type 4.

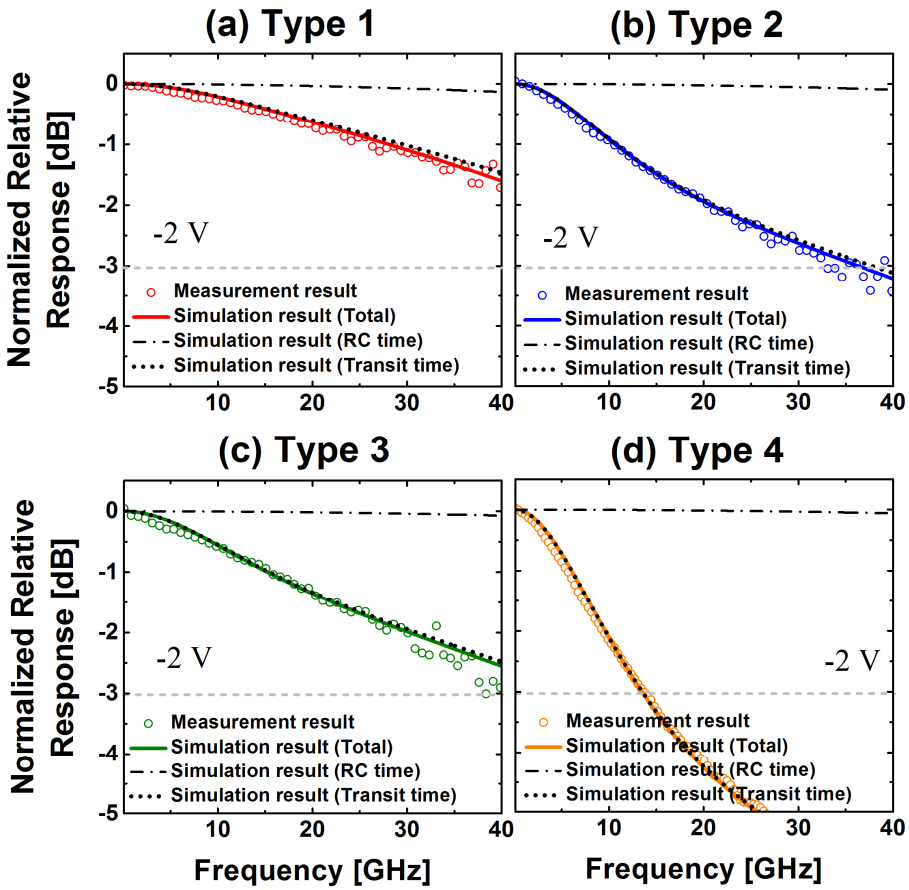

Fig. 6-20. Measured and simulated photodetection frequency responses for four types of Ge-LPD cores having different n- and p-doped region areas from 100 MHZ to 40 GHz at –2 V.

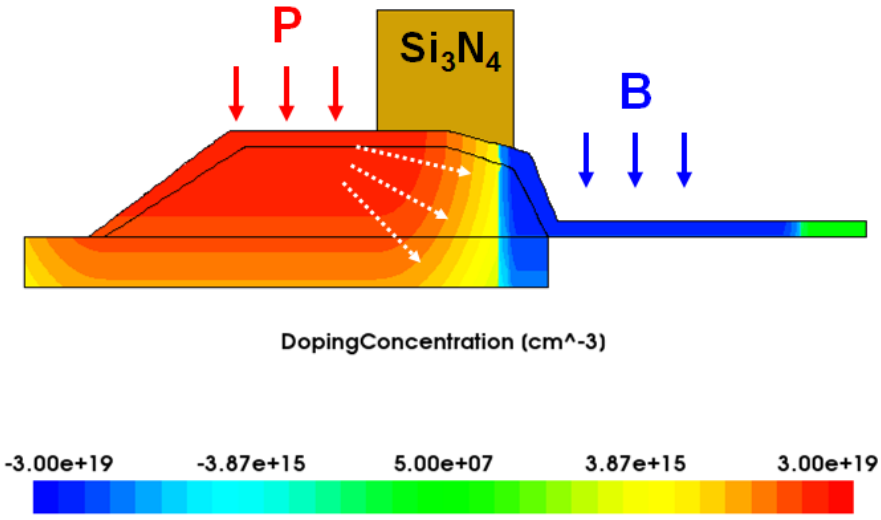

Fig. 6-21. TCAD simulated doping profiles of Type 4 Ge-LPD having wide n-doped region.

TABLE 6-7

EXTRACTED TIME CONSTANTS FOR 4 TYPES OF GE-LPD CORES HAVING DIFFERENT N- AND P-DOPED REGION AREAS

	Type 1	**Type 2**	**Type 3**	**Type 4**
	−2 V			
τ_{RC}	0.72	0.59	0.52	0.47
$\tau_{transit}$	2.26	4.22	3.19	11.75
τ_{total}	2.5	4.39	3.32	11.79

6.4. Summary

In this chapter, the characteristics of several types of Ge-VPDs and Ge-LPDs fabricated by IME and IHP fabrication process are investigated, respectively. Two types of Ge-VPDs having different series resistance, four types of Ge-LPDs having different Si waveguide width, and for types of Ge-LPDs having different n- and p-doped region areas are characterized as current-voltage, photocurrent linearity, electrical *S*-parameters, and photodetection frequency responses.

These are characterized and investigated by modified equivalent circuit model and several TCAD simulations. From these investigations, waveguide-type Ge-PD having small series resistance is suitable for large photocurrent operation and Ge-LPD having smaller Si-waveguide width and smaller doping regions causes larger photodetection bandwidth due to having smaller diffusion length. These analysis and investigation are helpful to apply waveguide-type Ge-PD to various kinds of Si-based applications.

7. Conclusion

In this dissertation, several waveguide-type Ge-PDs on Si are investigated and their characterization, simulation and modeling works are performed specifically. Two different junction types of Ge-PDs having vertical and lateral p-i-n junctions are realized by IME and IHP Si photonics fabrication processes, respectively. Ge-PD measurements are done with DC, AC, and noise measurement setup to characterize current-voltage, linearity, electrical *S*-parameter, photodetection frequency response, and noise. The modified equivalent circuit model for several types of waveguide-type Ge-PDs on Si is also introduced. This model includes *RC* passive circuit components, two current sources for photogenerated carriers experiencing diffusion and drift, and one noise current source. Based on this equivalent circuit model and TCAD simulation, the influence of series resistance, Si-waveguide width, and n- and p-doped region areas on PD performances are investigated and identified in this dissertation.

These analyses and model should be very useful for investigating waveguide-type Ge-PDs and designing optimal integrated with electronic circuits for a variety of Si-based applications.

Bibliography

[1] https://engineering.ucsb.edu/insights2006/pdf/presentations/insights2006_mario_paniccia.pdf M. Panicca, "First electrically pumped hybrid silicon laser.ppt" Oct. 2016.

[2] G. P. Agrawal, "Fiber-optic communication systems," vol. 222. John Wiley & Sons, 2012.

[3] D. Bryant, "Connectivity's demands and Intel silicon photonics," Intel Corporation, 2016.

[4] Q. Tan, "The on-going revolution of and Intel silicon photonics," Intel Corporation, 2014.

[5] D. P. Vidyarthi, *Techonologies and Protocols for the Future of Internet Design: Reinventing the Web*, PA: IGI Global, 2012.

[6] M. Streshinsky *et al*., "The road to affordable, large-scale," *Optics & Photonics News*, Sep. 2013.

[7] J. F. Buckwalter *et al*., "A monolithic 25-Gb/s transceiver with photonic ring modulators and Ge detectors in a 130-nm CMOS SOI process," *IEEE J. Solid-State Circuits*, vol. 47, no. 6, pp. 1309–1322, June 2012.

[8] Estevez, M.C., Alvarez, M. and Lechuga, L.M. (2012), Integrated optical devices for lab-on-a-chip biosensing applications. Laser & Photon. Rev., 6: 463–487. doi:10.1002/lpor.201100025

[9] R. Llorente and M. Beltrán (2010). Radio-over-Fibre Techniques and Performance, Frontiers in Guided Wave Optics and Optoelectronics, Bishnu Pal (Ed.), InTech, DOI: 10.5772/39559. Available from: http://www.intechopen.com/books/frontiers-in-

guided-wave-optics-and-optoelectronics/radio-over-fibre-techniques-and-performance

[10] G. Eneman *et al.*, "Defects, junction leakage and electrical performance of Ge pFET devices," *ECS Trans.*, vol. 19, no. 1, pp. 195–205, 2009.

[11] G. Dehlinger *et al.*, "High-speed germanium-on-SOI lateral PIN photodiodes," *IEEE Photon. Technol. Lett.*, vol. 16, no. 11, pp. 2547–2549, Nov. 2004.

[12] A. Novack *et al.*, "Germanium photodetector with 60 GHz bandwidth using inductive gain peaking," *Opt. Exp.*, vol. 21, no. 23, pp. 28387−28393, Nov. 2013.

[13] S. Assefa *et al.*, "CMOS-integrated high-speed MSM germanium waveguide photodetector," *Opt. Exp.*, vol. 18, no. 5, pp. 4986–4999, Feb. 2010.

[14] S. Klinger *et al.*, "Ge-on-Si p-i-n photodiodes with a 3-dB bandwidth of 49 GHz," *IEEE Photon. Technol. Lett.*, vol. 21, no. 13, pp. 920–922, July 2009.

[15] L. Virot *et al.*, "High-performance waveguide-integrated germanium PIN photodiodes for optical communication applications [Invited]," *Photon. Res.* vol. 1, no. 3, pp. 140–147, Oct. 2013.

[16] N. Duan *et al.*, "High speed waveguide-integrated Ge/Si avalanche photodetector," *in Proc. OFC*, 2013, pp. 1–3.

[17] S. Assefa *et al.*, "CMOS-integrated high-speed MSM germanium waveguide photodetector," *Opt. Exp.*, vol. 18, no. 5, pp. 4986–4999, Feb. 2010.

[18] H. T. Chen *et al.*, "High-responsivity low-voltage 28-Gb/s Ge p-i-n photodetector with silicon contacts," J. Lightw. Technol., vol. 33, no.4, pp. 820−824, Feb. 2015.

[19] S. Lischke *et al*., "High bandwidth, high responsivity waveguide-coupled germanium p-i-n photodiode," *Opt. Exp*., vol. 23, no. 21, pp. 27213–27220, Oct. 2015.

[20] R.R.A. Binetti *et al*., "InP/InGaAs photodetector on SOI photonic circuitry," *IEEE Photonics Journal*, vol. 2, no. 3, pp. 1–7, June 2010.

[21] A. Beling *et al*., "High-power high-speed waveguide photodiodes and photodiode arrays heterogeneously integrated on silicon-on-insulator," *in Proc. OFC*, 2013, pp. 1–3.

[22] M. –J. Lee *et al*., "Optical-power dependence of gain, noise, and bandwidth characteristics for 850-nm CMOS silicon avalanche photodetectors," *IEEE J. Sel. Topics Quantum Electron.,* vol. 20, no. 6, p. 3802807, Nov./Dec. 2014.

[23] M. Peils *et al*., "Nonlinear modeling of waveguide photodetectors," *Opt. Exp*., vol. 21, no. 13, pp. 15634–15644, June 2013.

[24] J.-S. Youn *et al*., "SNR characteristics of 850-nm OEIC receiver with a silicon avalanche photodetector," *Opt. Exp*., vol. 22, no. 1, pp. 900–907, Jan. 2014.

[25] Z. Abdallah *et al*., "Nonlinear equivalent-circuit modeling of a fast photodiode," *IEEE Photon. Technol. Lett.*, vol. 26, no. 18, pp. 1840–1842, Sep. 2014.

[26] D. Dai *et al.,* "Equivalent circuit model of Ge/Si avalanche photodiode," *in Proc. Int. Conf. on Group IV Photonics*, 2009.

[27] A. Novack *et al.,* "Germanium photodetector with 60 GHz bandwidth using inductive gain peaking," *Opt. Exp*., vol. 21, no. 23, pp. 28387–28393, Nov. 2013.

[28] M. Gould *et al*., "Bandwidth enhancement of waveguide-coupled photodetectors with inductive gain peaking," *Opt. Exp.*, vol. 20, no. 7, pp. 7101−7111, Mar. 2012.

[29] T.-Y. Liow *et al.*, "Silicon optical interconnect device technologies for 40 Gb/s and beyond," *IEEE J. Sel. Topics Quantum Electron.*, vol. 19, no. 2, p. 8200312, Mar./Apr. 2013.

[30] Y. Zhang *et al.*, "Silicon multi-project wafer platforms for optoelectronic system integration," *in Proc. Int. Conf. on Group IV Photonics*, 2012, pp. 63–65.

[31] D. A. Tulcbinsky *et al.*, "High-power photodetectors," *IEEE LEOS Newsletter*, pp. 16–17. Apr. 2005

[32] S. M. Sze *et al.*, *Physics of Semiconductor Devices*, 3rd ed. NY: Wiley, 2007.

[33] N. C. Harris *et al.*, "Noise characterization of a waveguide-coupled MSM photodetector exceeding unity quantum efficiency," *J. Lightw. Technol.*, vol. 31, no. 1, pp. 23−27, Jan. 2013.

[34] K. S. Yee *et al.*, "The finite-difference time-domain (FDTD) and the finite-volume time-domain (FVTD) methods in solving Maxwell's equations," *IEEE Trans. Antennas Propa*g., vol. 45, no. 3, pp. 354−363, Mar. 1997.

[35] J.-M. Lee *et al.*, "An equivalent circuit model for a Ge waveguide photodetector on Si," IEEE Photon. Technol. Lett., vol. 28, no. 21, pp. 2435–2438, Nov. 2016.

[36] Lumerical FDTD Solutions [Online]. Available: htttp://www.lumerical.com

[37] *Synopsys TCAD Sentaurus Manuals*, Mountain View, CA, USA, 2009. [Online]. Available: http://www.synopsys.com

[38] S. Lischke *et al.*, "High-speed, waveguide Ge PIN photodiodes for a photonic BiCMOS process," *in proc. BCTM*, 2014, pp. 29-32.

[39] Jia-Ming Liu, Principles of Photonics, NY: Cambridge, 2016.

[40] S. Lischke *et al*., "Design Effects on the Performance of High-Speed Ge Photo Detectors," *in Proc. Int. Conf. on Group IV Photonics*, 2016.

[41] H. Chen *et al*., "Dark current analysis in high-speed germanium p-i-n waveguide photodetectors," *J. Appl. Phys.* vol. 119, no. 21, p.213105, June 2016.

[42] K. Wada and L. C. Kimerling, "Defects in Germanium," in *Photonics and Electronics with Germanium*, 1st ed. Weinheim, Germany: Wiley, 2015, ch. 1.

[43] V. Sorianello *et al*., "Near-infrared photodetectors in evaporated Ge: characterization and TCAD simulation," *IEEE Trans. Electron Devices*, vol. 60, no. 6, pp.1995–2000, June 2013.

[44] C. Claeys and E. Simoen, *Extended Defects in Germanium: Fundamental and Technological Aspects.* Berlin, Germany: Springer-Verlag, 2009.

Abstract (In Korean)

Si 위에서 구현된 도파관 타입의 Ge 광 검출기의 특성, 시뮬레이션 및 모델링

Si photonics 기술은 성숙한 Si 공정 기술에 기반하여 고밀도의 광 집적 회로를 구현할 수 있어 최근 연구 관심도가 증가하고 있으며, 이를 활용한다면 고성능의 전자 시스템에서 그 동안 문제가 되었던 Interconnect 병목 현상을 해결 할 수 있는 하나의 솔루션이 될 것으로 많은 기대를 받고 있다. 이러한 우수한 Si 공정 기술을 활용한다면 1.5-μm 대역의 빛을 흡수할 수 있는 고성능의 Ge 광 검출기를 구현할 수 있다. 최근 다양한 타입의 Si 기판 위에서 구현된 고속 도파관 타입의 Ge 광 검출기뿐만 아니라 이러한 광 검출기가 집적화된 광 수신기 연구가 활발히 진행되고 있다.

본 학위 논문에서는 Si-on-Insulator 기판 위에서 구현된 도파관 타입의 Ge 광 검출기의 특성, 시뮬레이션, 모델링에 대해 집중적으로 연구하였다. 본 논문에서 다루어지는 Ge-PD는 수직과 수평 방향의 p-i-n 접합을 가지고 있으며 각각 IME와 IHP 공정을 활용하여 구현되었다. 서로 다른 직렬 저항을 가지고 있는 Ge-VPD, 서로 다른 Si 도파관 너비를 가지고 있는 Ge-LPD, 그리고 서로 다른 n과 p타입

도핑 영역 면적을 가지고 있는 Ge-LPD들에 대해서 연구 되었고, DC, AC, noise 측정을 통해 그들의 특성을 자세히 파악하였다. 뿐만 아니라 자세한 PD 특성 이해를 돕기 위해 TCAD Sentaurus와 Lumerical FDTD 시뮬레이션 툴을 통합하여 시뮬레이션 할 수 있는 방법을 개발하였다. 이를 활용한다면, 다양한 도파로 타입의 Ge 광 검출기의 빛 흡수 영역에서의 광 생성 캐리어들의 움직임에 대한 특성 연구를 할 수 있다. 그리고 본 논문에서는 1.5-μm 대역에서 동작 가능한 Ge 광 검출기의 정확도가 높은 등가회로 모델 또한 연구가 되었다. 이 모델은 p-i-n 접합 부분과 기생 성분들을 표현하기 위한 RC 수동 회로 소자, 확산 및 표동에 의해 움직이는 광 생성 캐리어를 표현하기 위해 2개의 전류원, 잡음을 표현하기 위해 1개의 전류원으로 구성되어 있다. 각각의 모델 파라미터들은 전기적인 S-파라미터 측정, 특별히 개발된 TCAD를 활용한 광 검출 주파수 특성 시뮬레이션 그리고 잡음 측정을 통해 추출되었다. 추출된 파라미터 기반으로 성립된 등가회로 모델은 다양한 바이어스 전압 조건에 대해 광 검출 주파수 응답 특성을 제공하며 이는 다양한 타입의 검출기들에 대해 적용할 수 있음을 확인하였다. 이러한 연구 결과는 PD 성능을 분석하는데 큰 유용성을 가지며, 고 성능 광 수신기 회로 설계에도 큰 도움이 될 것으로 기대된다.

핵심 단어: 통합-시뮬레이션, 등가회로 모델, Ge 광 검출기, 광 연결, 검출기 잡음, 광 검출 주파수 응답, Si 포토닉스, TCAD

List of Publications

International Journal Papers

[1] Jeong-Min Lee, Seong-Ho Cho, and Woo-Young Choi, "An Equivalent Circuit Model for a Ge Waveguide Photodetector on Si," IEEE Photonics Technology Letters, Vol. 28, No. 21, pp.2435-2438, Nov. 2016.

[2] Hyun-Yong Jung, Jeong-Min Lee, and Woo-Young Choi, "A High-Speed CMOS Integrated Optical Receiver with an Under-Damped TIA," IEEE Photonics Technology Letters, Vol. 27, No. 13, pp.1367-1370, July 2015.

[3] Jinsoo Rhim, Yoojin Ban, Byung-Min Yu, Jeong-Min Lee, and Woo-Young Choi, "Verilog-A behavioral model for resonance-modulated silicon micro-ring modulator," Optics Express, Vol. 23, No. 7, pp. 8762-8772, Apr. 2015

[4] Myung-Jae Lee, Jeong-Min Lee, Holger Rücker, and Woo-Young Choi, "Bandwidth Improvement of CMOS-APD With Carrier-Acceleration Technique," IEEE Photonics Technology Letters, Vol. 27, No. 13, pp.1387-1390, July 2015.

[5] Jinsoo Rhim, Jeong-Min Lee, Byung-Min Yu, Yoojin Ban, Seong-Ho Cho, and Woo-Young Choi, "25-Gb/s Optical Transmitter with Si Ring Modulator and CMOS Driver," Journal of the Optical Society of Korea, Vol. 18, No. 5, pp. 564-568, Oct. 2014.

International Conference Presentations

[1] Jeong-Min Lee, Minkyu Kim, S. Lischke, L. Zimmerman, Seong-Ho Cho, and Woo-Young Choi, "Photodetection Frequency Response Characterization for High-Speed Ge-PD on Si With an Equivalent Circuit," *in proceedings of Optoelectronics and Communications Conference/International Conference of Photonics in Switching (OECC/PS)* (2016).

[2] S. Lischke, D. Knoll, C. Mai, M. Kroh, D. Schmidt, A. Peczek, J. Kreißl, Jeong-Min Lee, Minkyu Kim, Woo-Young Choi and L. Zimmermann, "Design Effects on the Performance of High-Speed Ge Photo Detectors," *in proceedings of IEEE International Conference on Group IV Photonics (GFP)* (2016).

[3] Jinsoo Rhim, Byung-Min Yu, Jeong-Min Lee, Seong-Ho Cho, and Woo-Young Choi, "Modulation Performance Optimization for Depletion-Type Silicon Micro-Ring Modulators," *in proceedings of IEEE Optical Interconnects Conference (OIC)* (2016).

[4] Hyun-Yong Jung, Jeong-Min Lee, and Woo-Young Choi, "A High-Speed CMOS Integrated Optical Receiver with an Under-Damped TIA," *in proceedings of IEEE Photonics Conference (IPC)* (2015).

[5] Yoojin Ban, Byung-Min Yu, Jinsoo Rhim, Jeong-Min Lee, and Woo-Young Choi, "Modeling of self-heating effect for depletion-type Si micro-ring modulator," *in proceedings of Optical Interconnects Conference (OIC)* (2015).

[6] Jeong-Min Lee and Woo-Young Choi, "An Equivalent Circuit Model for Germanium Waveguide Vertical Photodetectors on Si," *in proceedings of International Topical Meeting on Microwave*

Photonics/Asia-Pacific Microwave Photonics Conference (MWP/APMP), pp.139-141 (2014).

[7] Jinsoo Rhim, Yoojin Ban, Jeong-Min Lee, Seong-Ho Cho, and Woo-Young Choi, "A Behavior Model for Silicon Micro-Ring Modulators and Transmitter Circuit-Level Simulation Using It," *in proceedings of IEEE International Conference on Group IV Photonics (GFP)* (2014).

[8] Byung-Min Yu, Jeong-Min Lee, Yoojin Ban, Seong-Ho Cho, Woo-Young Choi, "Model Parameter Extraction for Si Micro-Ring Modulators," *in proceedings of Optoelectronics and Communications Conference (OECC)* (2014).

[9] Yoojin Ban, Jeong-Min Lee, Byung-Min Yu, Seong-Ho Cho, and Woo-Young Choi, "Small-Signal Frequency Responses for Si Micro-Ring Modulators," *in proceedings of IEEE Optical Interconnects Conference (OIC)* (2014).

[10] Yoojin Ban, Jeong-Min Lee, and Woo-Young Choi, "A Small-Signal Model for Modulation Response of a Silicon Ring Modulator," *in proceedings of International Conference on Group IV Photonics (GFP)* (2013).

[11] Minsu Ko, Jeong-Min Lee, Myung-Jae Lee, and Woo-Young Choi, "A 5-GHz CMOS Integrated Radio-Over-Fiber Receiver," *in proceedings of Asia-Pacific Microwave Photonics Conference (APMP)* (2013).

[12] Jeong-Min Lee, Holger Rücker, and Woo-Young Choi "60-GHz Voltage-Controlled Oscillator and Frequency Divider in 0.25-μm SiGe BiCMOS Technology," *in proceedings of IEEE International SoC Design Conference (ISOCC)*, pp. 65-67 (2012).

Domestic Conference Presentations

[1] 이정민, 김민규, 최우영, “40-GHz Ge-on-Si Photodetector,” *광전자 및 광통신 학술회의*, June 2016, 부산.

[2] 이정민, 조성호, 최우영, “Waveguide-Type Vertical Ge-on-Si 광 검출기의 등가회로 모델,” *2015 Photonics Conference*, Dec. 2015, 평창.

[3] 반유진, 임진수, 유병민, 성연수, 이정민, 최우영, “Modeling of Si Micro-Ring Modulator Self-Heating,” *2014 하계 학술 발표회*, Aug. 2014, 제주.

[4] 정현용, 이정민, 윤진성, 최우영, “Ge 광 검출기를 사용한 25 Gb/s CMOS 혼성 집적 광 수신기,” *2014 SoC 춘계학술대회*, May 2014, 서울.

[5] 반유진, 이정민, 유병민, 최우영, “Design and Measurement of Directional Couplers to be used in Silicon Micro-Ring Modulators,” *2013 Photonics Conference*, Nov. 2013, 제주.

[6] 이정민, 유병민, 반유진, 최우영, “DC Characteristics of a Silicon Micro-Ring Modulator,” *2013 Photonics Conference*, Nov. 2013, 제주.

[7] 이정민, 이명재, Holger Rücker, 최우영, “Performance Comparison of 850-nm CMOS Avalanche Photodetectors Based on Single or Double Junctions,” *The 20th Conference Optoelectronics and Optical Communications (COOC)*, May 2013, 경주.

[8] 유병민, 반유진, 이정민, 최우영, “Optimization of 20-GHz Silicon Ring Modulator Design,” *The 20th Conference Optoelectronics and Optical Communications (COOC)*, May 2013, 경주.

[9] 반유진, 이정민, 유병민, 최우영, “실리콘 링 공진기의 Critical Coupling에 직선 도파관의 너비와 Gap 거리가 미치는 영향 분석,” *2013 Photonics Conference*, Nov. 2012, 평창.

[10] 고민수, 이정민, 윤진성, 이명재, 최우영, “60GHz 광섬유-무선 다운링크를 위한 SiGe BiCMOS 집적화된 광-밀리미터파 변환기,” *제19회 한국 반도체 학술대회*, Feb. 2012, 서울.

[11] 이정민, 최우영, “Ku-Band LNB 수신단을 위한 위성통신용 LNA 설계,” *춘계 마이크로파 및 전파전파 학술대회*, May 2011, 일산.

Awards

[1] **ISOCC 2014 Best Poster Award:** "12.5-Gb/s Monolithically Integrated Optical Receiver with CMOS Avalanche Photodetector," *International SoC Design Conference*, Chip Design Contest Session (2014).

[2] **우수논문상:** "실리콘 링 모듈레이터의 Self-Heating 모델링," *한국광학회 2014년도 하계학술발표회* (2014).

[3] **APMP 2013 Best Student Poster Award:** "A 5-GHz CMOS Integrated Radio-Over-Fiber Receiver," *Asia-Pacific Microwave Photonics Conference* (2013).

[4] **우수논문상:** "Performance Comparison of 850-nm CMOS Avalanche Photodetectors Based on Single or Double Junctions," *The 20th Conference on Optoelectronics and Optical Communications* (2013).